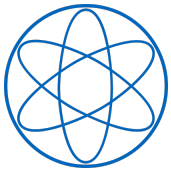

TECHNISCHE UNIVERSITÄT MÜNCHEN
Fakultät für Physik
Lehrstuhl für Oberflächen- und Grenzflächenphysik

Transition Metal Centers Embedded in Surface-Confined Coordination Environments: Tunable Interfaces and N-Heterocyclic Carbene Nanoarchitectures

Peter Knecht

TECHNISCHE UNIVERSITÄT MÜNCHEN
Fakultät für Physik
Lehrstuhl für Oberflächen- und Grenzflächenphysik

Transition Metal Centers Embedded in Surface-Confined Coordination Environments: Tunable Interfaces and N-Heterocyclic Carbene Nanoarchitectures

Peter Knecht

Vollständiger Abdruck der von der Fakultät für Physik der Technischen Universität München zur Erlangung des akademischen Grades eines Doktors der Naturwissenschaften (Dr. rer. nat.) genehmigten Dissertation.

Vorsitzender: Prof. Dr. David Egger

Prüfende der Dissertation:
1. Prof. Dr. Johannes V. Barth
2. Prof. Dr. Mathias Senge

Die Dissertation wurde am 28.04.2021 bei der Technischen Universität München eingereicht und durch die Fakultät für Physik am 11.05.2021 angenommen.

Abstract

The molecular functionalization of surfaces offers an inexpensive and elegant method to impart and tailor a material's physicochemical properties. Molecules can be designed specifically to alter a particular property in the desired way. By using principles of the bottom-up approach the surface layer can be fabricated with atomic precision. In this thesis, the self-assembly and characteristics of different model systems comprising metal-organic complexes and nanostructures are explored on an atomically flat silver surface under ultra-high vacuum conditions. In this aspect, we apply a comprehensive set of experimental techniques consisting of advanced microscopy (scanning tunneling microscopy and manipulation), electron and mass spectroscopy (UV/X-ray photoelectron spectroscopy, temperature programmed desorption) and diffraction (low-energy electron diffraction, normal incidence X-ray standing waves).

Specifically, we employ a linear linker molecule consisting of a benzene functionalized with two tetrazole moieties at *para* positions and investigate its self-assembly and coordination with the native Ag adatoms and codeposited Fe adatoms on Ag(111). We identify a rich spectrum of room-temperature stable Ag and Fe^{2+} coordination nodes depending on the formation temperature. Thus, we unravel the atomic structure of Ag surfaces functionalized with tetrazole corrosion inhibitors and show the formation of novel organometallic Fe structures with potential magnetic properties.

In a second part we carry out a detailed study of the geometric and electronic structure, self-assembly and thermal transformation of Ru tetraphenyl porphyrin (Ru-TPP) on Ag(111). For the pristine Ru-TPP, two different phases form depending on the surface molecular coverage. By thermal annealing these porphyrin layers undergo intramolecular cyclodehydrogenation reactions. Depending on the arrangement of the phenylene substituents, the Ru atoms have distinct electronic structures and the porphyrin macrocycles adapt differently to the surface, i.e. saddle shape (pristine Ru-TPP) or bowl shape (planarized Ru-TPP derivatives). In all cases, the Ru atom resides close to the surface ($2.59/2.45$ Å), preferably located at the fcc(111) hollow sites and in between the plane of the porphyrin macrocycle and the Ag surface.

The tetrapyrrole flexibility of the surface-confined Ru porphyrin proves crucial for CO ligation. The pristine Ru-TPP on Ag(111) is found to exhibit different modes of CO ligation (both μ and axial), but strikingly no CO ligation is observed for the planarized derivatives. The most stable type is determined to be the axial mode (with E_{Bind} ~ 0.8 eV). We therefore unambiguously demonstrate that the substituents regulate the interfacial conformational adaptability, either promoting or obstructing the uptake of axial CO adducts.

Finally we use Ru porphyrins to control both the orientation and lateral arrangement of N-heterocyclic carbenes (NHCs) on solid surfaces, a current challenge of surface functionalization. The coupling of the NHC to the Ru porphyrin is a facile process which takes place

on the interface: we apply NHCs as functional, robust pillars on well-defined, pre-assembled Ru-TPP monolayers on silver and characterize these interfaces with atomic precision. The NHCs assemble at room temperature modularly and reversibly on the Ru porphyrin arrays. We demonstrate a selective positioning and axial ligation at the Ru centers. With its binding, the NHC modifies the interaction of the Ru porphyrin with the Ag surface, displacing the Ru atom by 1 Å away from the surface. This arrangement of NHCs allows us to address individual ligands by controlled manipulation with the tip of a scanning tunneling microscope, creating patterned structures on the nanometer scale.

Upon application of the same NHC ligand on the denser packed Ru-TPP monolayer, we discovered an extraordinary phenomenon: a fraction of the Ru porphyrin molecules is portered from the Ag surface and engages in the formation of a second molecular layer. We reveal a reversible structural rearrangement of the molecular layer which is induced by the NHC binding and is reversed by annealing-induced desorption of the NHC ligand.

Zusammenfassung

Die molekulare Funktionalisierung von Oberflächen ist eine günstige und elegante Methode, um die physikalisch-chemischen Eigenschaften von Materialien beeinzuflussen und zu formen. Moleküle können spezifisch hergestellt werden, um eine bestimmte Eigenschaft gezielt zu steuern. Mithilfe des sogenannten "Bottom-up" Verfahrens kann eine molekulare Schicht mit atomarer Präzision auf eine Oberfläche angebracht werden. In dieser Arbeit werden die Selbstorganisation und die Eigenschaften von verschiedenen Metall-organischen Modellsystemen auf einer atomar flachen Ag(111) Oberfläche im Ultrahochvakuum untersucht. Hierzu werden verschiedene experimentelle Methoden eingesetzt, darunter Rastertunnelmikroskopie und -manipulation, Röntgen- und Ultraviolettphotoelektronenspektroskopie sowie thermische Desorptionsspektroskopie, Spektrokopie mithilfe von stehenden Röntgenwellenfeldern und Elektronenbeugung.

Zunächst wird die Selbstorganisation von linearen molekularen Verbindungselementen, bestehend aus einem Benzen Ring, der mit zwei Tetrazol-Seitenketten in *para*-Stellung funktionalisiert wurde, und deren Koordinierung mit Ag und Fe Adatomen auf einer Ag(111) Oberfläche untersucht. Wir entdecken ein Spektrum an Ag und Fe^{2+} koordinierten Knoten, die sich bei jeweils unterschiedlichen Temperaturen bilden, jedoch alle Raumtemperaturstabilität aufweisen. Somit decken wir die atomare Struktur von einer Ag Oberfläche, die mit einem vor Korrosion schützenden Molekül funktionalisiert wurde, auf und zeigen zudem die Bildung von neuartigen organometallischen Fe Konstruktionen mit potentiell magnetischen Eigenschaften.

Außerdem wird eine detaillierte Studie über die geometrischen und elektronischen Eigenschaften, die Struktur und thermische Transformation von Ru Tetraphenylporpyrin (Ru-TPP) auf einer Ag(111) Oberfläche durchgeführt. Abhängig von der molekularen Bedeckung der Oberfläche können zwei unterschiedliche Phasen der Selbstorganisation ausgemacht werden. Durch eine thermische Behandlung dieser Schicht werden Cyclodehydrierungsprozesse zwischen Phenylsubstituenten und Makrozyklus ausgelöst, was signifikante Veränderungen zur Folge hat. Abhängig von der Anordnung der Phenylringe ändert sich sowohl die elektronische, als auch die geometrische Struktur, wodurch der Makrozyklus der Moleküle die Form eines Sattels (vor thermischer Behandlung) oder einer Schale (nach thermischer Behandlung) annimmt. In beiden Fällen konnten wir für das Ru Atom die Adsorptionshöhe bestimmen ($2.59/2.45$ Å vor/nach thermischer Behandlung), das so zwischen der Ag Oberfläche und dem Porphyrin Makrozyklus liegt, und haben außerdem eine Präferenz der Adsorptionsposition auf Muldenplätzen der Ag(111) Oberfläche ermittelt.

Die unterschiedlichen Formen, die der Makrozyklus des Ru-TPP annehmen kann, haben sich als bedeutend für die Bindung von CO an das Metallzentrum herausgestellt. Für Ru-TPP auf der Ag(111) Oberfläche können verschiedene Bindungsvarianten aufgezeigt werden,

wohingegen nach thermischer Behandlung keine CO Bindung festgestellt werden kann. Als stabilste Bindungsvariante stellt sich die axiale Bindung an Ru-TPP heraus (Bindungsenergie $\sim$0.8 eV). Wir zeigen hier eindeutig, dass die Substituenten am Makrozyklus des Porphyrins dessen Anpassungsfähigkeit beeinflussen, was eine Bindung von CO sowohl ermöglichen als auch unterbinden kann.

Zuletzt werden die Ru Porphyrine verwendet, um die Anordnung und Ausrichtung von N-heterocyclischen Carbenen (NHCs) relativ zu einer Oberfläche zu kontrollieren. Das Anbringen von NHCs am Ru Porphyrin wird direkt auf der Oberfläche durchgeführt: NHCs erweisen sich als robuste, funktionale Pfeiler auf wohldefinierten, vorkonfektionierten Ru-TPP Monolagen auf Silber und werden anschließend mit atomarer Präzision charakterisiert. Die NHCs verteilen sich modular und reversibel auf der Anordnung von Ru-TPP. Es wird gezeigt, dass die Bindung selektiv an den Ru Atomen stattfindet und eine vollständige Funktionalisierung erreicht werden kann. Dadurch wird die Interaktion zwischen Ru Atom und der Silber Oberfläche beeinflusst, was dazu führt, dass sich das Ru Atom etwa 1 Å von der Oberfläche entfernt. Es ist außerdem möglich, einzelne NHC Moleküle durch kontrollierte Manipulation mit der Spitze des Rastertunnelmikroskops zu entfernen, wodurch beliebige Muster in Nanometergröße erstellt werden können.

Wird das NHC auf eine dichter gepackte Monolage von Ru-TPP angebracht, kann ein anderes Phänomen beobachtet werden: Ein Teil der Ru-TPP Moleküle wird von der Silber Oberfläche in eine höhere Lage transportiert. Es wurde eine Rekonstruktion der molekularen Monolage beobachtet, induziert durch die Bindung des NHCs. Dieser Effekt kann durch thermisch induzierte Desorption des Liganden umgekehrt werden.

Contents

Acronyms

2D	two dimensional
2H-TPP	tetraphenyl porphyrin
3D	three dimensional
AFM	atomic force microscopy
BTB	1,4-di(1*H*-tetrazole-5-yl)benzene
CoPc	Co phthalocyanine
Co-TPP	Co tetraphenyl porphyrin
CuPc	Cu phthalocyanine
DFT	density functional theory
DLS	Diamond Light Source
FePc	Fe phthalocyanine
Fe-TPP	Fe tetraphenyl porphyrin
FFT	fast Fourier transform
HOPG	highly oriented pyrolytic graphite
IMe	1,3-dimethyl-2*H*-imidazol-1-ium-2-ide
IMe-CO_2	1,3-dimethyl-1*H*-imidazol-3-ium-2-carboxylate
LDOS	local density of states
LEED	low-energy electron diffration
LHe	liquid helium
LN_2	liquid nitrogen
LT-STM	low-temperature STM
MOF	metal-organic framework
nc-AFM	non-contact AFM
NHC	N-heterocyclic carbene
NIXSW	normal incidence X-ray standing wave
OMBE	organic molecular beam epitaxy
RT	room temperature
Ru-TPP	Ru tetraphenyl porphyrin
Ru-TPP_{pl}	planarized Ru tetraphenyl porphyrin derivatives
SAM	self-assembled monolayer
SCO	spin crossover
STM	scanning tunneling microscopy
Ti-TPP	Ti tetraphenyl porphyrin
TPD	temperature programmed desorption
UHV	ultra-high vacuum

UPS	ultraviolet photoelectron spectroscopy
VT-STM	variable-temperature STM
XPS	X-ray photoelectron spectroscopy
XSW	X-ray standing wave
Zn-TPP	Zn tetraphenyl porphyrin

1 Introduction

Technological advances of the last decades have lead to a level of miniaturization, where the manufacturing dimensions for certain key technologies have come down to a few nanometers. [1, 2] Further downsizing is not only challenging in the fabrication process, but also requires to take quantum phenomena into account, which will play an important role in making such small devices. A different approach to realize devices in the nanometer regime features the application of molecules on well-defined surfaces, which offer a plethora of functionalities by the possibility of tailoring molecules for each specific task. There are examples of functional devices on a single-molecule level, including transistors, [3] switches, [4, 5] nanoscale "race cars", [6] amplifiers, [7] logic gates, [8] or storage devices. [9]

However, the development of functional molecular nanosystems is not limited to isolated molecules. Nanostructured materials based on the molecular self-assembly on a surface are also a current topic of interest. While the self-assembly process enables the large-scale fabrication of such materials, their properties are not only determined by the molecular building blocks. The formed lattice structures [10, 11] and the underlying substrate [12–14] also play an important role. The understanding of the interplay of these contributions is essential for engineering such systems with specific functionalities, which can include adressing spins of single-molecule magnets [15, 16] and catalysis. [17, 18] In this thesis, we aim for a better understanding of such nanostructures by studying different model systems, which are outlined below. A more detailed motivation for each system will be given in the respective dedicated Chapter.

Inspired by coordination polymers and networks of tetrazoles and transition metals in solution based chemistry, which exhibit fluorescence, [19] second harmonic generation [19] or spin crossover phenomena, [20] the first project (presented in Chapter 4) describes the effect of iron coordination to a molecule, consisting of a phenylene with two tetrazole moieties at *para* positions. Here, the focus lies on the formation of coordination motifs and observation of potential magnetic properties of the iron nodes. In contrast to solution based chemistry, the material synthesis procedures were conducted under ultra-high vacuum (UHV) conditions on an atomically flat Ag(111) surface, ensuring a clean and highly controlled environment for the characterized sample.

The second project (presented in Chapter 5) is a profound analysis of the properties of Ru tetraphenyl porphyrin (Ru-TPP) on a Ag(111) surface. Ruthenium is known for its catalytic [21, 22] and magnetic [23, 24] properties, while the tetraphenyl porphyrin offers an already well-known platform for the integration of metal atoms, self-assembling in well-defined structures on coinage metal surfaces. [25–27]

Firstly, it is shown that, in contrast to other tetraphenyl porphyrins on Ag(111), Ru-TPP can self-assemble in two different ways: For submonolayer coverages the pattern resembles the

self-assembly of other tetraphenyl porphyrins on the same surface. Approaching a saturated monolayer, a transition into a higher density compressed phase is observed. Furthermore, a detailed study of the conformation of the Ru-TPP is conducted, analyzing the macrocycle conformation and the adsorption height of the Ru center and comparing it to planarized Ru porphyrin derivatives.

In the following Chapters such layers of Ru-TPP are used as organised pedestals for the ligation of organic and inorganic molecules, binding to the ruthenium center of the porphyrin. The understanding of the ligation behaviour is crucial for technical applications e.g. in catalysis [28, 29] or for gas sensors. [30, 31]

In Chapter 6, a model system is investigated with the ligation of CO on a Ru-TPP layer on Ag(111). It was shown that this ligand forms a strong bond with the metal center in free Ru porphyrins, [32] which makes CO a promising choice as a small inorganic ligand. We show that there are different bonding modes for CO on Ru-TPP, one of them being stable at temperatures up to $\sim$250 K. Additionally, we find a different ligation behavior depending on the macrocycle conformation of the Ru-TPP: While the pristine Ru-TPP allows the CO ligation, this is not observed for its planarized derivatives.

In Chapter 7, the binding of a prototypical N-heterocyclic carbene (NHC), 1,3-dimethyl-2*H*-imidazol-1-ium-2-ide (IMe), on a submonolayer of Ru-TPP is visited. NHCs are stable carbenes, which have been eagerly explored in novel organometallic materials, metallopharmaceuticals, catalysts and surface functionalisation. [33] We analyze the electronic and conformational changes of the Ru-TPP upon ligation, characterizing the desorption characteristics of IMe and present nanofabrication opportunities by the controlled removal of single ligands via the tip of a scanning tunneling microscope (STM).

Chapter 8 highlights an intriguing reconstruction, which is triggered by the ligation of IMe on Ru-TPP in the more densely packed compressed phase. We show that upon ligation, which induces a decoupling of the Ru-TPP from the Ag(111) surface, $\sim$20 % of the Ru(IMe)-TPP complexes are portered from the contact layer into a second layer, creating enough room in the contact layer to allow the remaining molecules to self-assemble into the less densely packed square phase. Both effects are reversible by thermal annealing.

Multiple techniques have been used for the acquisition of the data, which was necessary to gain insights into different properties of the studied systems. All experiments were conducted under UHV conditions, which is required for most of the employed analysis techniques and guarantees well-defined systems free of impurities. Imaging of the assemblies with submolecular resolution and the patterning of molecular structures were performed by STM. The periodic structure of the molecular assembly was determined in conjunction with low-energy electron diffration (LEED). Electronic properties could be accessed via X-ray photoelectron spectroscopy (XPS) and ultraviolet photoelectron spectroscopy (UPS), while information about the adsorption geometry could be inferred by normal incidence X-ray standing waves (NIXSW). Temperature programmed desorption (TPD) measurements allowed to determine desorption energies and kinetics. Complementary density functional theory (DFT) calculations and atomic force microscopy (AFM) imaging, contributed by collaboration partners, were employed to refine the experimental findings and guide the data interpretation.

2 Theoretical principles of experimental methods

Scanning tunneling microscopy

Scanning tunneling microscopy (STM) is a technique allowing real space imaging with atomic resolution. It was developed in 1981 at the IBM Research Laboratory in Zurich by Gerd Binnig and Heinrich Rohrer [34] who were awarded half a Nobel Prize in Physics in 1986 for this invention. Images are acquired by an atomically sharp, metallic tip scanning the surface at a very small distance with a bias voltage applied (Figure 2.1). Due to the effect of quantum tunneling, a current flows between tip and sample, allowing to obtain information about the topography and electronic structure of the surface. The precise movement of the tip in the sub-nanometer regime is realized via the attached piezoelectric tube (Figure 2.1).

Electron tunneling

In classical physics, particles cannot propagate through a potential barrier V, if their energy E is smaller than V. However, as described first in 1927 by Friedrich Hund, [35] quantum mechanics allows particles to propagate through barriers of finite height with a certain probability. Particles such as electrons can behave as waves with a wave function Ψ, which can be described by the Schrödinger equation:

$$-\frac{\hbar}{2m}\frac{d^2\Psi}{dz^2} + V(z)\Psi = E\Psi \tag{2.1}$$

Here we employ a one-dimensional, time-independent Schrödinger equation, with the reduced Planck constant $\hbar$ and the electron mass m. With a rectangular potential barrier of height V_0 (Figure 2.2A, region 2) and an incoming wave propagating in positive z direction (Figure 2.2A, region 1), we obtain as solution for the different regions:

$$\Psi_{1,3}(z) = \Psi^0_{1,3}\exp\left(\pm i\frac{\sqrt{2mE}}{\hbar}z\right) \tag{2.2}$$

$$\Psi_2(z) = \Psi^0_2\exp\left(-\frac{\sqrt{2m\left(V_0 - E\right)}}{\hbar}z\right) \tag{2.3}$$

While the solution for region 3 allows the propagation behind the potential barrier, the probability of tunneling can be determined by the solution for region 2: For a potential of width d

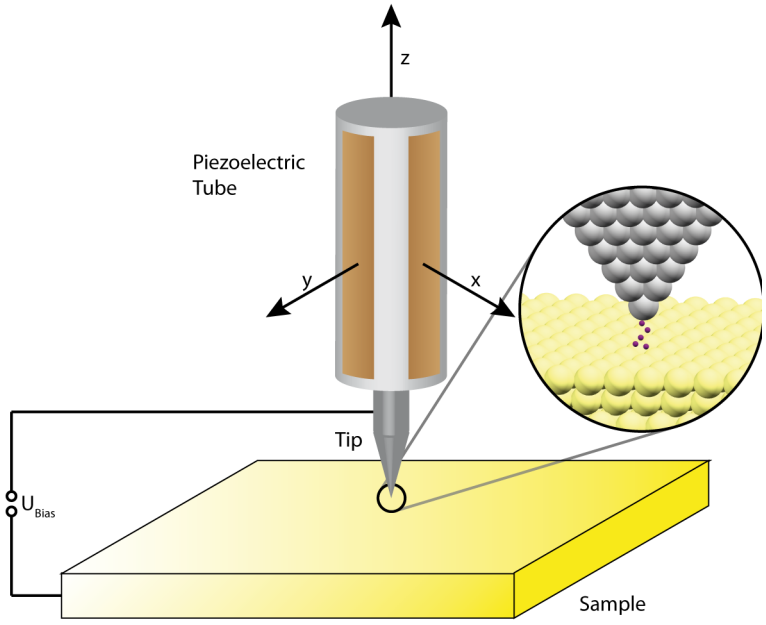

Figure 2.1 Setup used for scanning tunneling microscopy. The tip can be moved by the piezoelectric tube, allowing three-dimensional positioning. If the tip is close to the sample and a bias voltage is applied, electrons can tunnel, creating a tunneling current (see inset).

we obtain as a transmission probability T:

$$T = |\Psi_2^0|^2 \exp\left(-2\frac{\sqrt{2m\,(V_0 - E)}}{\hbar}d\right) \tag{2.4}$$

It can be seen that the probability for the electron to propagate through the barrier is decreasing exponentially with the width of the potential and the energy difference between the potential and the electron. In case of a tunneling microscope, the potential barrier translates to the vacuum space between the tip and the sample (Figure 2.2B). The distance between those two determines the width of the potential barrier. In tunneling contact the Fermi level of tip and sample align, so that electrons tunnel in both directions equally, giving a net current of zero. However, if a voltage U_{Bias} is applied (Figures 2.1 and 2.2), the Fermi level will be offset and therefore a tunneling current can flow. A more elaborated model of the tunneling current I_t was presented by by Hamann and Tersoff in 1985, [36] based on a description from a many-particle perspective from Bardeen. [37] In this approach the tunneling current I can be expressed as

$$I = \frac{2\pi e}{\hbar}\sum_{\mu,\nu} f(E_\mu)\left[1 - f(E_\nu + eV)\right]|M_{\mu\nu}|^2\delta(E_\mu - E_\nu) \tag{2.5}$$

with the Fermi function $f(E)$, the applied bias voltage V, the tunneling matrix element $M_{\mu\nu}$ between state Ψ_μ of the tip and Ψ_ν of the sample, and the energy E_μ of state Ψ_μ in the absence of tunneling. This expression can be further simplified under the assumption of

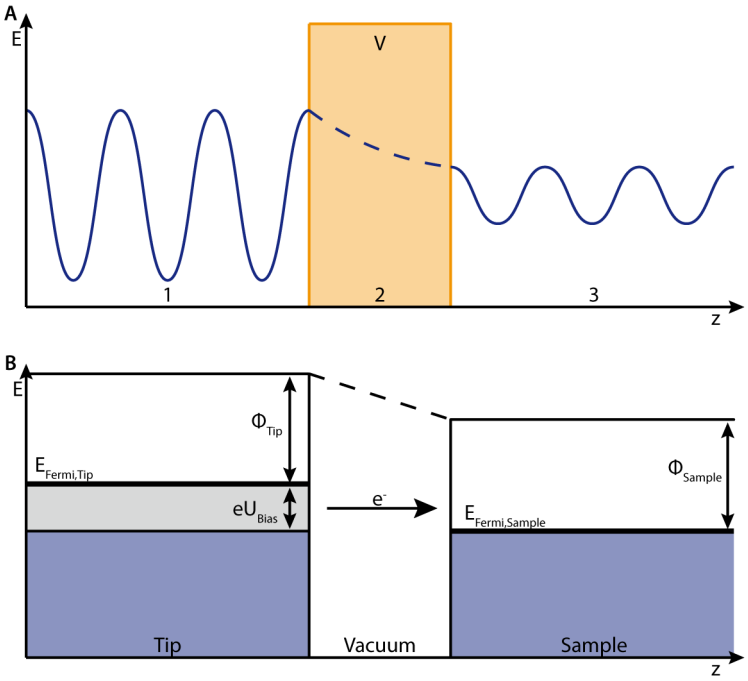

Figure 2.2 (A) Schematic illustration for electron tunneling through a potential barrier V. The incoming electron wave function in region 1 hits the potential barrier in region 2. The exponential decay of the wave function along the potential barrier leads to a reduced amplitude of the electron wave function in region 3, which is related to the tunneling probability. (B) Schematic illustration of the tip-sample junction of an STM. The applied bias between tip and sample alters the position of the Fermi-level, allowing electron tunneling through the vacuum barrier. Without an applied bias, the tunneling probability is equally high in both directions, resulting in no net current.

temperatures not significantly higher than room temperature and small bias voltages to

$$I = \frac{2\pi}{\hbar} e^2 V \sum_{\mu,\nu} |M_{\mu\nu}|^2 \delta(E_\mu - E_F)\delta(E_\nu - E_F) \tag{2.6}$$

The matrix element can be expressed by an integral over a surface, which is located entirely within the vacuum region between tip and sample:

$$M_{\mu\nu} = \frac{\hbar^2}{2m} \int dS \left(\Psi_\mu^* \overrightarrow{\nabla} \Psi_\nu - \Psi_\nu \overrightarrow{\nabla} \Psi_\mu^* \right) \tag{2.7}$$

As the exact shape of the tip is difficult to determine and can be manipulated only to a certain extent in experiments, a spherical shape of the apex with radius R and center at $\overrightarrow{r_0}$ is assumed. By this the expression for the tunneling current resolves to

$$I = 8\sqrt{2}\pi^3 \hbar^3 e^2 V \sqrt{\frac{\phi}{m^3}} D_t(E_F) R^2 \exp(2\hbar^{-1} R\sqrt{2m\phi}) \sum_\nu |\Psi_\nu(\overrightarrow{r_0})|^2 \delta(E_\nu - E_F) \tag{2.8}$$

with the work function ϕ assumed to be the same for tip and sample and the density of states per unit volume of the tip D_t. From this equation the expected exponential behavior of the tunneling current with the barrier width d can be observed as

$$|\Psi_\nu(\overrightarrow{r_0})|^2 \propto \exp(-2\frac{\sqrt{2m\phi}}{\hbar} d) \tag{2.9}$$

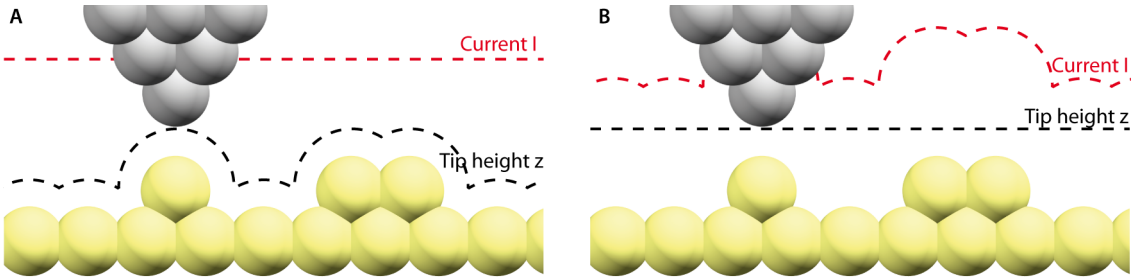

Figure 2.3 Schematic illustration of the operational modes of an STM. (A) constant current mode: The tip height is adjusted via a feedback-loop such that the tunneling current between tip and sample is constant. (B) constant height mode: The tip height is fixed, so that no feedback-loop is required.

Additionally, the tunneling current is proportional to the local density of states (LDOS) of the sample, represented by the sum in Eq. 2.8. Therefore, an image recorded by an STM can be understood as the convolution of the topography and the LDOS.

Operational modes of an STM

There are two different modes to scan the surface: Constant current mode and constant height mode (Figure 2.3). In the constant height mode, the tip does not change its z-position and the current, which is fluctuating with changes of tip-sample separation and accessible electronic states, is recorded. A flat surface as well as a very stable setup are required for this operation mode, as the exponential decay of the tunneling current with increasing tip-sample separation leaves only a narrow region where currents are measurable. The more frequently used mode is the constant current mode, where the z-position of the tip is adjusted by a feedback loop in such a way that the tunneling current remains constant. Thus, the information enclosed in the z-position of the tip can be related to topography and LDOS of the investigated sample.

X-ray photoelectron spectroscopy & ultraviolet photoelectron spectroscopy

X-ray photoelectron spectroscopy (XPS) is a method to quantify the elemental and chemical composition of a sample. It relies on the photoelectric effect, which was first observed in 1887 by Heinrich Hertz [38] and theoretically explained in 1905 by Albert Einstein [39], being awarded with the Nobel Price in Physics in 1921 for this work. The sample is exposed to an X-ray beam of a well-defined energy, leading to the absorption of single photons exciting core level electrons of the atoms of the sample (Figure 2.4). These electrons can be ejected and have a well-defined kinetic energy, which depends on the energy of the incoming photons $h\nu$, the binding energy of the corresponding core level with respect to the Fermi level E_b and the work function Φ:

$$E_{kin} = h\nu - E_b - \Phi \tag{2.10}$$

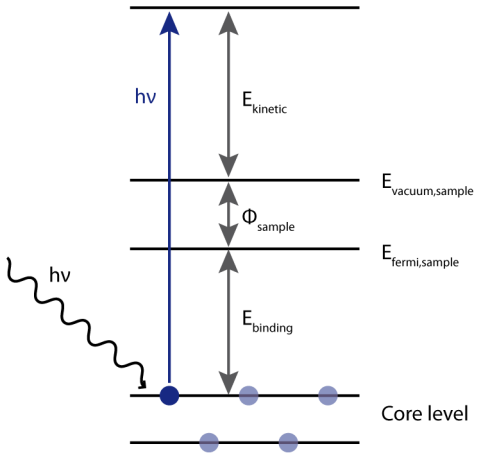

Figure 2.4 Schematic of the working principle for XPS. Incoming photons of energy $h\nu$ remove core level electrons from the sample, which have a characteristic kinetic energy, from which the binding energy of the corresponding core level can be obtained. The binding energies allow to analyze the elemental composition of the sample and the chemical environment of the investigated elements.

With a hemispherical electron energy analyzer, E_{kin} can be measured, which allows to determine the binding energy of the core level, from which the electron was ejected. The energy range of the X-rays used for this technique to access the core level electrons lies usually between $100\,\mathrm{eV}$ and $2000\,\mathrm{eV}$. In this energy range, the inelastic mean free path for electrons in solids is approximately 0.5–$3\,\mathrm{nm}$ [40], so that only electrons from the top layers contribute to the detected photoemission, making X-ray photoelectron spectroscopy (XPS) a surface-sensitive technique. Core level binding energies are specific for each element and sensitive to the chemical environment: Chemical bonds which include the sharing of valence electrons can change the screening of the positive nuclear charge and therefore change the binding energy of the core levels. From the peak intensities, the relative abundance of each contribution can be extracted, [41] allowing to determine quantitatively the chemical composition on the sample. A requirement for this technique is a (semi)conductive sample, which allows to replace the removed electrons. For non-conductive samples, an electron flood gun has to be added to the setup to avoid a charging of the sample surface, which would lead to a shifting of the measured core level energies.

Ultraviolet photoelectron spectroscopy (UPS) uses the same principle, but is operated with ultraviolet photons. These photons cause photoemission from valence electrons of the sample, which can be used to gain information about the work function, band structure and molecular states of the investigated system.

X-ray standing waves

X-ray standing wave (XSW) is a technique to determine the adsorption height and registry of adsorbates on single crystal surfaces. Its working principle is based on the creation of a standing wave field on the surface of the crystal, which influences the photoemission characteristics of the adsorbates to allow an element-specific determination of adsorption sites for the adsorbates. Due to the necessity of a tunable hard X-ray beam (X-ray energies $>2\,\mathrm{keV}$),

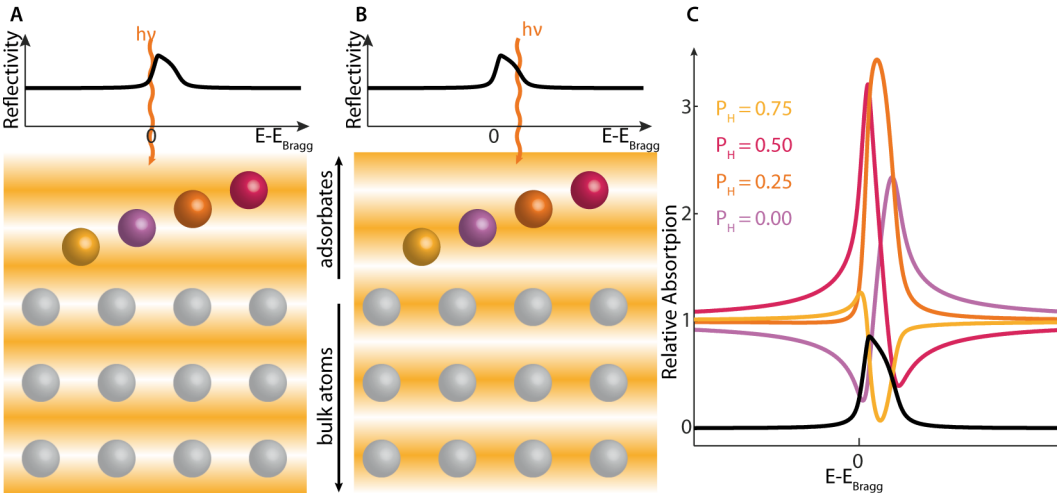

Figure 2.5 Scheme of the working principle of NIXSW measurements. (A,B) Illustration of the standing wave field with a phase shift of 0 (A) and π (B). The top graphs show the reflectivity of the substrate, the wavy orange line indicates the energy of the incident photons, responsible for the created standing wave field. Bulk atoms are depicted in silver; adsorbates in purple, orange, red and yellow are positioned corresponding to coherent positions of 0, 0.25, 0.5, and 0.75, respectively. (C) Simulated NIXSW profiles for the adsorbates with different adsorption heights as shown in (A) and (B).

measurements require a synchrotron radiation source.

The standing wave field can be created by an X-ray beam (wavelength λ) hitting the sample crystal under Bragg scattering conditions:

$$n\lambda = 2d_H \sin(\theta) \tag{2.11}$$

with order n of the Bragg reflection, angle θ between incident wave and scatterer plane and the separation d_H of scatterer planes. The resulting standing wave field has the periodicity of the scatterer planes d_H. A very important feature of this standing wave field is the tunability of the phase. The Bragg reflection peak occurs over a finite range of incident angles and photon energies, which was shown by dynamical X-ray diffraction theory. [42] The reflection profile can be modelled by a Darwin-Prins curve (Figure 2.5). When scanning the photon energy or incident angle through the width of the Bragg reflection peak, the phase of the standing wave field shifts by π, which allows the determination of the position of adsorbates on the crystal: The absorption intensity and therefore also the photoemission intensity is proportional to the intensity profile of the standing wave field, which is maximal (minimal) for adsorbates on the antinodes (nodes) of the standing wave field. However, the width of the Bragg reflection peak depends on the incident angle [43] and is generally small, so that perfect crystallinity of the sample and a highly collimated beam would be required to perform measurements. [44] Close to normal incidence conditions, the width broadens significantly. This special type of measurement is called normal incidence X-ray standing wave (NIXSW), which softens the requirements on the sample and beam conditions and is used for all measurements performed for this thesis. By scanning through the Bragg reflection peak, the photoemission signal has a characteristic shape depending on the position z of the corresponding adsorbate (Figure

2.5), which can be determined using the following equation [43]:

$$I = 1 + R + 2\sqrt{R}\cos\left(\psi - \frac{2\pi z}{d_H}\right) \tag{2.12}$$

$$R = \left|\frac{E_r}{E_i}\right|^2 \tag{2.13}$$

where I is the measured photoemission intensity, ψ is the phase difference between the reflected and the incident wave, E_r and E_i are the the reflected and incident X-ray amplitudes, respectively. This equation however is only valid for adsorbates occupying a single vertical position with respect to the standing wave field. To account for multiple different adsorption sites or for dynamic effects like thermal vibrations, the equation can be modified in the following way [43]:

$$I = 1 + R + 2f_H\sqrt{R}\cos\left(\psi - 2\pi\frac{P_H}{d_H}\right) \tag{2.14}$$

Here two parameters are introduced: The coherent position P_H gives the average position within the standing wave field for an ensemble of atoms with a single photoemission peak and ranges between 0 and 1. The coherent fraction f_H is a measure for the degree of disorder, with values between 0 (e.g. random distribution of adsorbates or two adsorption heights differing by $d_H/2$) and 1 (all adsorbates at equivalent positions). It is worthwhile to note that the adsorption height D_H of an adsorbate above the scatterer plane can only be determined by the coherent position to a certain degree, as the addition of multiples of d_H does not alter the results of Eq. 2.14:

$$D_H = (n + P_H) \cdot d_H, n = 0, 1, 2... \tag{2.15}$$

Furthermore, f_H and P_H can also be considered as amplitude and phase of a Fourier component of the site distribution of the adsorbates. After obtaining more sets of f_H and p_H with different scattering planes of the crystal, one could obtain a real space image of the adsorbates on the surface by Fourier inversion [43]. While this requires in general measurements on many different scatterer planes, for adsorption on high symmetry sites on the crystal (e.g. bridge, atop, hollow site) already two different sets can suffice to determine the exact adsorption site.

In particular, for an fcc crystal surface in (111)-facing, combining the results of NIXSW measurements from (111) and $(1\bar{1}1)$ planes enables to determine above which of the different high symmetry sites of the substrate the adsorbate is located. Bridge adsorption sites occupy different positions with regard to the $(1\bar{1}1)$ plane, which lets the coherent factor drop to $f_{H,1\bar{1}1} \approx 0.33$ (Figure 2.6A, [43]). In contrast, fcc, hcp and atop sites have each a well-defined adsorption height with regard to the $(1\bar{1}1)$ plane (Figure 2.6), resulting in $f_{H,1\bar{1}1} \approx 1$. Each of these three sites can be distinguished by its coherent position $P_{H,1\bar{1}1}$, if the adsorption height above the crystal surface is known (Figure 2.6).

It should be noted that all coherent fractions will be usually lower due to vibrations of the atoms, which can induce a small variation of the adsorption height. This is usually accounted

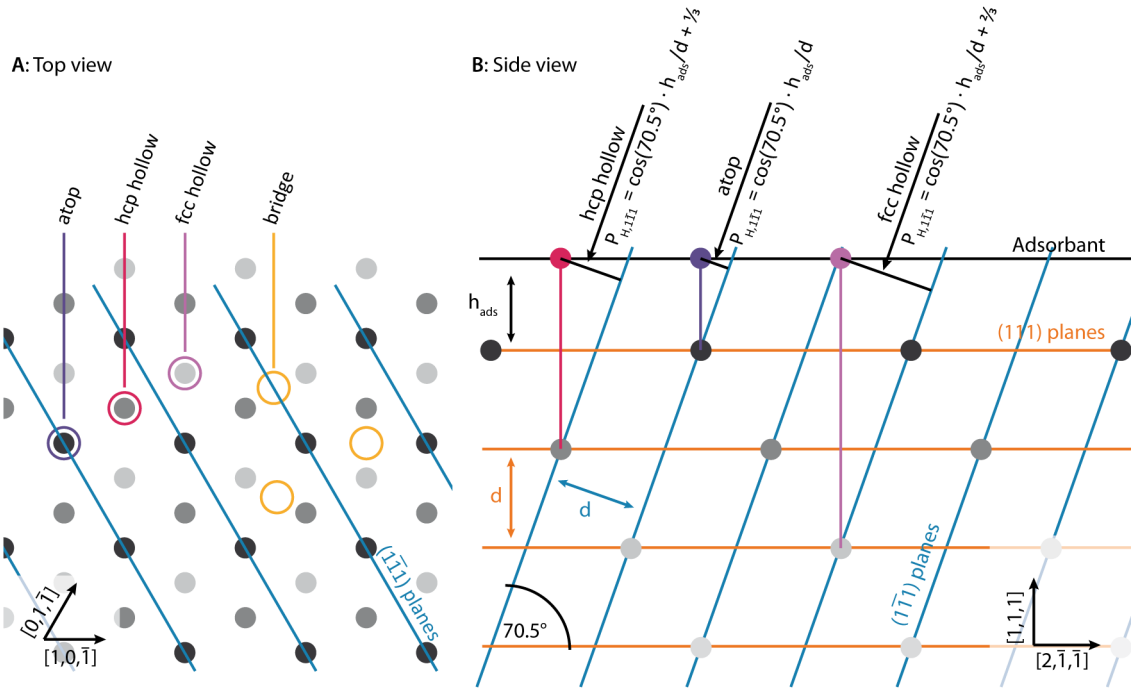

Figure 2.6 Scheme for the triangulation in NIXSW for a densely-packed (111) face of an fcc crystal. (A) Top view on the crystal, Top layer, second layer, and third layer atoms are marked in black, gray, and light gray, respectively. Examples for atop, fcc and hcp sites are circled in violet, raspberry and lavender, respectively. Three equivalent bridge sites are marked, indicating different positions with regard to the $(1\bar{1}1)$ planes. (B) Side view on the crystal, demonstrating the coherent positions $P_{H,1\bar{1}1}$ for the three different adsorption sites.

for by the Debye-Waller factor, lowering the measured coherent fractions by $\sim$10 % for small adsorbates at room temperature. [45]

Low-energy electron diffraction

Low-energy electron diffration (LEED) is a technique for the structural analysis of a surface. A beam of low-energy electrons (typically 5-100 eV) is focussed onto the surface with normal incidence (Figure 2.7). The mean free path of the electrons at low energies is approximately a few atomic layers, making this technique surface-sensitive. The de Broglie wavelength λ of electrons with energy E can be calculated by

$$\lambda = \frac{h}{\sqrt{2m_e E}} \tag{2.16}$$

The electron wavelength ranges typically between 0.1-0.5 nm, which is of the order of interatomic distances and therefore allows atomic diffraction. Before hitting the fluorescent screen, the backscattered electrons have to pass a retarding grid first: The first grid is grounded and ensures the propagation of the electrons from the sample in field-free space. On the following grids a potential is applied to reject inelastically scattered electrons. The fluorescent screen itself is biased to high voltage to accelerate the elastically scattered electrons onto the screen.

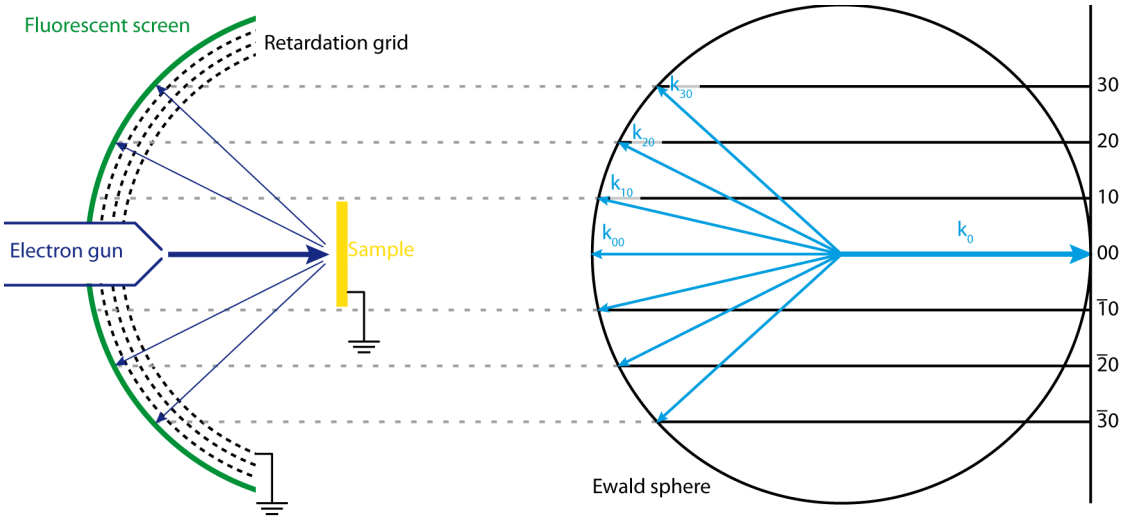

Figure 2.7 Schematic of a LEED setup and the elastic scattering condition. Electrons from the electron gun (purple) hit the sample (yellow), where the electrons are scattered. The retarding grids are adjusted in a way, that only elastically scattered electrons can pass and hit the fluorescent screen. The Ewald sphere on the right visualizes the condition for elastic scattering on a crystal surface. The scattered wave vectors have to be of the same length as the incident wave vector and point onto a reciprocal lattice rod. All vectors shown fulfill these requirements.

For elastic scattering the Laue condition must be fulfilled: [46]

$$\mathbf{k}_{sc} - \mathbf{k}_{in} = \mathbf{G} \tag{2.17}$$

$$|\mathbf{k}_{sc}| = |\mathbf{k}_{in}| \tag{2.18}$$

Here, $\mathbf{k}_{in}$ and $\mathbf{k}_{sc}$ are the incident and scattered wave vectors, respectively, $\mathbf{G}$ is a reciprocal lattice vector of the investigated substrate. This condition can be visualized via the Ewald construction (Figure 2.7), where the scattered wave vectors have to point to the intersections of reciprocal lattice rods and Ewald sphere. Therefore, the spots imaged in LEED reflect the two dimensional reciprocal lattice of the surface structure. In order to increase the contrast of the recorded images and decrease the beam current to reduce damaging of the sample, one can also employ a microchannel plate instead of the fluorescent screen. As these plates have a planar geometry compared to the spherical geometry of typical fluorescent screens, the enhanced contrast is accompanied by a distortion of the image inherent to the setup.

Temperature programmed desorption

Temperature programmed desorption (TPD) is a technique to characterize the desorption behavior of the adsorbates on a surface. Measurements are performed by heating the sample up with a linear temperature ramp while monitoring simultaneously the desorbing particles via a mass spectrometer. A common equation for the analysis of the acquired spectra is provided by the Polanyi-Wigner model: [47]

$$-\frac{d\theta}{dt} = \nu(\theta, T)\theta^x \exp\left(-\frac{E_D(\theta, T)}{k_B T}\right) \tag{2.19}$$

Here θ denotes the coverage of the investigated species, $\nu(\theta, T)$ a pre-exponential factor, x the order of the desorption, $E_D(\theta, T)$ the desorption energy, k_B the Boltzmann constant and T the temperature. The kinetics of the desorption process determine the order of desorption x, e.g. $x = 0$ for multilayer desorption, $x = 1$ for molecular desorption and $x = 2$ for recombinative desorption, however, the desorption order is not restricted to these examples. For desorption spectra that are acquired with a constant heating rate β the equation can be rewritten in the following way:

$$-\frac{d\theta}{dT} = \frac{\nu\theta^x}{\beta} \exp\left(-\frac{E_D}{k_B T}\right) \tag{2.20}$$

The rate of desorption $d\theta/dT$ is measured by a mass spectrometer close to the sample. While the mass spectrometer records the partial pressure of the investigated species, it was shown that with a sufficient high pumping speed the measured intensity in the mass spectrometer is proportional to the rate of desorption. [48, 49]

The analysis of temperature programmed desorption (TPD) spectra can be performed by various techniques. [47, 50–53] One difficulty in the analysis is the fairly large number of unknowns in the Polanyi-Wigner equation. In this case, the acquisition of coverage dependent data (multiple spectra with different initial coverage θ_0) or rate dependent data (multiple spectra acquired with different heating rates β) can help to narrow down some of the unknowns.

From coverage dependent data, the shape of the spectra can give an indication of the order of desorption (Figure 2.8A-C). For $x = 1$ the peak of the desorption rate is at the same temperature, irregardless of the initial coverage θ_0. In the case of $x < 1$, the peak of the desorption rate moves to higher temperatures for higher θ_0, in the case of $x > 1$ the peak moves to lower temperatures for higher θ_0. Therefore, the coverage dependent data can give an indication of the order of desorption x. The shape of the peak is also influenced by the order of desorption, being symmetric for $x = 2$ and more asymmetric in the other two shown examples, which can also be used to identify x. However it should be noted that these observations are not valid, if ν and E_D vary with coverage θ, which can be e.g. the case when attractive or repulsive interactions between adsorbates are observed.

Similarly, rate dependent data can give an indication of pre-exponential factor ν and desorption energy E_D. Figure 2.8D-F show rate dependent desorption curves with different ν/E_D, which are chosen such that the desorption maximum for $\beta = 10\,\mathrm{Ks}^{-1}$ is approximately at the same temperature in all three cases. While the desorption peak shifts in all cases towards lower temperatures for smaller β, this is most pronounced at smaller ν/E_D. Thereby, this shift can also give an indication of ν and E_D.

When fitting the data via numerical integration of the Polanyi Wigner equation, which was performed for fairly simple desorption processes and is further explained in chapter 3, such a preliminary analysis can allow to specify x, removing thereby one variable from the fitting process. While such a fitting can result in a very good agreement with the data, it necessitates to make several assumptions about the desorption behavior, e.g. the number of species, which are observed in a single spectrum, or temperature and coverage dependencies of ν and E_D.

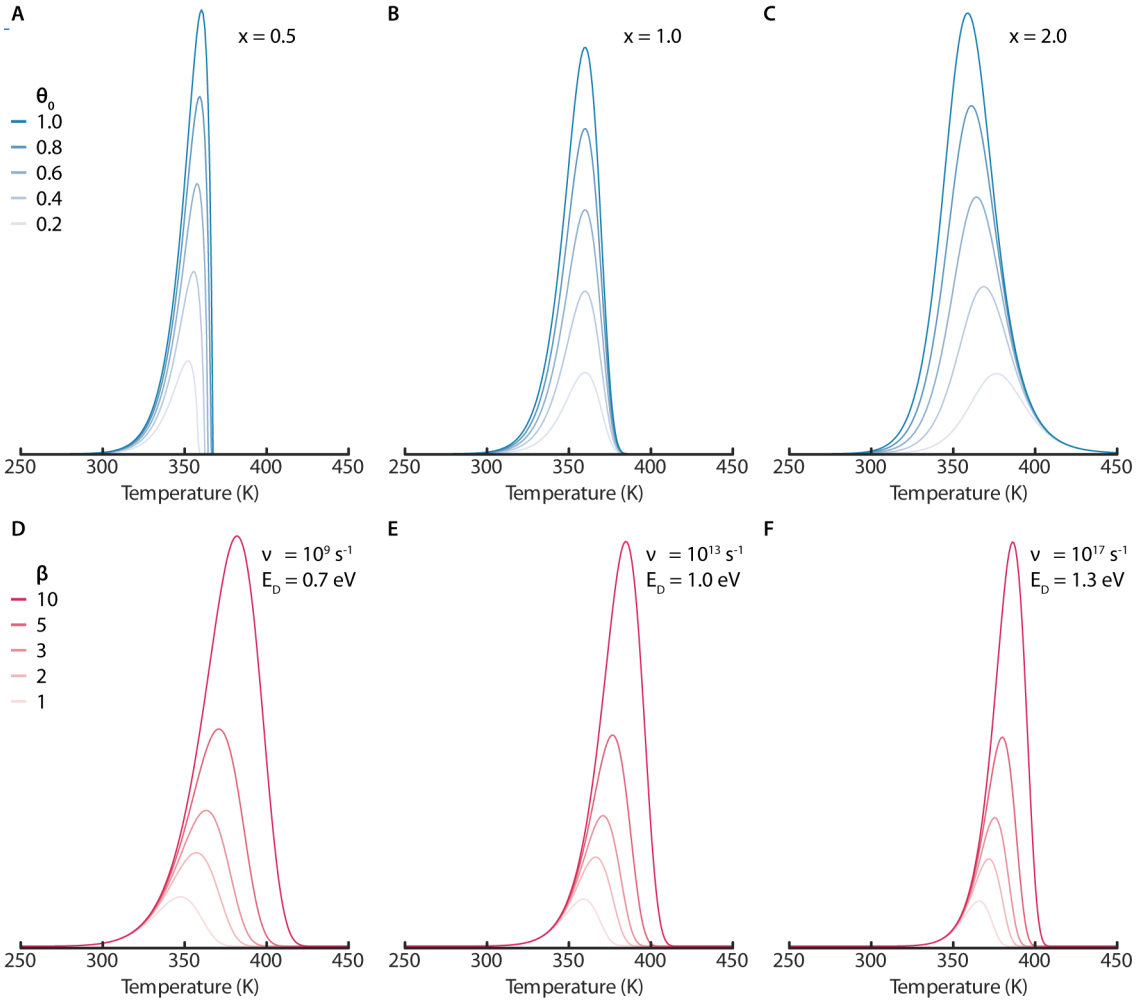

Figure 2.8 Simulation of different TPD spectra. (A-C) Spectra for different initial coverages θ_0 for desorption processes of different order, as indicated on each graph. The spectra were simulated with $\nu = 10^{13}\,\mathrm{s}^{-1}$, $E_D = 1.0\,\mathrm{eV}$, $\beta = 1$. (D-F) Spectra for different heating rates β, with parameters ν and E_D as indicated on each graph. Simulatione were performed with θ_0 = 1 and x = 1.

In the case of more complex spectra, it has been demonstrated that if desorption traces of more than one species are considered, different models can describe the data with similary high agreement. [54] Thus, a good agreement between fit and data can be obtained with a model, which is not reflecting the actual desorption process. Therefore, more complex spectra were analysed via the Redhead equation, [51] which allows to find an estimate for the desorption energy:

$$E_D \approx k_B T_P \left(\log \left(\frac{\nu T_P}{\beta} - 3.64 \right) \right) \tag{2.21}$$

Here, T_P is the peak temperature of the desorption trace, and if ν is not known, it is approximated from transition state theory as $\frac{k_B T}{h} \sim 10^{13}\,\mathrm{s}^{-1}$. While this equation includes various simplifications, it provides an estimation for the desorption energy E_D.

3 Technical implementation

Experiments for this thesis have been conducted at different experimental setups, which will be presented in this chapter. Most of the setups are based in E20 laboratories in Garching, the only exception is the I09 beamline at the Diamond Light Source (DLS) synchrotron in Didcot, UK. All experiments have been performed under ultra-high vacuum (UHV) conditions, with base pressures of 2×10^{-10} mbar or lower.

Variable-temperature STM (VT-STM)

The Aarhus-type VT-STM (SPECS) is set up in a UHV system (Figure 3.1), comprising a preparation chamber and an analysis chamber, which are separated by a gate valve (1). The preparation chamber includes a heating stage (2), with a parking lot for up to four samples attached, a sputter gun (5), a molecular dosing system (3, four-cell organic molecular beam epitaxy (OMBE) source by DODECON), a metal doser (4) and leak valves as gas inlets (7). As the position of the heating stage can only be adjusted in one direction, it is only used for heating and sputtering of the sample. For any deposition, the sample is held by a manipulator (axis perpendicular to the plane displayed in Figure 3.1, indicated by the dashed circle) with more degrees of freedom, allowing a more precise positioning of the sample accordingly to the desired process. The preparation chamber is evacuated via a turbomolecular pump.

The analysis chamber includes the STM (Figure 3.1, 8) and leak valves (7), enabling *in situ* dosing of gases during STM measurements and a sputter gun enabling *in situ* tip sputtering. A schematic of the STM is shown in Figure 3.2. The STM tip (4) is attached to a piezo scanner tube (5), allowing precise movements. On the bottom of the tube, a rod is firmly attached. This rod can be moved up and down by a piezo inchworm motor (6) for the approach and retraction of the STM tip in the range of several millimeters. The STM scanner is thermally and electrically decoupled from the main sample platform and the sample by quartz spheres (8). The STM sample (1) is mounted onto a double-decker sample holder (2). Two clamps (3) ensure a firm positioning of the sample on the large platform (10), which can be cooled down to allow imaging below room temperature (RT). In this case, sample and scanner platform are cooled down by liquid nitrogen (LN_2) via a cooling piston (11), while the STM scanner is counter-heated to RT by a zener diode (9). During measurements the cooling piston has to be drawn away from the scanner platform, so that the sample will slowly heat up to room temperature (RT). Here, the STM platform acts as a cold reservoir and slows down this process, so that the temperature of the sample increases by approximately $0.25\,\mathrm{K\,min^{-1}}$ at 130 K and less than $0.10\,\mathrm{K\,min^{-1}}$ at 230 K and above.

The analysis chamber is pumped by an ion pump, which requires no moving parts and is

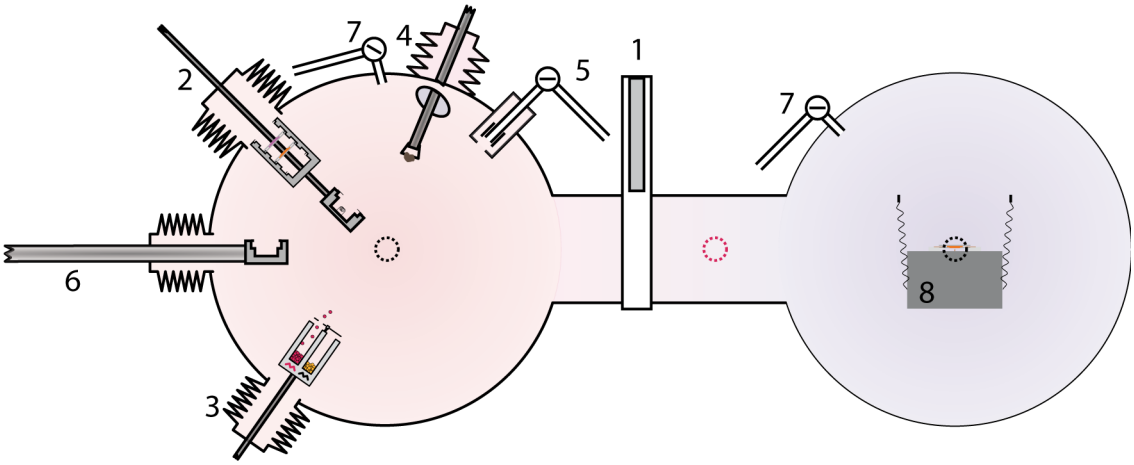

Figure 3.1 Schematic of the VT-STM UHV system, with preparation chamber (left) and analysis chamber (right), separated by a gate valve (1). The preparation chamber includes the heating and parking stage (2), a molecular doser (3), a metal doser (4), a sputter gun with an Ar gas inlet (5), a transfer arm (6) and a manipulator perpendicular to the shown plane (dashed circle). The analysis chamber includes a leak valve for gas inlets (7), the STM (8) and a manipulator for sample transfers (dashed circle). A load lock is attached to the analysis chamber (position indicated by red dashed circle).

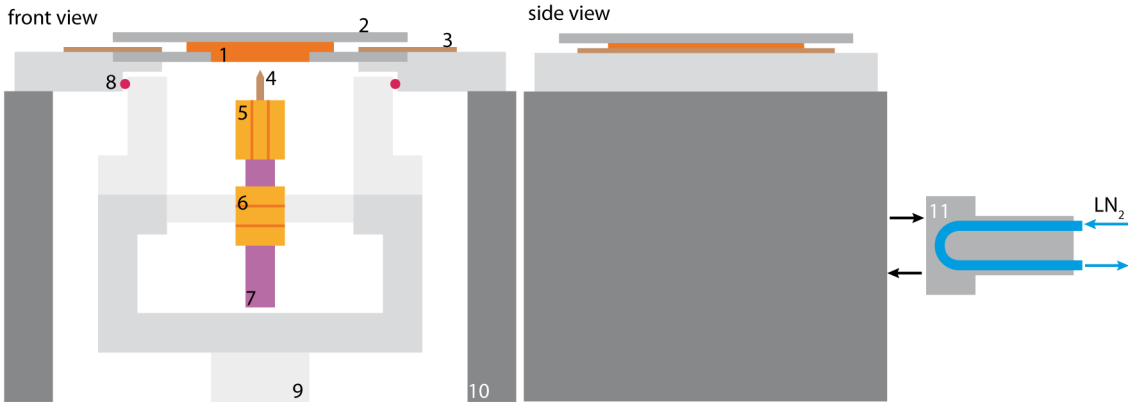

Figure 3.2 VT-STM schematics, with the following components: (1) Sample, mounted on (2) a double-decker sample holder. (3) Two clamps ensuring a stable positioning of the sample. (4) STM tip. (5) Scanner piezo tube. (6) Piezo inchworm motor, moving a rod (7) with the scanner piezo tube attached. (8) Quartz spheres, which decouple the scanner from the sample stage thermally and electrically. (9) Zener diode to heat the STM scanner. (10) Aluminium platform, acting as cold reservoir. (11) Cooling piston for measurements below RT.

therefore suitable for STM measurements by not introducing additional sources of noise.

Low-temperature STM (LT-STM)

This setup consists of a preparation and an STM chamber, separated by a gate valve. The preparation chamber allows sputtering and annealing of the sample, as well as deposition of molecules by an attached molecular evaporator. The STM chamber houses a Createc LT-STM, featuring an inner cryostat operated with liquid helium (LHe) which allows measurements at 5 K. The cryostat ensures that sample and the STM tip do not heat up during measurements, resulting in highly stable imaging conditions. Further information can be found in the thesis of K. Seufert. [55]

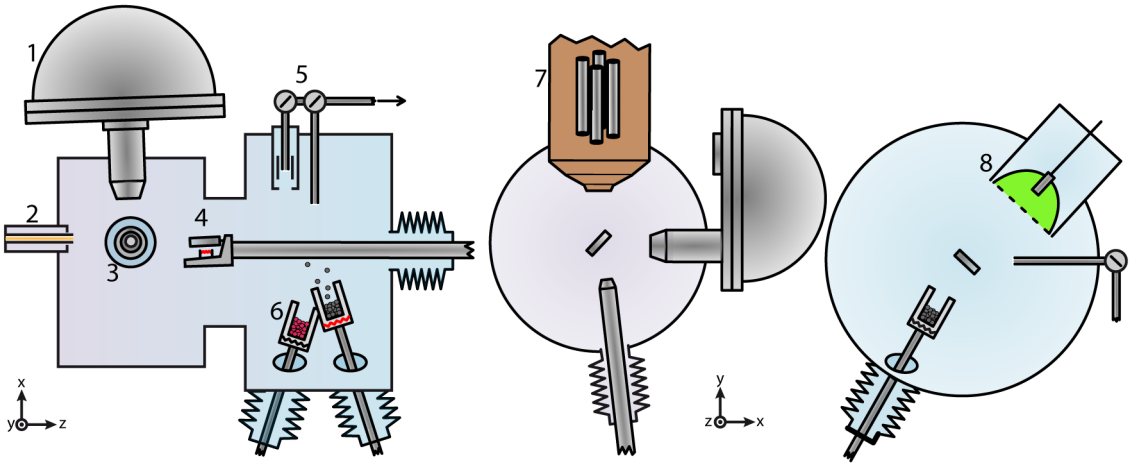

Figure 3.3 PSD chamber schematic from different perspectives, showing the following components: (1) the photoelectron analyzer, (2) the He source for UPS, (3) the X-ray source for XPS, (4) the sample mounted on the manipulator, (5) the inlet from the gas dosing system and the sputter gun, (6) the molecular evaporators, (7) the mass spectrometer, and (8) the LEED apparatus.

LT-STM/AFM

This UHV system is equipped with a CreaTec non-contact AFM (nc-AFM)/STM, from which the nc-AFM images as well as some high resolution STM images were acquired. A more detailed description of the chamber can be found elsewhere. [56]

PSD chamber

The PSD chamber (named after photon stimulated desorption) features instruments for the analysis of a sample by XPS, UPS, LEED and TPD. The layout is depicted in Figure 3.3. The left part of the chamber includes the photoelectron analyzer (SPECS phoibos 100 CCD, 1), a Helium lamp for UPS measurements (2), an X-ray tube, enabling non-monochromatic Kα radiation from either a Mg or an Al source, and a mass spectrometer (7), which is placed behind a copper cap to allow TPD measurements. The right part includes a LEED apparatus (BDL800IR-LMX-ISH by OCI Vacuum Microengineering Inc., 8), a sputter gun and an inlet from the gas dosing system with a pneumatically controlled valve (5), and the molecular evaporators (6). The sample on the manipulator (4) can be cooled down to $\sim$80 K by LN_2, in which case higher sample temperatures are obtained by counter heating. The temperature, measured by a K-type thermocouple directly attached to the sample, is controlled by a proportional-integral-derivative (PID) controller (Schlichting Physikalische Instrumente HS 130), which allows not only to measure the temperature precisely, but also to apply heating ramps, which are essential for TPD measurements. The manipulator allows rotations along the z-axis and movements along x-, y-, and z-axis, enabling the positioning the sample as required for each individual apparatus.

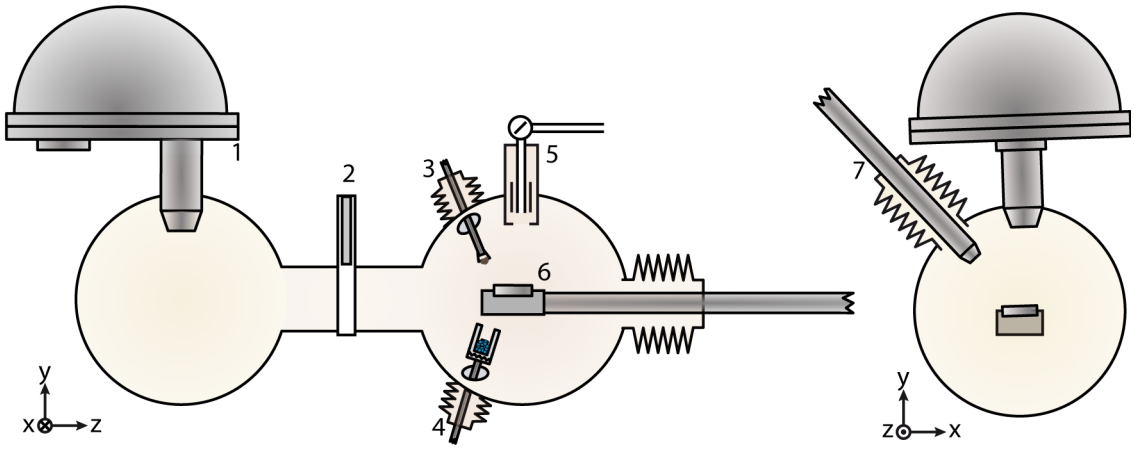

Figure 3.4 TUM - Walter Schottky Institute XPS chamber schematic, with the following components: (1) photoelectron analyzer, (2) gate valve to separate analysis chamber and preparation chamber, (3) metal evaporator, (4) molecular evaporator, (5) sputter gun, (6) manipulator with sample, (7) X-ray source.

TUM - Walter Schottky Institute XPS

This SPECS UHV system (see Figure 3.4) was used for XPS measurements. It includes a SPECS Phoibos 150 hemispherical analyzer (1) and a SPECS FR 50 X-ray source (7), supplying non-monochromatized Mg or Al Kα radiation. All instruments required for the sample preparation are mounted in a preparation chamber, which can be separated from the XPS analysis chamber by a gate valve (2). These instruments include a metal doser (3), a molecular doser (4), and a sputter gun (5). The sample on the manipulator is usually held at 300 K, but can be cooled down by LN_2 and heated up by a combined filament/electron-impact heating. The manipulator can perform movements in x-, y-, and z-direction and can be rotated along the z-axis.

I09 end-station at the Diamond Light Source

All NIXSW measurements have been performed at the I09 beamline at the DLS, a third generation synchrotron located in Didcot, UK. Two preparation chambers allow the *in situ* preparation of samples. Both chambers allow Ar^+ sputtering and thermal annealing of the sample. Additional instruments such as evaporators can be attached to the chambers via gate valves. The design of the system enables samples on the main manipulator to access all capabilities of one preparation chamber and the analysis chamber. This allows preparation and measurement below RT, without any temperature fluctuations due to sample transfers, which can be crucial in inhibiting desorption processes.

The analysis chamber features a hemispherical electron energy analyzer and a LEED setup, which were used to acquire XPS, NIXSW and LEED data. Two undulators allow to irradiate the sample with either soft X-rays (100-2100 eV) or hard X-rays (2.1-20 keV). [57] The intensity, energy and polarization of the incident X-rays can be adjusted as required for the specific experiments. A Scienta EW4000 HAXPES analyzer is employed, mounted perpendicular to the incident X-rays in the horizontal plane of the photon linear polarization.

Further information about the I09 beamline and about synchrotron light can be found in references. [57, 58]

Sample preparation

All samples were prepared using very similar procedures, which are elucidated in the following.

The preparation of a clean and atomically flat Ag(111) crystal was achieved by several cycles of Ne^+ (PSD-chamber) or Ar^+ (all other setups) sputtering and subsequent annealing to a temperature in the range of 630-725 K. The cleanliness of the crystal was assessed by STM or XPS.

The 1,4-di(1*H*-tetrazole-5-yl)benzene (BTB) molecules (synthesis described in [59], Figure 3.6) were dosed by OMBE on the Ag(111) surface held at RT following thorough outgassing in vacuo. The sublimation temperature was 523 K and resulted in a deposition rate of approximately $2.5\,\mathrm{molecules}\cdot\mathrm{nm}^{-2}\cdot\mathrm{h}^{-1}$.

Ru tetraphenyl porphyrin (Ru-TPP) (Figure 3.6) was deposited onto the Ag(111) crystal held at RT by heating Ru(CO)-TPP (Sigma Aldrich, 80 % dye content) at 550-625 K. By outgassing the crucible in vacuo, the dye content of the sublimed molecules can be further increased, as free base tetraphenyl porphyrin (2H-TPP) sublimes at slightly lower temperatures and is therefore removed from the crucible. For temperatures above approximately 560 K, the CO detaches from the Ru-TPP, allowing to deposit clean Ru-TPP monolayers. At evaporation temperatures below 560 K, the CO remains attached. However, with the crystal held at RT the CO desorbs from the contact layer, resulting also in the deposition of a clean monolayer of Ru-TPP. Nevertheless, on the second layer and above the CO is preserved on the Ru-TPP. The deposition rates were $0.3\text{-}2.0\,\mathrm{molecules}\cdot\mathrm{nm}^{-2}\cdot\mathrm{h}^{-1}$, depending on the crucible temperature and chamber geometry.

By annealing a layer of Ru-TPP molecules at 620 K for 10 min, intramolecular cyclodehydrogenation reactions induce the formation of planarized Ru-TPP derivatives. [60] Four different products can be observed, which are shown in Chapter 5.

The masked 1,3-dimethyl-2*H*-imidazol-1-ium-2-ide (IMe) (1,3-dimethyl-1*H*-imidazol-3-ium-2-carboxylate (IMe-CO_2), Figure 3.5) was synthesized according to a reported procedure. [61] The free IMe was deposited by heating the masked IMe to 360-390 K (Figure 3.5). [61] No evidence of the parent ions of IMe-CO_2 or dimerized IMe was found in mass spectrometry during deposition or desorption. The co-adsorption of CO_2 can be excluded because no traces of oxygen were detected by XPS. Deposition rates of up to $10\,\mathrm{molecules\,nm}^{-2}\,\mathrm{h}^{-1}$ were used for Ru-TPP monolayer samples held at 300 K. Deposition rates with the substrate held at 200 K were up to 5 times higher.

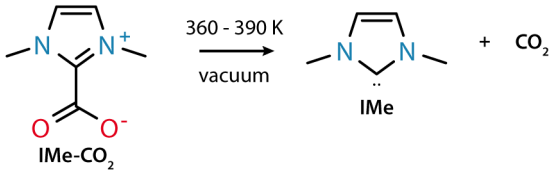

Figure 3.5 Decomposition of the masked IMe (IMe-CO_2, left) into the free IMe and CO_2, occurring when heated to the indicated temperature range in vacuum. [61–63]

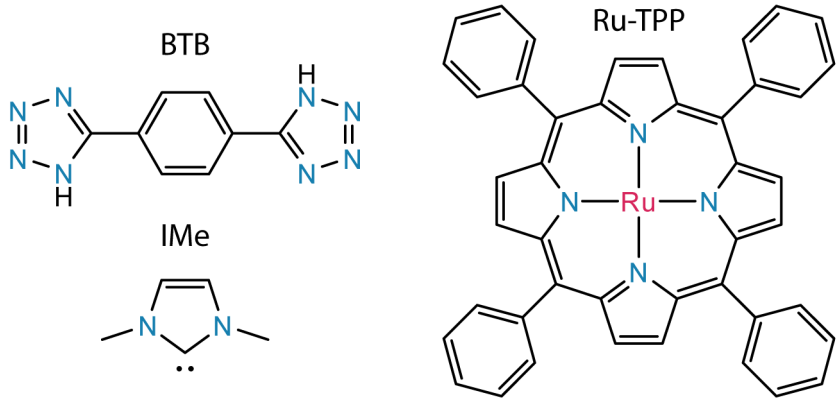

Figure 3.6 Structural formulas of the different employed molecules.

At the VT-STM, the LT-STM, and the I09 beamline a commercial OMBE source (DODECON nanotechnology GmbH) was used for molecular deposition, at the NIM-XPS and PSD home built sources were employed.

CO was dosed in the PSD chamber via a gas dosing system [64], which allows the dosage of defined amounts of gases via a needle-doser. At the other chambers, gas was dosed via leak-valves, where the total dosage was estimated by the exposure time and the increase of the pressure in the chamber.

Fe was deposited via a home built metal evaporator. A thin Fe wire is wrapped around a thermally more durable W wire. Heating resistively the W wire and thereby also the Fe wire enables the sublimation of Fe, which is thereby deposited onto the crystal.

Data acquisition and analysis

STM

All STM images were acquired with chemically etched W tips, with the STM operating in the constant current mode. The tunneling bias was applied to the sample. The analysis of STM images was performed by gwyddion [65] and routines written for IGOR Pro 6.3. Several routines for IGOR Pro 6.3 have been added to facilitate the image analysis: Firstly a routine allowing the import of STM image and spectroscopy files from the Aarhus VT-STM.

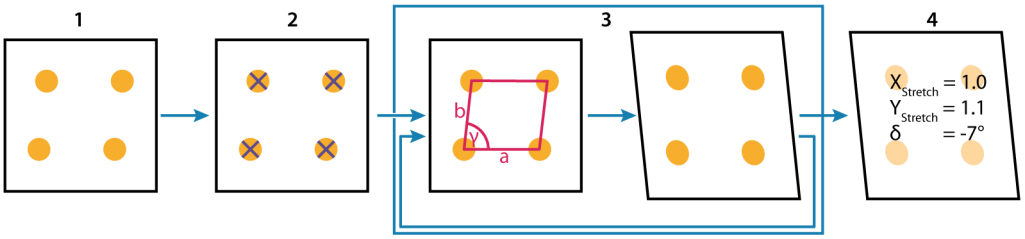

Figure 3.7 Automated calibration process for STM images. (1) An image with a square or hexagonal pattern of well-defined dimensions needs to be selected. (2) The regular pattern is marked manually. (3) The calibration routine is measuring the actual dimensions of the marked structure and computes correction parameters $X_{Stretch}, Y_{Stretch}$, and δ. For higher accuracy of the correction this process is repeated multiple times, until the change in δ between iterations is $< 0.000\,01°$. (4) The routine stops and returns the calibration parameters, exemplary parameters are displayed.

Secondly, a routine to extract calibration parameters of STM images to account for image distortions (Figure 3.7). It requires an image showing a structure, which is either rectangular or hexagonal and where the dimensions are known (e.g. atomic resolution of Ag(111)). The corners of such a hexagon/square have to be marked on the image. Then the routine stretches/compresses the image in x- & y-directions and additionally tilts the y-axis to fit the marked structure with the given dimensions. Additionally, a routine to apply these calibration parameters during the import of images has been included.

Images were processed by subtracting a plane background, in a few cases also by two dimensional (2D)-fast Fourier transform (FFT) filtering to remove noise. If not further specified, STM images were acquired at 300 K.

XPS / UPS

XPS data from the TUM - Walter Schottky Institute XPS and the PSD have been analyzed via routines for IGOR Pro 6.3, XPS data from the synchrotron has been analyzed via Matlab routines (developed by D. Duncan). In both cases, similar features are implemented, including background subtraction and peak fitting with Voigt profiles. UPS data is shown as recorded without any background subtraction. The binding energy scale was corrected either via the Fermi edge (C 1s and Ru 3d region from synchrotron data, UPS data) or via the Ag $3d_{5/2}$ peak at 368.27 eV (all other data).

TPD

Measurements were performed using a quadrupole mass spectrometer inside a copper cap, [66, 67] with the sample located at a distance of approximately 1 mm from the opening on the apex of the copper cap.

For the presented TPD analysis we developed Matlab routines. These offer the import of the data (based on routines developed by P. Deimel) and additionally options for background subtraction and normalization. The normalization requires a reference spectrum with a well-defined initial coverage, which is usually a desorption spectrum from a saturated layer, i.e. the initial coverage $\theta_0 = 1$. The intensity of the spectrum is then scaled such that the time-integrated area equals the initial coverage θ_0. All other spectra, recorded under the

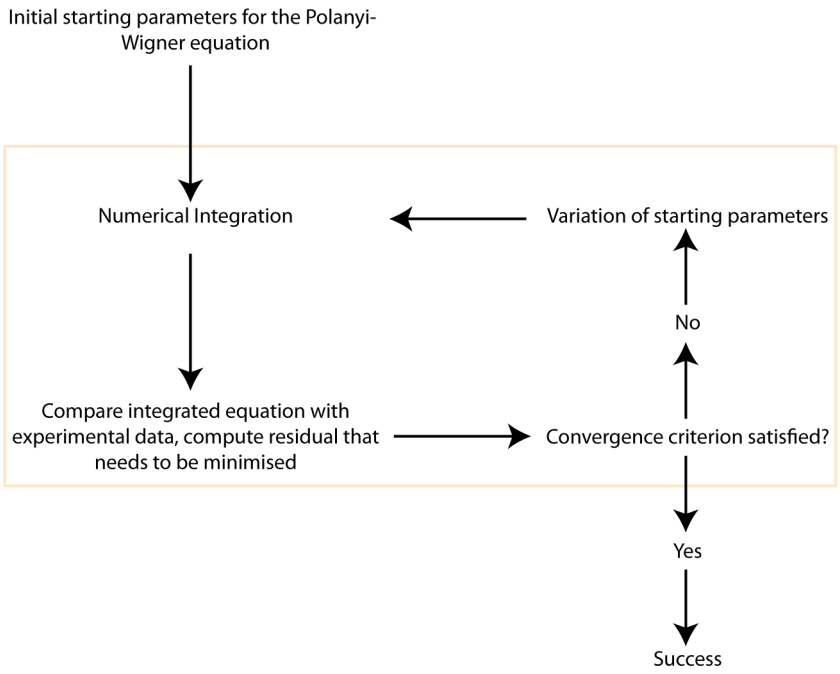

Figure 3.8 Flowchart of the fitting procedure using the *fminsearch* routine implemented in Matlab. An adequate set of starting parameters is recommended to reduce computation time and minimize the risk of obtaining a local minimum as the final result.

same conditions, but with different θ_0, are normalized using the same parameters. The initial coverage of each spectrum can be determined by comparing its integrated area, which is proportional to θ_0, with the reference spectrum.

For further analysis, it was assumed that the TPD spectra can be described via the Polanyi-Wigner equation (see Eq. 2.20). The objective was to write a routine that allows to fit simultaneously multiple spectra (which might differ in initial coverage or in the applied heating rate). This allows to fit all available data with a single routine in order to achieve the best match between the experimental data and the modeling and is achieved by the use of the optimization method *fminsearch*, a nonlinear solver implemented in Matlab, which works as described in the following.

First, with the given set of starting parameters, the Polanyi-Wigner differential equation is numerically solved via the ode45 (ordinary differential equation) solver, which is implemented in Matlab. This has to be done for each spectrum individually, as the starting parameters can be different. As a second step, the quality of the fitting is assessed by calculating the squared difference between measurement and fit. To ensure that all spectra contribute equally, the difference is assessed for all spectra at the same temperatures, implemented by interpolating the data of all but the first spectra. The sum of the squared differences indicates the quality of the fitting and needs to be minimized. This is done directly by the *fminsearch* method, which repeats the aforementioned steps while adjusting the starting parameters until a minimum is found (Figure 3.8). This method has no limitation on the number of unknowns, which are varied in order to find the minimum. This allows to introduce additional dependencies for the variables, e.g. temperature or coverage dependencies. A simple coverage dependence of

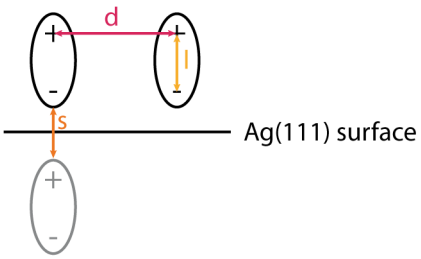

Figure 3.9 Scheme of the dipole-dipole interaction. The two dipoles (black ellipses) are separated by distance d, the charges in each dipole are separated by l, the distance between dipole and image dipole (grey) is s.

the desorption energy could be implemented in the following way:

$$E_D = E_{D,0} + E_{D,\theta} \cdot \theta \tag{3.1}$$

Here, $E_{D,0}$ denotes the desorption energy in the no coverage limit, while $E_{D,\theta}$ is the coverage dependent component.

This method can also be easily adapted into fitting multiple Polanyi-Wigner equations for each spectrum, if it cannot be described by a single desorption process. One constraint is however, that the equations for the single desorption processes can be separated, i.e. the single components are not correlated:

$$-\frac{d\theta}{dT} = \sum_i \frac{\nu_i \theta_i^{x_i}}{\beta} \exp\left(-\frac{E_{D,i}}{k_B T}\right) \tag{3.2}$$

Dipole strength estimation

A coverage dependent desorption energy (see Equation 3.1) can be the result of dipole interactions between the adsorbates. After acquiring $E_{D,\theta}$ from a fit, the corresponding dipole moment of the adsorbates can be estimated via a simple model on the basis of Coulomb-interactions between dipoles. The potential energy E_{pot} between two point charges q_1 and q_2 with a separation r is given by

$$E_{pot} = \frac{1}{4\pi\epsilon_0}\frac{q_1 q_2}{r} \tag{3.3}$$

To extend this to dipoles, the two charges of each dipole, separated by distance l, have to be considered. A superposition of energy contributions from surrounding dipoles, assuming a full coverage of the adsorbate, leads to the following equation.

$$E_{Dip} = \frac{q^2}{4\pi\epsilon_0} \sum_{i=1}^{N} \left(\frac{2}{d_i} - \frac{2}{\sqrt{d_i^2 + l^2}}\right) \tag{3.4}$$

Including now as a last step image dipoles, induced by the conductive Ag(111) substrate, we

obtain

$$E_{Dip} = \frac{q^2}{4\pi\epsilon_0} \sum_{i=1}^{N} \left(\frac{2}{d_i} - \frac{2}{\sqrt{d_i^2 + l^2}} + \frac{2}{\sqrt{d_i^2 + (l+s)^2}} - \frac{1}{\sqrt{d_i^2 + s^2}} - \frac{1}{\sqrt{d_i^2 + (2l+s)^2}} \right) \tag{3.5}$$

Here s is the distance between a dipole and its image dipole (see Figure 3.9). Calculations were performed including up to 40000 surrounding molecules to estimate the dipole moment.

NIXSW

NIXSW data were acquired at the I09 beamline at the DLS. Measurements for the (111) planes, parallel to the surface, and $(1\bar{1}1)$ planes, tilted by 70.53° with respect to the surface, were performed at a normal incidence Bragg energy of $h\nu = 2.63\,\mathrm{keV}$. All measurements were repeated multiple times at different spots of the sample, where at each spot the reflectivity curve was measured to allow a precise energy alignment of the individual NIXSW measurements and to ensure the crystalline quality of the Ag(111). Monitoring potential beam damage was performed by recording XP spectra of the C 1s and Ru 3d region before and after each NIXSW measurement. All fitting procedures for the NIXSW data were adapted from Matlab routines developed by D. Duncan and M. Schwarz.

DFT

The Quantum ESPRESSO package [68] was employed for the density functional theory (DFT) geometry optimisation. Within the vdW-DF2-B86r approximation [69, 70] in the exchange-correlation term, five layers of the silver substrate were considered, the two lower layers fixed at their bulk-terminated positions. An optimized lattice constant of 4.1325 Å, 2 × 2 k points, Fermi–Dirac smearing of occupation numbers with a 50 meV broadening, projector augmented wave [71] data sets for the pseudization of the core electrons, surface–dipole corrections, and cutoff energy of 60 Ry for the wave functions and 350 Ry for the electron density were applied. For the Ru-TPP square phase, also with CO or IMe ligated to the Ru center, the unit cell derived from LEED and STM containing two molecules was used. For the planarized Ru-TPP derivative, a unit cell of the same size with an isolated molecule was used.

AFM-simulation

The simulations of AFM images based on the geometries found by DFT were acquired by the probe particle model (https://nanosurf.fzu.cz/pprmodel.php). It uses empirical potentials to model the interaction between the tip and the molecular layer [72]. All simulations in this thesis use the potential model for a CO functionalized tip.

4 Self-assembly and metal adatom coordination of a linear bis-tetrazole ligand on Ag(111)

This chapter includes content that has been published in

P. Knecht, N. Suryadevara, B. Zhang, J. Reichert, M. Ruben, J. V. Barth, S. Klyatskaya, A. C. Papageorgiou, **The self-assembly and metal adatom coordination of a linear bis-tetrazole ligand on Ag(111)**, *Chem. Commun.*, 2018, **54**, 10072-10075. Reproduced with permission from the Royal Society of Chemistry.

The functionalization of metal surfaces with azole compounds and in particular triazole and tetrazole compounds has attracted interest due to their corrosion inhibiting properties. [73, 74] More recently, triazole and tetrazole ligands have been employed in the formation of coordination polymers with functional properties ranging from fluorescence [19] and second harmonic generation [19] to spin crossover (SCO) phenomena. [20] The tetrazole group with its four nitrogen atoms is known to show distinct types of coordination nodes for the formation of metal organic coordination networks. While the tetrazole can act as both a dinucleating ligand and a trinucleating ligand, the deprotonated tetrazolate can engage in coordination bonds with up to four metal atoms. [75] Here we investigate 1,4-di(1*H*-tetrazole-5-yl)benzene (BTB), consisting of a benzene with tetrazole groups at the 1 and 4 positions (Figure 4.1), as a very promising ligand for metal-organic frameworks (MOFs): it couples the coordination properties of two tetrazole ligands and offers tunability of size via implementation of additional backbone units. MOFs with Ag, [76] Cu, [76] and Fe [20] nodes are reported to form under hydrothermal conditions and have demonstrated SCO phenomena. [20]

To the best of our knowledge, the surface coordination chemistry of tetrazoles is hitherto unexplored, although compounds with the related triazole group have been studied. On the more inert Au(111), hydrogen bonding drove the self-assembly of benzotriazole. [77] On Cu(111) triazoles are found to bind with a triazole group either oriented towards the substrate or creating a planar node with a native Cu adatom. [78–80] On highly oriented pyrolytic graphite (HOPG) the addition of Cu adatoms results in the formation of Cu^{2+}. [81]

Here we investigate the afore described tetrazole linear linker (Figure 4.1) ultra-high vacuum (UHV) conditions via scanning tunneling microscopy (STM) to obtain real space images of the self-assembly with molecular resolution, and X-ray photoelectron spectroscopy (XPS) to get information about the chemical state of the elements on the surface. We thus gain the first experimental atomistic scale insight of the binding of tetrazole moieties on Ag(111).

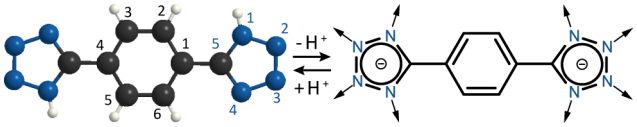

Figure 4.1 Ball-and-stick model of BTB and possible coordination modes of the tetrazolate anion. Carbon, nitrogen and hydrogen atoms are black, blue and white, respectively. The atom numbering is indicated

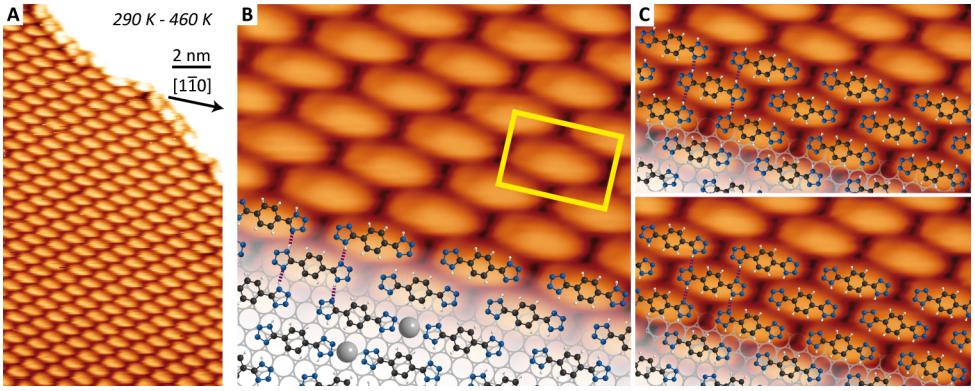

Figure 4.2 RT self-assembly of BTB on Ag(111) (phase α, observed after annealing in the indicated temperature range). (A) Large scale STM image (-1.25 V, 90 pA), the Ag [$1\bar{1}0$] direction is indicated. (B,C) Detailed STM (1.25 V, 110 pA) overlayed with a model (B: *trans* isomer, C: *cis* isomer). The unit cell is marked in yellow in (B). The ball-and-stick model is based on the crystal structure. [91] Black, blue, and white spheres represent carbon, nitrogen and hydrogen, respectively. Gray spheres mark possible position of metal adatoms (Ag and/or Fe). Empty gray circles represent substrate atoms. Purple dotted lines indicate hydrogen bonding between nitrogen atoms.

Furthermore, we exploit our *in situ* sample preparation methodology for the formation of such metal-organic networks at the vacuum-solid interface, which combines a clean synthesis without any solvents with a great control of the thickness by adjusting the dose of sublimed molecules. [82] We note that metal organic coordination networks are a current topic of intense investigation, [83–87] and recently enhanced cooperativity for supported SCO networks was predicted. [88]

Self-assembly on Ag(111)

Initially, we investigate the room temperature (RT) self-assembly of BTB on the Ag(111) surface, where mobile Ag adatoms are known to be present. [89, 90] Shortly after the molecular deposition, elongated protrusions appear on the STM images along the [$1\bar{1}0$] direction (Figure 4.2), coexisting with a 'sea' of diffusing molecules. These protrusions are consistent with the molecular dimensions of BTB adsorbing planarly on the metallic surface. The overview image in Figure 4.2A evidences the formation of a self-assembled close-packed two dimensional (2D) island (phase α), which is characterized by a commensurate unit cell $\begin{pmatrix} 5 & 0 \\ 2 & 4 \end{pmatrix}$ (see Figure 4.2B) and has been the sole structure observed after annealing to temperatures of up to 390 K.

We propose that these islands consist of BTB in the *trans* configuration (Figure 4.2B). Here each unit cell contains two BTB *trans* molecules, one in each surface enantiomeric form; that is the two molecular *trans* configurations in this model result by a mirror and translation

operation and cannot arise from any combination of rotation plus translation operations. The structure is stabilized by the NH$\cdots$N hydrogen bondings indicated by purple dotted lines in Figure 4.2B. The proposed model is in analogy to the hydrogen bonded structures found in single crystals of BTB [91] with the projected N$\cdots$N separation measured as 2.9 Å *vs.* 2.8 Å. [91] We note that in the STM the two isomeric forms cannot be distinguished and it is also possible to model phase α solely with *cis* isomers (Figure 4.2C), which can be placed in two different ways, not distinguishable by the STM. The spacing of the tetrazole units along the Ag[$1\bar{1}0$] and the epitaxial unit cell is consistent with a scenario whereupon Ag adatoms are located at bridge sites and further stabilize the network by metal coordination (Figure 4.2B). The Ag adatom was not directly evidenced in our STM data, similarly to Ag adatoms in coordination nodes of two *ortho*-benzoquinone moieties. [92] This type of on-surface coordination is not unprecendented on Ag(111) (coordination of four iminic N atoms with a Ag adatom after annealing at 383–443 K was proposed recently, [93] whereas free base porphyrins are complexing Ag after annealing above 530 K). [94] However, this would be the first report of such coordination of surfaces already at RT and its plausibility will be discussed along with the XPS data. Complementary XPS measurements confirmed that the intact molecule was present on the Ag(111) following RT deposition. The relevant C 1s spectrum (Figure 4.3A, left) shows two main components, which can be related to the carbon atoms of the benzene (285.2 eV, blue) and the tetrazoles (287.3 eV, yellow), respectively, with the expected ratio of $\sim$3:1. In the corresponding N 1s spectrum, we also identify two peaks at 401.3 eV (blue) and 400.0 eV (violet) in a ratio of $\sim$3:1. The former corresponds to the combined contribution of the aminic N [95, 96] and iminic N atoms bound to two nitrogen atoms, [97] the latter to the iminic N atoms bonded to a single N atom. [97, 98]

XPS reveals that at RT the deprotonation of the N1 atoms occurs slowly and concomitantly with N-Ag coordination at the N2/N3 atoms. Figure 4.3B shows measured spectra on the same samples as the one shown in Figure 4.3A, albeit recorded $\sim$18 h later.The lower energy component of the N 1s region (Figure 4.3B, right) increases in relative intensity, as a result of a shift of the N1 contribution by $\sim$1.3 eV towards lower binding energy, commonly associated with aminic N deprotonation. [95]

The C 1s spectrum (Figure 4.3B, left) shows a splitting of the peak related to the tetrazole carbon. [99] However, one can notice that the C 1s signal reveals only $\sim$50 % of the tetrazole units to be deprotonated as the intensities of the components at 287.0 eV (yellow in Figure 4.3B) and 286.0 eV (green in Figure 4.3B, corresponding to deprotonated nearest N neighbour) are approximately equal. Therefore the total intensity of the N 1s component at 399.6 eV has further contribution from a shift of the iminic N components with two N nearest neighbours (for relative intensities of different components see Table 4.1). Such a shift would be consistent with a scenario of metal coordination with Ag adatoms. [99] These observations substantiate the model with Ag adatoms in the densely packed phase α (Figure 4.2B).

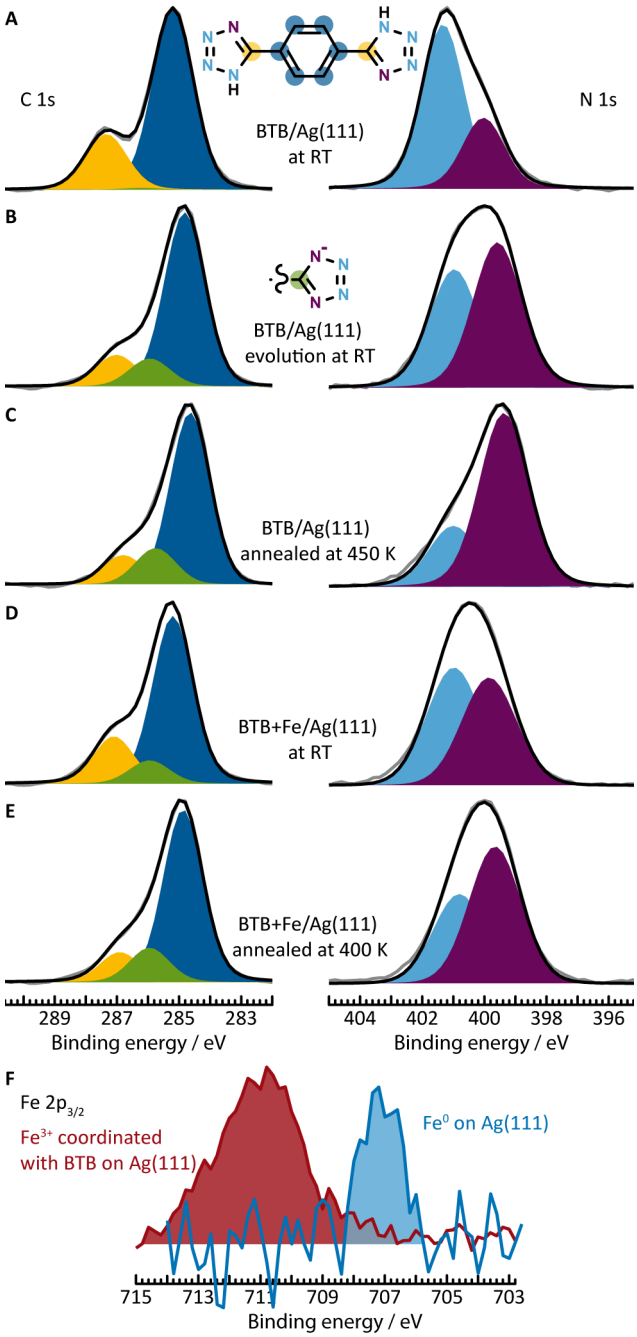

Figure 4.3 XPS measurements. (A-E) C 1s and N 1s regions corresponding to: (A) ∼1 monolayer of BTB on Ag(111) at RT showing intact molecules after sublimation; (B) deprotonation of aminic N atoms and Ag coordination occuring slowly at RT (recorded 18 h after sublimation); (C) higher degree of N deprotonation and Ag adatom coordination after annealing at 450 K (∼4 h after sublimation). (D) monolayer BTB and Fe atoms in a ratio of ∼6:1 (Table 4.1, 4.2) dosed sequentially on Ag(111) at RT evidencing both deprotonation of aminic N and coordination of iminic N to Fe (∼2 h after sublimation); (E) both of these processes are promoted by annealing to 400 K (∼4 h after sublimation). F: Fe $2p_{3/2}$ spectra for Fe on the bare Ag(111) surface (blue, 707.2 eV) and Fe with excess BTB on Ag(111) (red, 711.0 eV) show that all the Fe is coordinated with the tetrazole molecules and shifts to a higher oxidation state.

Table 4.1 Binding energies (BE) and relative intensities (rel. I) of C 1s and N 1s spectra presented in Figure 4.3. Assignments A-E correspond to the A-E spectra in Figure 4.3.

	C 1s of protonated tetrazole (yellow)		**C 1s** of deprotonated tetrazole (green)		**C 1s** of benzene (blue)	
	BE (eV)	rel. I	BE (eV)	rel. I	BE (eV)	rel. I
A	287.3	24 %	286.2	1 %	285.2	75 %
B	287.0	14 %	286.0	12 %	284.8	74 %
C	286.8	12 %	285.8	15 %	284.6	73 %
D	287.1	20 %	286.0	10 %	285.2	72 %
E	286.9	13 %	286.0	15 %	284.9	74 %
	N 1s (blue)		**N 1s (violet)**			
	BE (eV)	rel. I	BE (eV)	rel. I		
A	401.3	70 %	400.0	30 %		
B	401.0	46 %	399.6	56 %		
C	401.0	26 %	399.4	74 %		
D	401.1	52 %	400.0	48 %		
E	400.8	40 %	399.7	60 %		

Table 4.2 Atomic ratios of C, N and Fe in the samples characterized by XPS, based on spectra with identical acquiring conditions and normalizing with the photoionization cross sections at the energy of the Mg K_α line. [100]

	C 1s	**N 1s**	**Fe 2p$_{3/2}$**
intensity (a.u.)	1.32×10^5	2.13×10^5	3.87×10^4
atomic ratio	52 %	47 %	1 %

Phase transformation upon thermal annealing

Upon annealing the sample at 430 K, two additional phases β and γ can be observed by STM measurements (see Figure 4.4). The amount of deprotonated tetrazoles is $\sim$60 % after annealing (ratio of green component to total contributions from tetrazole carbon atoms in Figure 4.3C, left). We therefore infer that the N1 of both tetrazole moieties of each molecule are deprotonated in phases β and γ.

In phase β (green unit cell in Figure 4.4A) the presence of Ag adatoms is inferred based on the XPS evidence of Figure 4.3C, which shows the majority of N signal shifted to lower binding energy as a combined effect of N deprotonation and N-Ag coordination. STM images seldom evidenced the presence of single Ag adatoms (Figure 4.4C). We propose two Ag adatoms between the tetrazole groups of two molecules with a projected Ag-N distance of $\sim$2.2 Å (indicated in Figure 4.4B), which is in good accordance with reported Ag-N bond lengths of tetrazole moieties. [101] The molecules assemble in a higher order coincidence superlattice (three different adsorption sites on the Ag(111) substrate) with the epitaxy matrix $\begin{pmatrix} \frac{8}{3} & \frac{5}{3} \\ 3 & 6 \end{pmatrix}$. In phase γ (yellow unit cell in Figure 4.4A), the presence of Ag adatoms can be identified commonly in the STM image as broad round protrusions. Close inspection of the unit cell dimensions reveals that each of these protrusions is best fitted with three Ag adatoms. Similar nanodots have been observed with Cu adatoms in 2D coordination networks. [102] Two additional Ag adatoms per unit cell are evidenced under the same imaging conditions as the adatoms in phase β (Figure 4.4C). We therefore infer that single Ag adatoms are not necessarily visible in STM images, whereas a trimer of Ag adatoms would be routinely discernible.

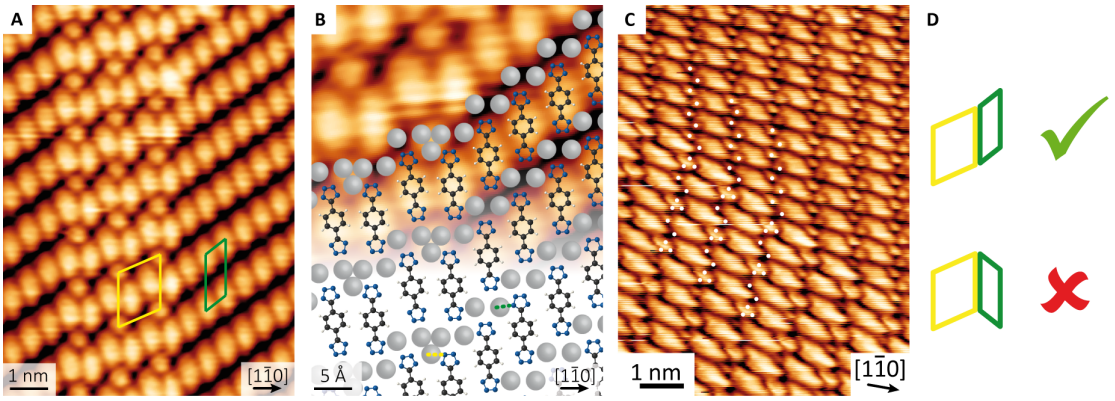

Figure 4.4 Ag adatom coordination of BTB. (A) STM (1.75 V, 110 pA) of the structures formed after annealing in the indicated temperature range, unit cells of phases β and γ are depicted in green and yellow, respectively. (B) Molecular model including Ag adatoms (gray spheres). The shortest Ag-N bonds are depicted in green and yellow for phases β and γ, respectively. (C) STM (-0.63 V, 90 pA) of phases β and γ, where protrusion between the molecules can be discriminated. White dots represent the proposed position for Ag adatoms. (D) Schematic of transitions between phases β (unit cell in green) and γ (unit cell in yellow). Only transitions shown on the top (and symmetrically equivalent) have been observed. No transition as shown on the bottom was detected, indicating the chiral recognition in the interface of these two phases.

The projected Ag-N distances between nitrogen atoms of the tetrazoles and silver adatoms are 2.3 Å. The unit cell comprises two molecules and five Ag adatoms and is commensurate: $\begin{pmatrix} 5 & 2 \\ 3 & 6 \end{pmatrix}$. Transitions between both structures, β and γ, can be observed along the $[1\bar{2}1]$ directions of the Ag(111) and exhibit organisational chiral recognition (Figure 4.4D).

Phase transformation upon Fe coordination

Targeting metal-organic networks with magnetic properties, such as SCO phenomena, we explored the coordination with Fe, which occurs readily at RT after sublimation of BTB and Fe adatoms on the clean Ag(111) surface, identified by an Fe oxidation state, distinctively different than metallic Fe on Ag(111) (Figure 4.3F) and consistent with literature values of Fe^{2+}/Fe^{3+}. [103] As under these conditions, the STM images do not identify any other structure formation as the densely packed phase α, the Fe is assumed to be incorporated in that phase similarly as proposed in the model in Figure 4.2B (gray spheres). Since the molecular XPS signatures do not change significantly in the presence of Fe adatoms, we propose that Fe displaces Ag in the coordination nodes. Based on the number of tetrazole ligands and the Fe 2p binding energy we ascribe the Fe oxidation state in these nodes to 2+. The projected Fe-N distances in these structures (2.3 Å) are close to Fe-N bond lengths (2.2 Å) in high spin Fe^{2+}. [20]

Two distinct phases (δ and ϵ, Figure 4.5) associated with the presence of Fe on the surface can be found in STM investigations of Ag(111) surfaces prepared by sequential dosing of BTB and Fe and subsequent annealing to 390 K and 430 K, respectively.

In phase δ (Figure 4.5A,B,C) one can identify pairs of small round protrusions in between molecular ligands, which can be tentatively assigned to dimers of Fe atoms (separated by 3.3 Å). The head-to-head Fe coordination of the tetrazole moieties is reminiscent of the *exo* ligation reported for surface stabilized dehydrogenated pyrazole moieties. [104] Phase δ

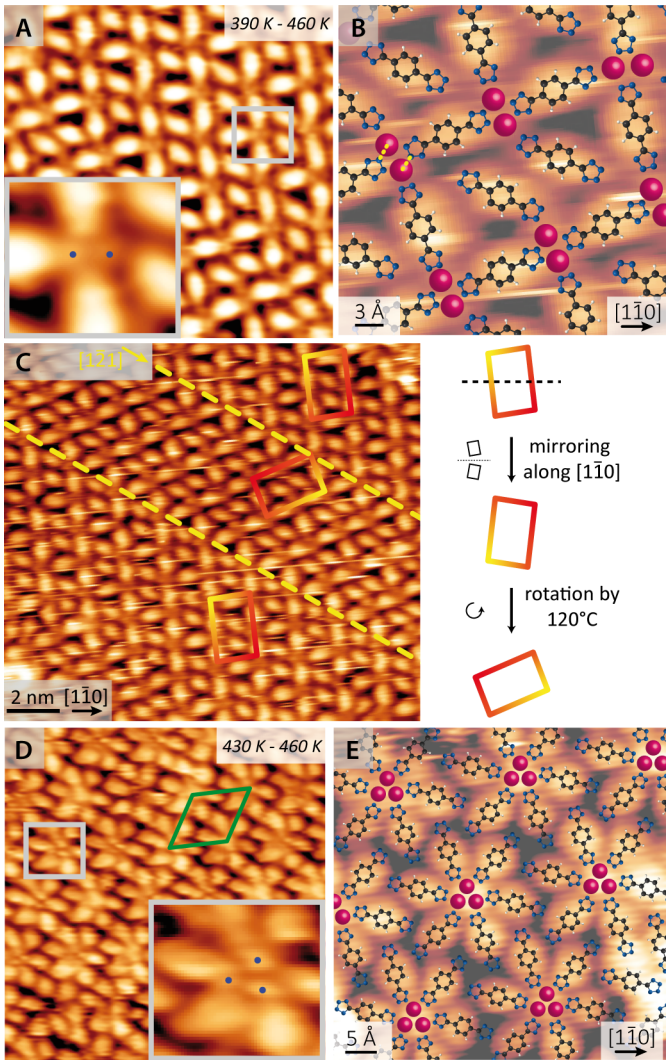

Figure 4.5 Fe coordination of BTB after annealing in the indicated temperature range. (A) STM of phase δ (1.50 V, 60 pA) with rows of alternating chirality. The inset shows the marked part magnified with the proposed position for Fe adatoms. (B) Detail of phase δ (1.50 V, 60 pA). The shortest Fe-N distances are marked in yellow. Magenta spheres represent Fe adatoms. (C) STM highlighting the seamless switching of symmetrically equivalent domains along the $[1\bar{2}1]$, accompanied by a chirality switch, as shown in the schematic on the right. Unit cells are marked by colored boxes (D) STM of phase ϵ (1.50 V, 110 pA), the unit cell is marked in green, the inset shows the proposed position for Fe adatoms. (E) Detail of phase ϵ (1.50 V, 110 pA).

is characterized by a unit cell of five BTB molecules and four Fe atoms: $\begin{pmatrix} 6 & 1 \\ 4 & 10 \end{pmatrix}$. The molecular domains have a zig-zag appearance which arise from chirality and orientational switches of the rows along the $[1\bar{2}1]$ directions of the Ag(111) (Figure 4.5C).

Phase ϵ has a structure resembling flowers (Figure 4.5D,E). Each unit cell consists of six molecules and presumably three Fe atoms imaged as three round protrusions: $\begin{pmatrix} 8 & 1 \\ 7 & 8 \end{pmatrix}$.

Summary

In summary, we have systematically characterised at the atomic scale the self-assembly of a linear bis-tetrazole linker molecule on Ag(111). Unexpectedly, simultaneous deprotonation

and coordination with native Ag adatoms of the tetrazole moieties occur slowly at RT and are further enhanced by annealing to higher temperatures. Owing to the multitude of coordination sites offered by the tetrazole moiety, polymorphism is found in the metal adatom coordination motifs. These range from hosting Ag/Fe trimers to dimers and single adatoms. We thus provide an atomistic scale model of how the silver surface is modified by the adsorption of a planar tetrazole compound and the involvement of metal adatoms in its binding, which is expected to contribute to the mechanistic understanding of corrosion inhibition. Intriguingly, BTB-Fe coordination on the Ag/vacuum interface results in Fe^{2+} species, implying that this ligation might prevent the interfacial charge transfer which often lowers the observed oxidation state and quenches the native magnetic properties of metal-organic complexes. [105] Further experiments are necessary to determine its spin state and whether it exhibits SCO phenomena. At last, we identified a structure (densely packed, phase α) of BTB on Ag(111) which can accommodate metal adatoms coordinating the tetrazoles without changing noticeably the positions of the molecular ligands, presumably mediated by the tetrazole deprotonation.

5 Structural and electronic properties of Ru porphyrins on Ag(111)

This chapter includes content that has been published in

P. Knecht, P. T. P. Ryan, D. A. Duncan, L. Jiang, J. Reichert, P. S. Deimel, F. Haag, J. T. Küchle, F. Allegretti, T.-L. Lee, M. Schwarz, M. Garnica, W. Auwärter, A. P. Seitsonen, J. V. Barth, A. C. Papageorgiou, **Tunable Interface of Ruthenium Porphyrins and Silver**, *J. Phys. Chem. C*, 2021, **125**, 3215-3224. Copyright 2021 American Chemical Society.

Porphyrins are naturally occurring small molecules at the heart of vital biological processes. Their tetrapyrrole ring can host and stabilize on interfaces a large number of the elements of the periodic table, most commonly transition metals, [106–108] but also p-block elements [109] as well as alkali metals, [110] offering unique possibilities of tunable functionalization of chemical, optical and magnetic properties. With the ability of introducing a wide variety of substituents in their periphery, metalloporphyrins are posited as prototypical building blocks of functional interfaces. [111] Furthermore, their tethering to surfaces is frequently raising unexpected properties: For example, the combination of a molecular catalyst and a Au(111) surface was an active catalyst for epoxidation with only benign O_2 as oxidant, an activity that neither the molecule nor the surface process independently. [18] A similar sophisticated hybrid system was envisioned by coupling silver surfaces (which unlike extended gold surfaces can dissociate O_2) with the epoxidation selectivity of a molecular catalyst, [17, 112, 113] and Ru-porphyrins have demonstrated enantioselective epoxidations as homogeneous catalysts. [114, 115] In our earlier studies we found no evidence of the key oxygen intermediates on Ru porphyrins supported on Ag(111). [116] This was attributed to the interfacial coupling and the associated electron donation from the substrate to the porphyrin. [116] However, it was shown recently for Ru metal atoms in single-atom site catalysts that this criterion alone cannot rationalize the catalytic reactivity, whence more detailed structural and electronic configurations need to be considered for the rational design of catalytic interfaces. [117]

Here, for the model system of Ru tetraphenyl porphyrin (Ru-TPP) on Ag(111), we pose the following questions: 1. What is the coupling of the functional Ru center to the Ag(111) surface? 2. Is such coupling affected by the arrangement of the macrocycle? To this end we investigate the effect of (i) molecular coverage and (ii) out-of-plane vs. in-plane arrangement of the macrocycle phenyl substituents, as the conformation of peripheral substituents has been shown to alter the interfacial coupling of porphyrins [118] and their chemical reactivity. [119]

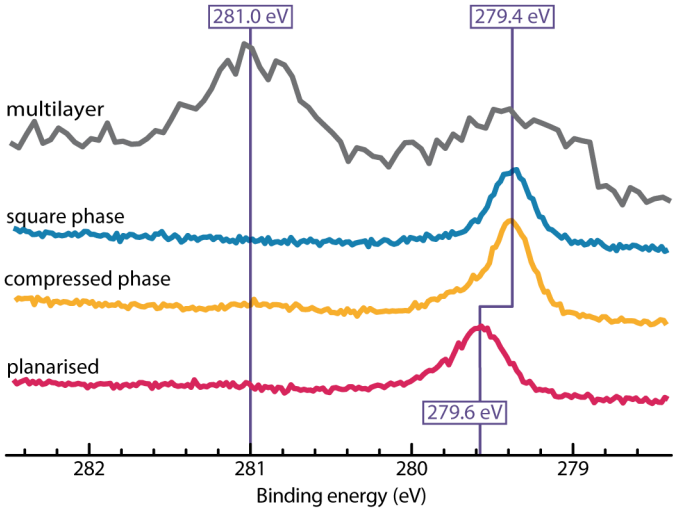

Figure 5.1 XPS data of Ru-TPP on Ag(111), showing the Ru $3d_{5/2}$ region for different coverages of Ru-TPP and planarized derivatives of Ru-TPP.

Our methodological approach encompasses a dual experimental and theoretical investigation: the supramolecular assembly is studied by both low-energy electron diffration (LEED) and scanning tunneling microscopy (STM). The electronic configuration and the related charge transfer is studied using X-ray photoelectron spectroscopy (XPS), STM and density functional theory (DFT). Finally, the detailed adsorption geometry is determined by a combination of normal incidence X-ray standing wave (NIXSW), STM, bond resolving atomic force microscopy (AFM) and DFT. With this comprehensive study, we aim to benchmark the crucial factors needing consideration for not only designing model experimental and theoretical studies, but also in the design of transition metal functionalized molecular single layers on metallic surfaces.

Results and Discussion

Three different phases of Ru porphyrins are considered in the following. The first two correspond to the self-assembly of pristine Ru-TPP with the phenyl legs significantly tilted with respect to the porphyrin macrocycle: a square phase and a denser compressed monolayer phase. The third phase corresponds to planarized derivatives of Ru-TPP, which have their phenyl legs fused to the plane of the macrocycle. To aid the identification of the related data in the figures a color coding is used to mark each separate phase (blue, orange and pink, respectively, see Figure 5.1).

Pristine Ru-TPP on Ag(111): square phase

The Ru-TPP has a strong interaction with the Ag(111) substrate evidenced in the chemical shift that the Ru $3d_{5/2}$ core level exhibits upon adsorption, shown by XP spectra (Figure 5.1): The core-level binding energy is $281.0\,\mathrm{eV}$ for the multilayer and shifts to $279.4\,\mathrm{eV}$ at the interface (Figure 5.1). [116, 120, 121] The binding energy of the multilayer peak agrees

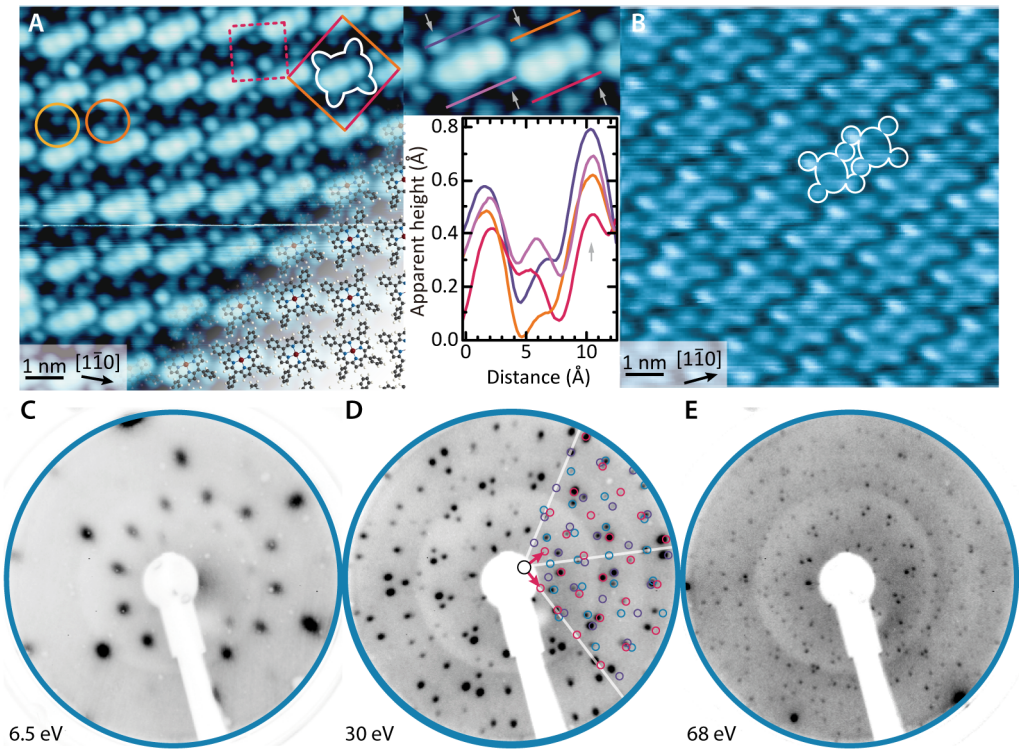

Figure 5.2 STM and LEED data of pristine Ru-TPP on Ag(111). (A) STM image of the square phase (-1.0 V, 50 pA, 5 K). (B) STM topograph of the square phase (2.5 V, 90 pA, 300 K), indicating a dimer-like self-assembly. The white contours outline single molecules, red and orange lines indicate the unit cell. Molecular models are overlaid to visualize the self-assembly. Ru, C, N, and H atoms are depicted in raspberry, gray, blue, and white, respectively. The yellow and orange circles in (A) highlight different molecular separations. The line profiles show differences in the apparent height of the phenyl legs for the two molecules of each unit cell along the same colored lines indicated on the STM image above. (C-E) LEED of square phase Ru-TPP described by a $\begin{pmatrix} 7 & 0 \\ 4 & 8 \end{pmatrix}$ unit cell containing two molecules. Electron energies are given on the bottom left of each image. The pink vectors in (D) show a unit cell, white lines indicate the high symmetry axes of the Ag(111) substrate, obtained from LEED images at higher electron energies (cf. E).

with the expected Ru^{II} oxidation state, [122] whereas the binding energy of the monolayer matches closely the reported value of surface metallic ruthenium. [123] We note that such strong charge transfer is indicative of a chemical bond, and we will elaborate its impact on the structure. For submonolayer coverages the self-assembly appears similar to other tetraphenyl porphyrins on Ag(111), [60] which we observe for Ru-TPP densities of up to $\sim$0.49 molecules nm^{-2} (blue). A detailed analysis of the high resolution LEED of a submonolayer of Ru-TPP (Figure 5.2C-E) reveals a $\begin{pmatrix} 7 & 0 \\ 4 & 8 \end{pmatrix}$ superstructure with respect to the underlying Ag(111) substrate, consistent with the reported LEED of the corresponding free-base TPP single layer on Ag(111). [27] It should be noted that the lengths of the unit cell vectors differ by $\sim 1\,\%$, however for simplicity we refer to it as the square phase. The unit cell vectors are shown in pink, and the diffraction spots corresponding to this unit cell are marked by pink circles. The purple and blue circles mark the diffraction spots of the other symmetrically equivalent domains on the Ag(111) lattice. The intensities of the first order spots are identified more clearly at lower electron energies (5.2C), whereas small mismatches arise due to image distortion inherent to the planar geometry of the microchannel plate in the LEED optics.

Figure 5.2A,B show high resolution STM images of Ru-TPP on Ag(111) in the square phase. Regular islands self-assemble due to intermolecular T-stacking of phenyl substituents (Figure 5.2A) at low molecular coverages. Therein we can identify individual Ru-TPP molecules. Their appearance depends on the applied bias and is comparable for both square phase and the differently packed compressed phase (discussed later in more detail). At $2.5\,\mathrm{V}$ (Figure 5.2B) the physically more protruding phenyl meso-substituents dominate the contrast. At $-1.0\,\mathrm{V}$ (Figure 5.2A) an elongated feature (defining the molecular axis) with three main protrusions can be observed, consisting of the Ru in the center and the two upper ($\acute{\alpha}\nu\omega$) pyrroles (α-pyr) in the saddle-shape conformation, similarly to Co-TPP on the same surface. [55] Four smaller protrusions on the corners arise from the phenyl rings in the porphyrin periphery. The brightness of the Ru center at $-1\,\mathrm{V}$ is associated with an occupied state on the center of the Ru porphyrin on the Ag(111), [124] similar to Co-TPP [25, 125] and Ti-TPP. [126]

For the square phase assembly of Ru-TPP on silver, the axis of the Ru-TPP α-pyr is found along the Ag $\langle 11\bar{2} \rangle$ directions, thus it does not align with either of the unit cell vectors of the substrate (Figure 5.4), resulting in 6 different domains of the self-assembly. [25] In Figure 5.2A, we mark with solid orange and red lines the unit cell proposed from LEED, which accommodates two Ru-TPP molecules. To the best of our knowledge, all previous STM reports of TPP layers on Ag(111) identify a smaller square unit cell containing a single molecule (shown in dotted lines). [27] However, on close inspection we can identify small asymmetries, which depending on the STM imaging could be easily overlooked: the separation of the protrusions corresponding to the phenyl substituents of neighboring molecules are alternating between subtly smaller and larger, as indicated by the orange and yellow circles in Figure 5.2A, respectively. This modulation in density is occasionally giving rise to a more pronounced dimer motif in STM images (5.2B). Additionally, we observe variations in the apparent height of the phenyl meso-substituents of the molecules in each unit cell, as shown in the line profiles in Figure 5.2A. We ascribe this observation to different inclinations of the phenyl rings, caused by the subtly different separations of neighboring molecules. We quantified this subtle difference by an analysis of the position of the central protrusion corresponding to the Ru center. We find the adjacent molecule to be displaced by $(\frac{16}{3}\ \frac{11}{3})$ with respect to the Ag(111) lattice. Compared to an equidistant assembly of all molecules, this corresponds to a displacement of the second molecule of $\sim$0.6 Å.

To further elaborate on the adsorption geometry of the Ru-TPP on Ag(111), a combination of NIXSW measurements and DFT calculations were performed. In the former, the crystalline substrate acts as a diffraction grid of photoelectrons in order to determine the position of atoms with respect to the scattering planes. [43] Using the (111) reflection, the fitting of the photoemission yield in the Ru $3d_{5/2}$ region (Figure 5.3A) results in a coherent fraction of 0.88 ± 0.05, indicative of a very uniform adsorption height for all Ru atoms. From the coherent position we determine an adsorption height of 2.59 ± 0.05 Å. This indicates a strong interaction between the Ru atoms and the Ag(111) surface, supported by the shift of the Ru $3d_{5/2}$ binding energy observed in XPS (Figure 5.1) and in good agreement with DFT (Table 5.1) (cf. structural analysis in Comparison section).

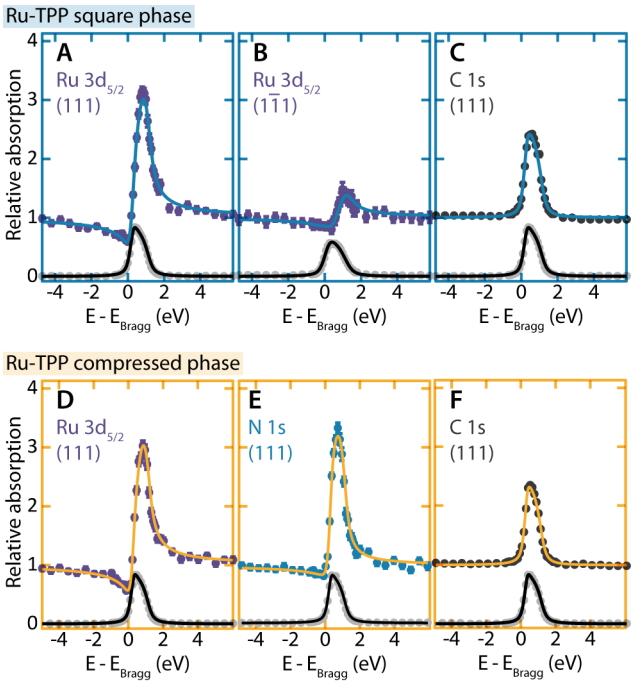

Figure 5.3 Fitted NIXSW photoelectron profiles of pristine Ru-TPP on Ag(111). The reflection of the silver substrate is given by the light gray dots, the black line shows the respective fit: (A-C) square phase and (D-F) compressed phase. The planes fulfilling the normal-incidence Bragg conditions and the investigated elements and core levels are indicated. The coherent positions and fractions deduced by the fittings can be found in Table 5.1.

Combining the results from the (111) and the $(1\bar{1}1)$ reflections (Figure 5.3A,B) allows the lateral adsorption site of the Ru atoms, on the Ag(111) substrate, to be determined. [43, 127] The resulting coherent fraction of 0.58 ± 0.04 from fitting the $(1\bar{1}1)$ data (Figure 5.3B) allows us to exclude adsorption on bridge sites as well as adsorption in single adsorption sites sharing the point group symmetry of the substrate (fcc, hcp or atop sites). The former case would result in a coherent fraction of 0.33 due to the equivalent adsorption sites, while the coherent fraction should be close to 1 in the latter cases. [43] Excellent agreement with the experimental data (Table 5.1) is obtained for an equal occupation of fcc and hcp hollow sites, where the expected coherent fraction and position in the Ru 3d$_{5/2}$ $(1\bar{1}1)$ data, assuming an adsorption height of 2.59 Å, would be 0.50 and 0.87, respectively. This finding allows us to rationalize the results from the STM study: the two molecules of the unit cell can be placed onto the Ag(111) in such a way, that one Ru atom occupies an fcc hollow site and the other Ru atom occupies an hcp hollow site, two sites that differ, laterally and in fractional coordinates, by **1:**$(n \pm \frac{2}{3}\, m \pm \frac{1}{3})$, **2:**$(n \pm \frac{1}{3}\, m \pm \frac{2}{3})$ or **3:**$(n \pm \frac{1}{3}\, m \mp \frac{1}{3})$, where n and m are non-zero integers. Thus the displacement revealed by the STM images, $(\frac{16}{3}\ \frac{11}{3})$, would correspond to offset **3** with $n = 5$ and $m = 4$. This is confirmed by DFT (Table 5.1, Figure 5.4), which shows the Ru centers close to hcp (yellow) and fcc (red) hollow sites (offset by ~ 0.3 Å from the respective hollow site).

Finally, the relaxed DFT structure reproduces the saddle-shape conformation of the pristine Ru-TPP molecules, with a stronger bending found for the α-pyr. The calculations show a more pronounced tilting of the phenyl rings ($\sim$33-44°) compared to the macrocycle pyrrole rings ($\sim$8-28°) with respect to the Ag(111) substrate, in agreement with near-edge X-ray

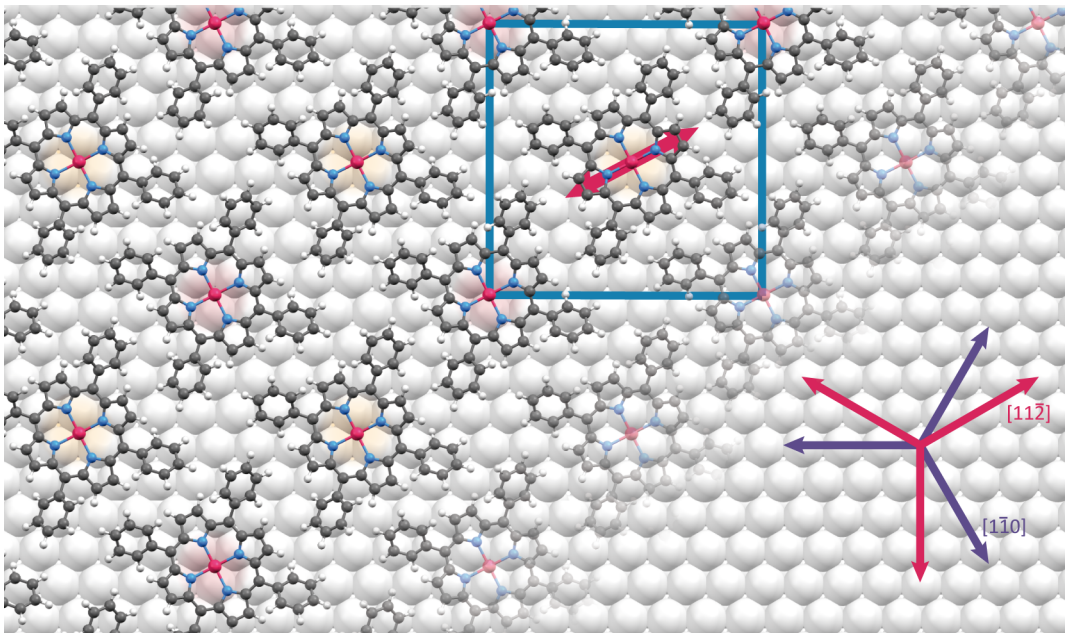

Figure 5.4 Top view of the Ru-TPP square phase on Ag(111) derived from the DFT energy optimization. The two different adsorption sites of the Ru centers are marked in yellow and pink, respectively, the unit cell of the Ru-TPP is marked in blue. The family of the high symmetry $\langle 1\bar{1}0\rangle$ directions is marked in violet, the family of the $\langle 11\bar{2}\rangle$ directions in pink, the α-pyr axis of the Ru-TPP is marked in pink according to the substrate alignment. Ru, Ag, C, N, and H atoms are depicted in raspberry, silver, gray, blue, and white, respectively.

absorption fine structure. [121] The adsorption height of the phenyl rings due to the different tilt angles differs by up to $\sim$0.4 Å, which can be related to the observed differences in the apparent height in STM (Figure 5.2A).

The saddle-shape and the tilt of the phenyl substituents are reflected by the low coherent fraction of 0.22 ± 0.03 of the C 1s NIXSW data (Figure 5.3C), in agreement with the value extracted from DFT ($f_{111,DFT} = 0.18$, assuming a Debye Waller factor of 0.9 [45]). The coherent position of 0.28 ± 0.03 (3.02 ± 0.07 Å) is slightly smaller than the coherent position of 0.36 (3.20 Å) extracted from the DFT simulation.

Pristine Ru-TPP on Ag(111): compressed phase

When the Ru-TPP coverage is (close to) a saturated monolayer (either by increasing the surface coverage or by annealing a multilayer film at 550 K), we observe structural changes in the LEED pattern (Figure 5.5B-E). The superstructure, referred to as compressed phase, can be described by a $\begin{pmatrix} 4 & 5 \\ 3 & -13/6 \end{pmatrix}$ unit cell. The pink, violet and blue circles show the spots from the three rotationally equivalent domains, the dashed circles represent their respective mirror domains. While this superstructure shows a good agreement with the measured spots in the LEED image, it cannot cover all visible spots. By adding the patterns of unit cells, which differ from the previously stated by less than 4 % in dimension and less than 3° in orientation, the accordance between LEED and measured lattice can be further increased (Figure 5.5D). In the following only the $\begin{pmatrix} 4 & 5 \\ 3 & -13/6 \end{pmatrix}$ unit cell will be considered, as the variations in compres-

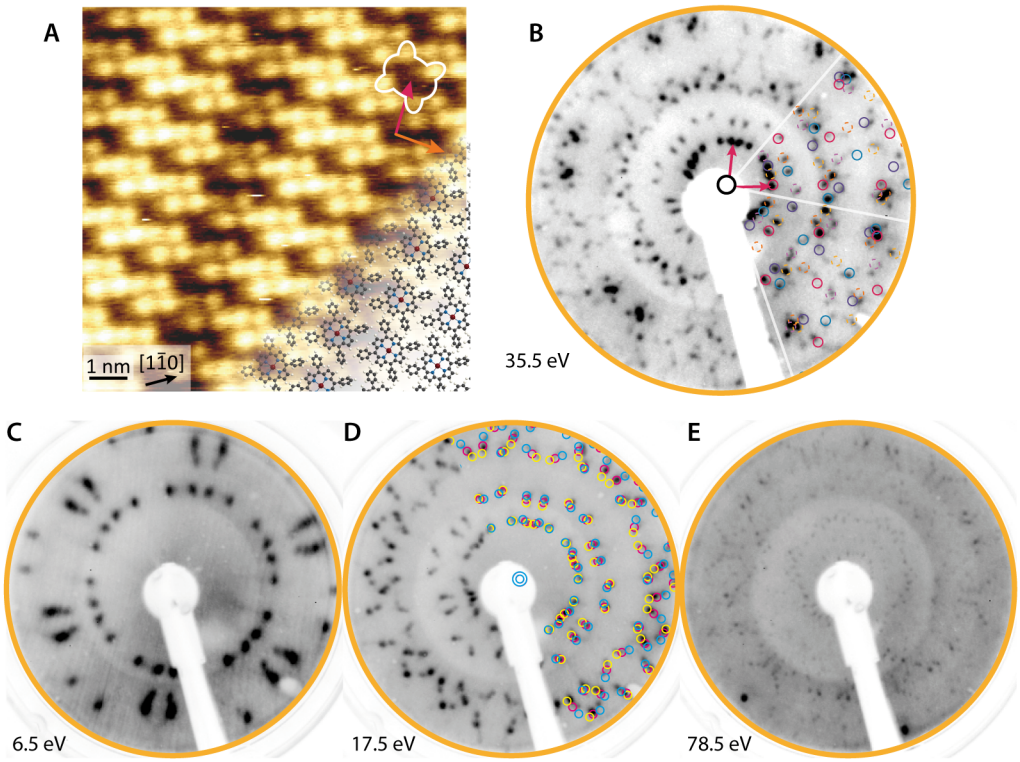

Figure 5.5 STM and LEED data of pristine Ru-TPP on Ag(111). (A) STM topograph of the compressed phase (1.9 V, 30 pA, 300 K). The white contour outlines a single molecule, red and orange arrows indicate unit cell vectors. Molecular models are overlaid to visualize the self-assembly. Ru, C, N, and H atoms are depicted in raspberry, gray, blue, and white, respectively. (B-E) LEED pattern of compressed phase Ru-TPP. Electron energies are given on the bottom left of each image. The overlaid model in (B) is described by a $\begin{pmatrix} 4 & 5 \\ 3 & -13/6 \end{pmatrix}$ unit cell containing one molecule. The pink vectors show a unit cell, white lines indicate the high symmetry axes of the Ag(111) substrate, obtained from LEED images at higher electron energies (cf. E). In (D) there are different superstructures overlaid in different colors. Pink: $\begin{pmatrix} 4.00 & 5.00 \\ 3.00 & -2.17 \end{pmatrix}$, yellow: $\begin{pmatrix} 5.17 & 4.04 \\ -2.37 & 2.88 \end{pmatrix}$, blue: $\begin{pmatrix} 3.89 & -0.93 \\ 3.21 & 5.16 \end{pmatrix}$.

Table 5.1 NIXSW results and deduced structural parameters from NIXSW and DFT: Coherent fractions f_{hkl} and coherent positions P_{hkl} satisfying Bragg conditions from the (hkl) plane of the Ru and C signals of square phase Ru-TPP, compressed phase Ru-TPP and planarized Ru-TPP derivatives on Ag(111). Adsorption heights are extracted from the (111) reflections; the adsorptions site for Ru centers from the triangulation data. Measurements were performed at 200 K if not specified differently.

				Adsorption height (Å)		
	hkl	**f_{hkl}**	**P_{hkl}**	NIXSW	DFT	Adsorption site
Pristine Ru-TPP: Square phase						
Ru $3d_{5/2}$	(111)	$0.88(5)$	$0.10(2)$	$2.59(5)$	2.68	hcp & fcc hollow
Ru $3d_{5/2}$	$(1\bar{1}1)$	$0.58(4)$	$0.88(2)$			
C 1s	(111)	$0.22(3)$	$0.28(3)$	$3.02(7)$	3.20	
Pristine Ru-TPP: Compressed phase						
Ru $3d_{5/2}$	(111)	$0.89(5)$	$0.10(2)$	$2.59(5)$		
C 1s	(111)	$0.16(2)$	$0.29(2)$	$3.04(5)$		
N 1s	(111)	$0.81(5)$	$0.18(2)$	$2.78(5)$		
Planarized Ru-TPP						
Ru $3d_{5/2}$	(111)	$0.92(3)$	$0.04(1)$	$2.45(2)$	2.48	hcp & fcc hollow
Ru $3d_{5/2}$	$(1\bar{1}1)$	$0.51(2)$	$0.90(1)$			
C 1s	(111)	$0.75(3)$	$0.27(1)$	$3.00(2)$	3.00	
Planarized Ru-TPP (300 K)						
Ru $3d_{5/2}$	(111)	$0.82(5)$	$0.02(2)$	$2.41(5)$		
C 1s	(111)	$0.49(1)$	$0.28(1)$	$3.02(2)$		
N 1s	(111)	$0.83(5)$	$0.11(2)$	$2.62(5)$		

sion and orientation between this family of unit cells are minor, compared to the difference between the square phase and any of the compressed phases.

The molecular density of a layer in this configuration (0.58 molecules nm^{-2}) is $\sim$18 % higher compared to the packing of the square phase (0.49 molecules nm^{-2}). This densely packed layer is also observed in STM (see Figure 5.5A). The α-pyr axis is rotated by $\sim$15° with respect to the overlayer unit cell vector, however the orientation of both the α-pyr and these unit cell vectors no longer coincide with any of the Ag$\langle 11\bar{2}\rangle$ and $\langle 1\bar{1}0\rangle$ families of directions. The wave-like modulation of the brightness is identified as a moiré pattern. Along the commensurate unit cell vector (Figure 5.5A, red) the molecules have similar apparent heights, while along the other unit cell direction (Figure 5.5A, orange) we see a repeating pattern every three molecules, which can be related to the higher-order-coincidence.

A transition to a more densely packed phase has not been observed for Zn-TPP, [26] Co-TPP [128] or the free base 2H-TPP [27] on Ag(111). As the intermolecular interaction is very similar for these molecules, we propose a stronger interaction between molecule and substrate, in particular of the Ru center and the Ag(111) as driving force. This interaction has to be strong enough to compensate for the induced strain due to the compression of the molecules into the smaller surface footprint and from adsorbing in different adsorption sites than the favored hollow sites.

NIXSW data shows for the Ru atoms in (111) reflection (Figure 5.3D, Table 5.1) the same coherent fraction and position as in the square phase. Therefore, even for the compressed assembly of Ru-TPP, all Ru centers have, independent of the lateral registry on the Ag(111) surface, the same adsorption height of 2.59 Å $\pm$ 0.05 Å. Compared to the square phase,

in the compressed phase, the higher molecular density, the higher-order coincidence, and the more uniform spatial distribution of Ru-TPP molecules (Figure 5.5A) preclude a well-defined adsorption site for the Ru centers. Therefore this was not investigated with NIXSW triangulation. The C 1s NIXSW (Figure 5.3F, Table 5.1) has a low coherent fraction similar to the square phase, indicating a similar variation in the adsorption height distribution of the organic ligand.

N 1s spectra (Figure 5.3E) reveal a lower coherent fraction compared to the Ru $3d_{5/2}$, agreeing with the expectation of a less uniform adsorption height for the N atoms in the saddle-shape configuration. [129] The coherent position indicates an average adsorption height as $2.78\,\text{Å} \pm 0.05\,\text{Å}$. If we consider that the N atoms define the plane of the macrocycle, this sits an average of $0.19\,\text{Å}$ higher than the Ru atom.

Planarized Ru-TPP derivatives on Ag(111)

We further investigate the interaction of metalloporphyrins with the Ag(111) by studying the structural and conformational changes to the molecule after undergoing oft-observed cyclodehydrogenation reactions between the macrocycle periphery and the phenyl substituents.[26, 60, 124, 130–132] For Ru-TPP on Ag(111), this is achieved by thermal annealing and such transformations result in a nearly flat molecule. Thereby, a variety of planar surface products (Figure 5.6A-D) form depending on the side of the ring-closing. [60] In STM images (Figure 5.6E,I,J) we identify clearly the given product by its outline, whereas the contrast of the Ru center is enhanced at a sample bias of approximately $-1\,\text{V}$. The distribution of the four products and their respective surface enantiomers is almost statistically random, unlike the recent example of a related metalloporphyrin, where higher stereoselectivity in the ring closing resulted in a highly ordered homochiral assembly. [133] non-contact AFM (nc-AFM) can image the newly formed bonds as well as the overall planar nature of the molecule based on the appearance of the C atoms. [131] At low coverages, we find that, as for the pristine Ru-TPP in the square lattice, a N-Ru-N axis of the molecules is always aligned with the Ag$\langle 11\bar{2} \rangle$ family of directions, but the molecules do not generally assemble in preferential patterns (Figure 5.6I).

A saturated layer of these different planarized Ru-TPP derivatives ($\sim 0.42\,\text{molecules}\,\text{nm}^{-2}$) also gives rise to a diffraction pattern (Figure 5.6K), albeit less defined, indicating a loss of the highly ordered self-assembled structures observed for the pristine Ru-TPP. The LEED pattern exhibits ring-like shapes which are centered around the $(0, 0)$. Within the ring, spots can still be discriminated. These spots indicate a square unit cell, with nearly identical unit vectors lengths, and one of the vectors co-linear with the one of the surface unit cell vectors (pink arrows, Figure 5.6K). The FFT of the STM data (Figure 5.6J inset) indicates a real space unit vector length of $\sim 15\,\text{Å}$ (blue arrows, Figure 5.6J). This would therefore suggest a surface unit mesh of approximately $\begin{pmatrix} 5.2 & 0 \\ 3 & 6 \end{pmatrix}$, however the diffuse nature of the spots makes a definitive assignment impossible. It is noted that at these higher coverages, only $\sim 70\,\%$ of the molecules are adsorbed with a N-Ru-N direction aligned to the Ag$\langle 11\bar{2} \rangle$. We attribute this

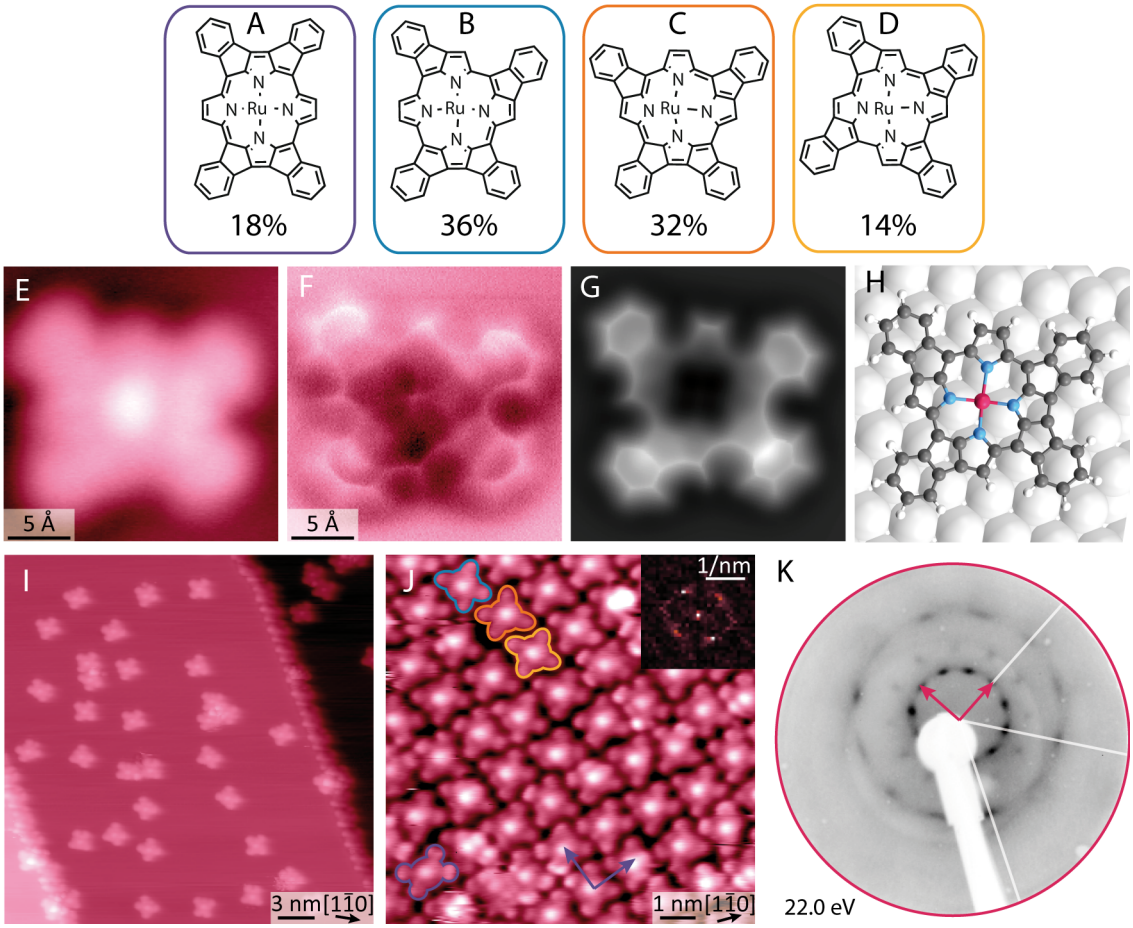

Figure 5.6 (A-D) Different cyclodehydrogenation products of the Ru-TPP on Ag(111) with their relative abundancies. [60] (E-H): The most common product (B). (E) STM micrograph with a CO-modified tip (-50 mV, 50 pA, 5 K). (F) Corresponding nc-AFM frequency shift image of the same molecule (tip height z = -20 pm with respect to the STM set point above Ag(111), oscillation amplitude 80 pm). (G) AFM simulation based on the DFT model. (H) Respective DFT model. Ru, Ag, C, N, and H atoms are depicted in raspberry, silver, gray, blue, and white, respectively. (I) STM topograph (-0.5 V, 50 pA, 5 K) of planarized Ru-TPP derivatives. (J) STM image (-1.2 V, 60 pA, 300 K) of a single layer of planarized Ru-TPP derivatives on Ag(111), distinguishing the four different planarized Ru-TPP derivatives, outlined in the same colors as in (A-D). Marked in purple are the unit cell vectors identified by the LEED analysis. The inset includes a fast Fourier transform (FFT) of the image. (K) LEED pattern showing blurry first and second order spots. The ring-shaped pattern indicates less order compared to the assembly of the pristine Ru-TPP. The pink vectors indicate unit cell vectors. White lines show high symmetry axes of the Ag(111) substrate.

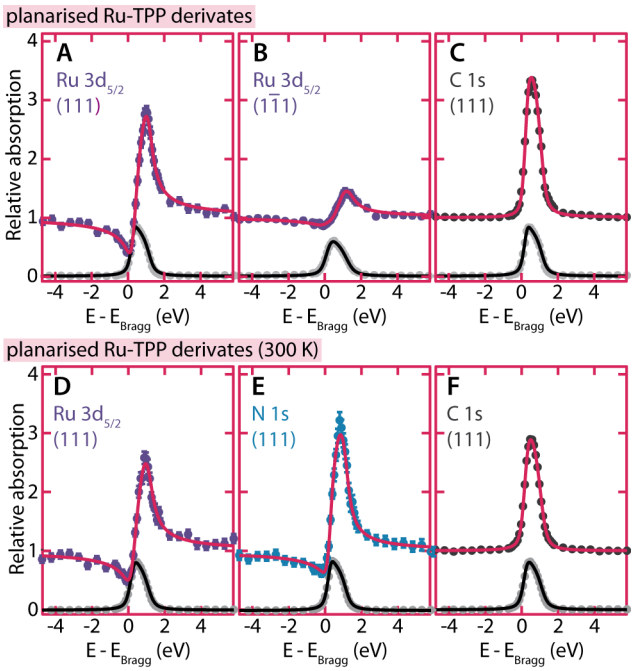

Figure 5.7 Fitted NIXSW photoelectron profiles of the planarized Ru-TPP derivatives on Ag(111). The reflection of the silver substrate is given by the light gray dots, the black line shows the respective fit. The planes fulfilling the normal-incidence Bragg conditions, investigated elements and core levels are given on each graph. The respective coherent positions and fractions are listed in Table 5.1.

effect to the dense packing of asymmetric monomers, which retain a well-defined tethering site for the Ru center, as we will demonstrate below.

The structure of the planarized Ru-TPP derivatives in this high coverage layer was also characterized by NIXSW (Figure 5.7, Table 5.1), which showed marked differences relative to pristine Ru-TPP. The coherent fraction for the C 1s increased sharply to 0.75 ± 0.03 with an average adsorption height of $2.98\,\text{Å} \pm 0.02\,\text{Å}$ comparable to studies on the likewise flat CuPc on Ag(111). [134] The measured coherent fraction can be reproduced by assuming a standard deviation of $< 0.3\,\text{Å}$ in the average adsorption height, showing that the molecule is not perfectly flat on the Ag(111) surface. The coherent fraction and position determined for the C 1s suggest that all carbon atoms are sitting higher that the Ru center, which will be discussed in more detail below. STM and AFM images (Figure 5.6E,F,I,J) do not show a two-fold symmetry of the macrocycle. In addition, the coherent fraction of the N 1s of NIXSW measurements at $300\,\text{K}$ (Figure 5.7E, Table 5.1) is similar to the coherent fraction of the Ru $3d_{5/2}$ signal, indicating a uniform adsorption height (compare with N 1s data for compressed phase in Table 5.1). [129] Both observations are not compatible with a saddle-shape deformation. Therefore we propose a bowl-shape for the planarized Ru-TPP derivatives, which is further corroborated by our DFT calculations (Figure 5.8B) and is similar to FePc and CoPc on Ag(111). [135, 136] This bowl-shaped DFT structure gives good agreement with the nc-AFM data (see simulation in Figure 5.6G).

However, DFT suggests a rather weak deviation from a planar conformation with a tilt angle of $\sim 4°$ on the edge of the molecule with regard to the underlying Ag(111) substrate. To account for the measured coherent fraction of the C 1s peak, a curvature that results in an angle

of $\sim$13° between the molecular plane at the outermost C atoms and the Ag(111) substrate would be required (assuming a Debye Waller factor of 0.9 to account for vibrations [45]). A drop in coherent fraction can be a temperature effect, as reported for analogous systems. [134] Additionally, the NIXSW measurements average over all different planarized products, while the DFT calculations considered only the most commonly observed planarized Ru-TPP derivative (Figure 5.6B).

NIXSW of the Ru 3d$_{5/2}$ peak in the (111) reflection shows that the Ru centers are even closer (by 0.14 Å) to the surface than in the pristine Ru-TPP, with an adsorption height of 2.45 Å $\pm$ 0.02 Å. The binding energy of the Ru 3d$_{5/2}$ peak however increases by approximately 0.2 eV (Figure 5.1), showing that the binding energy (and, correspondingly, the likely effective charge on the Ru center) is not directly correlated with the adsorption height. By combining the findings from the (111) reflection with the results from the $(1\bar{1}1)$ reflection, the adsorption site of the Ru center is, like in the square phase above, again determined to be a mixture of hcp and fcc hollow sites (Table 5.1). This is also in agreement with the DFT calculations, which identified a lateral adsorption site close to an hcp hollow site ($\sim$0.3 Å lateral displacement) and a predicted adsorption height of 2.48 Å.

Comparison of the different Ru porphyrin phases on Ag(111)

We have observed two different highly ordered self-assemblies for the pristine Ru-TPP depending on the molecular coverage on the Ag(111) surface. In both phases T-type interactions of the phenyl rings result in a nearly square arrangement of the Ru-TPP building blocks (Figure 5.2A,5.5A) and a saddle-shape conformation of the porphyrin ligands (Figure 5.8A). However, the two phases differ significantly in their molecular density: while the square phase is very comparable to other TPPs, [17, 25–27] the compressed phase is significantly more densely packed, which, to the authors' knowledge, has not been observed for any TPP on Ag(111).

The family of planarized Ru-TPP derivatives shows a less well-defined arrangement of lower density in comparison to the pristine Ru-TPP phases. This is related to both having a distribution of four different co-existing building blocks, forming an intermixed layer, as well as to the removal of attractive T-type interactions.

Despite the differences in the self-assembly, the adsorption height of the Ru centers of $\sim$2.59 Å was determined to be identical for the two phases of pristine Ru-TPP and similar to the metal center of the more planar FePc. [136] In comparison with the adsorption heights of other transition metals hosted in TPP molecules inferred by NIXSW ($\sim$2.9 Å for Co-TPP and Zn-TPP) [137] or calculated by DFT (2.66 Å for Ti-TPP), [126] the Ru center is placed relatively close to the Ag(111). After the conversion to the planarized derivatives, the Ru is found to be closer to the surface at a distance of $\sim$2.45 Å. The resulting smallest Ru-Ag bond lengths both for planarized Ru-TPP derivatives (experiment: $\sim$2.97 Å / theory: 2.88 Å) and square phase pristine Ru-TPP (experiment: $\sim$3.08 Å / theory: 2.92 Å) are typical of a covalent bond (2.91 $\pm$ 0.09 Å). [138]

This covalent character of the chemisorption is supported by DFT deduced electron density

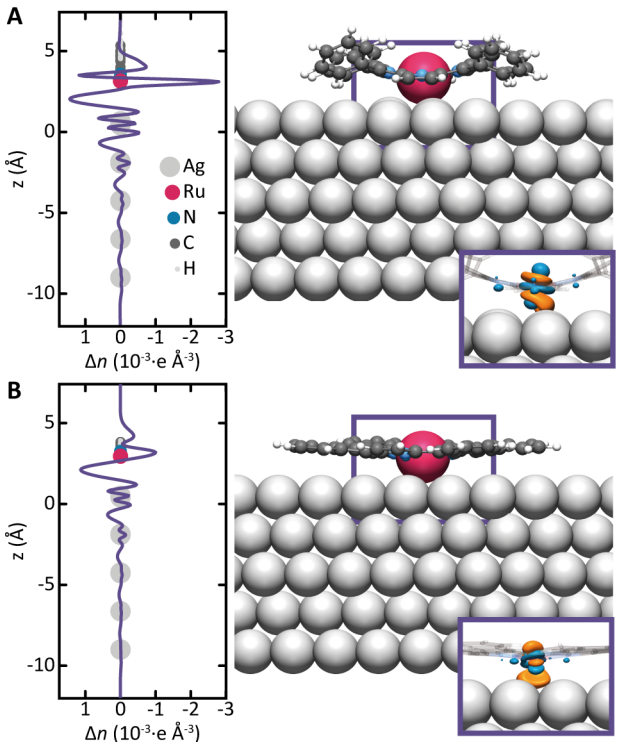

Figure 5.8 DFT modelling of Ru porphyrins on Ag(111). (A) Pristine Ru-TPP in the square phase in the saddle-shape conformation. (B) Most abundant planarized Ru-TPP derivative (Figure 5.6B) in a bowl conformation. Ru, Ag, C, N, and H atoms are depicted in raspberry, silver, gray, blue, and white, respectively. Electron density differences, Δn, upon adsorption of the Ru porphyrins are plotted against the distance from the Ag surface (graphs on the left) and shown in three dimensional (3D) maps (insets on the right) with isosurfaces at $\pm 0.04\, e$ Å^{-3} (orange and blue represent gain and loss of electron density, respectively).

difference, Δn, upon adsorption of the Ru-TPP and planarized Ru-TPP derivatives: we observe accumulation of charge on both sides of the Ru atoms [139] involving the Ru d orbitals (insets in Figure 5.8). In both cases, the one-dimensional plots show similar features, namely a depletion of electron density at the height of the Ru center and a gain of electron density in the interface between Ru atom and Ag substrate. However, this is accomplished differently for the two molecules. While in the case of Ru-TPP a depletion of the d_{z^2} orbital and a filling of d_{xz} and d_{yz} orbitals of the Ru center is observed, the planarized Ru-TPP gains electron density in the d_{z^2}, but loses electron density in the d_{xz} orbital. This highlights different electronic properties for the two different molecules, of potential relevance to their chemical reactivity.

Interestingly, we do not observe a measurable difference in the average adsorption height of the C atoms, which leads us to the assumption that only the center of the macrocycle is closer to the surface, while the molecule itself remains bent, with the outer atoms lifted away from the surface, similar to DFT calculations of the flat CoPc on Ag(111) [135] or NIXSW data on the fluorinated F_{16}CoPc. [140] Moreover, unlike Co-porphine on Cu(111), [129] a metalloporphyrin without out-of-plane substituents, for the planarized Ru-TPP derivatives on Ag(111) we have no detectable evidence of a saddle-shape conformation of the macrocycle in either the N 1s NIXSW nor in the AFM data.

Furthermore, NIXSW triangulation shows that the Ru center of the pristine Ru-TPP adsorbs on fcc and hcp hollow sites for submonolayer coverages, similar to Co-TPP. [25] This adsorption mode is also found for the planarized Ru-TPP derivatives. In both cases we deduce from NIXSW an equal distribution between hcp and fcc hollow sites, indicating that the adsorption energy is similar for both sites. Based on STM and LEED data, within the compressed phase, an adsorption of Ru solely on hollow sites is unlikely. The salient findings on the adsorption behavior point towards a strong interaction of the Ru center with the underlying Ag(111) substrate: The two molecule unit cell in the square phase accommodating the Ru centers into favored hollow sites; the compressed phase allowing even more molecules to adsorb in a single monolayer despite the additional strain and lack of registry to the favored sites; the small adsorption height of the Ru centers above the Ag(111) surface compared to other metal centers of porphyrin molecules, and the binding energy shift visible in the Ru $3d_{5/2}$ core level of the monolayer.

Conclusions

We have demonstrated that the Ru centers of Ag(111)-adsorbed Ru porphyrins are chemisorbed to the Ag substrate, irrespective of (i) molecular conformation (molecular distortion of Ru-TPP in supramolecular assembly) and (ii) planar vs. out-of-plane substituents. Our detailed analysis of the Ru-TPP/Ag(111) structure shows that the bonding to the Ag surface as well as the complete arrangement of the porphyrin ligand and the substrate are responsible for the accessible Ru coordination sphere and the chemical reactivity of the monolayer. [116, 141, 142] The first Ru coordination sphere includes the three surface Ag atoms lying 2.59 Å / 2.45 Å below the Ru center and the porphyrin ligand that lies, on average, ~ 0.5 Å above the Ru center, for both pristine Ru-TPP in a saddle-shape configuration (Figure 5.8A) and the

annealed Ru-TPP in a planarized bowl-shape configuration (Figure 5.8B). The chemisorption of the Ru porphyrins is mediated by a charge transfer with covalent character, predominantly between the Ru atom and the Ag surface.

A coverage-dependent phase transition of the pristine Ru-TPP into a compressed phase was shown by LEED and STM to accommodate almost $20\,\%$ more molecules compared to the square phase assembly. This expands our understanding of the TPP molecular flexibility on solid surfaces and offers possibilities of tuning the molecular densities of these layers without high local coverage gradients.

We demonstrate that, for Ru-porphyrins, Ru has a strong preference for the hollow site irrespective of the substituent conformation: This preference is preserved for the non-compressed phases of the pristine Ru-TPP as well as for the layer of the planarized Ru derivatives. We find that this preference results in a slightly asymmetric checkerboard arrangement of the pristine Ru-TPP molecules at low coverage, which cannot be satisfied for the molecule's high coverage, compressed phase.

From NIXSW we infer as well that the adsorption height of the Ru center for the pristine Ru-TPP is identical for the two different assemblies: pulled out of the porphyrin macrocycle towards the Ag(111) substrate at a distance of $2.59\,$Å. This value is corroborated by DFT for the square phase. For the planarized Ru-TPP derivatives, the Ru is $0.14\,$Å closer to the surface demonstrating that the tilted phenyl legs provide a very small lift-off of the functional porphyrin core from the surface, which was not observed between Cu-porphine [126] and Cu-TPP [143] on Cu(111). However changes both in the electron density difference upon adsorption around the Ru atom and in the ligand geometry are observed between the two different Ru porphyrins. Such changes are anticipated to influence the resulting functional properties.

The detailed insight to the nature of the bonding of Ru porphyrins on a silver surface provided here is expected to be of relevance to the precise functionalization of surfaces with metalloporphyrins and to enable the application of the "form follows function" principle to molecular architectonics on interfaces.

6 Conformational control of chemical reactivity for surface-confined Ru-porphyrins

This Chapter includes content that has been published in:

P. Knecht, J. Reichert, P. S. Deimel, P. Feulner, F. Haag, F. Allegretti, M. Garnica, M. Schwarz, W. Auwärter, P. T. P. Ryan, T.-L. Lee, D. A. Duncan, A. P. Seitsonen, J. V. Barth, A. C. Papageorgiou, **Conformational control of chemical reactivity for surface-confined Ru-porphyrins**, *Angew. Chem., Int. Ed.*, doi.org/10.1002/anie.202104075.

For the creation of novel materials and devices, inspiration is frequently sought in nature. Porphyrins and other natural tetrapyrrole compounds can incorporate a large fraction of the chemical elements in the periodic table. Their functionality is tuned by choice of the complexed species, possible axial ligands and substituents in the macrocycle periphery. For example, in biology, the binding of small molecules to metal centers of porphyrins determines many vital functions. Over the past decades we have witnessed an intense interest in utilizing porphyrins on surfaces as functional building blocks with a myriad of applications: ranging from atomic switches to single-molecule magnets and catalysts. [111] The surface chemistry of cyclic tetrapyrrole compounds is therefore a topic of extended research [108] and includes the on-surface metallation [106, 107] as well as s-block [110] and p-block [109] element functionalization. In this context, the effect of the macrocycle substituents has been studied systematically. [144] Moreover, the reactivity of individual metal atoms on surfaces is a topical issue in single-atom catalysis, [145–148] whereby arrays of metalloporphyrin layers under vacuum conditions present a versatile playground due to the coordinatively unsaturated metal centers provided by the generally favored adsorption geometries with the macrocycle residing parallel to the substrate lattice.

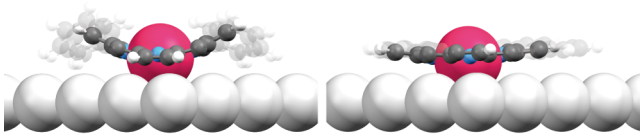

Figure 6.1 Models of a Ru tetraphenyl porphyrin (Ru-TPP) (left) and a planarized Ru-TPP derivative (right) on Ag(111). The substituents are faded to highlight the difference in the conformation of the porphyrin macrocycles. (see Chapter5; Ru, C, N, H, and Ag are shown in red, black, blue, white, and silver, respectively.

Complexes of inorganic gaseous molecules with metalloporphyrins are important intermediate species in catalysis. CO, [149–151] NO, [149, 152] NH_3, [136] and H_2O [136] have been shown to bind on metal supported metalloporphyrins and phthalocyanines axially to the metal center. In particular, CO also exhibited an unusual *cis*-μ-dicarbonyl ligation on top of Fe (and Co) tetraphenyl porphyrins on Ag(111) (and Cu(111)). [153] Ligation to the metal center gives rise to the so-called structural *trans*-effect, whereupon the metal atom is electronically and physically decoupled from the substrate. [136, 152, 154, 155] Generally, a significant alteration of the porphyrin's reactivity and electronic structure occurs due to the interaction with the metal center. [116] Turning our attention on the topic of *'switch on'* functionalities of organic layers on metal surfaces, we can find a common approach of 'decoupling' the molecule from the surface by e.g. a rigid tethering, [156] bulky substituents, [92, 157] or a platform [158] which enables a 'lift-off' of the functional moiety. In a biological environment, the macrocycle conformation can influence its functionality. [141] Here, we will examine this aspect: can we influence the function present in the free molecule (here CO binding) by the conformation of the porphyrin macrocycle (Figure 6.1) hosting the metal center on the surface?

For Ru-TPP, CO is determined to have an unusually high ligation energy ($1.9\,\mathrm{eV}$), [32] hence can be considered as a prototypical out-of-plane ligand with the stability of a covalent attachment. We study the effect of the porphyrin surface environment on this ligation for Ru-TPP and its planarized derivatives (Ru-TPP_{pl}) on Ag(111). We use scanning tunneling microscopy (STM) to find a *cis*-μ-dicarbonyl ligation [153] stable at low temperatures ($5\,\mathrm{K}$) and an axial ligation at higher temperatures ($200\,\mathrm{K}$), which is also examined with temperature programmed desorption (TPD). In stark contrast, there is no evidence of CO binding to the planarized Ru-TPP derivatives on Ag(111) under either conditions. We correlate the axial binding to conformational and electronic changes, rationalized by density functional theory (DFT), X-ray photoelectron spectroscopy (XPS), ultraviolet photoelectron spectroscopy (UPS) and normal incidence X-ray standing waves (NIXSW).

Results and Discussion

Imaging in real space

When deposited on Ag(111) at room temperature (RT) in submonolayer coverages, Ru-TPP (Figure 3.6) molecules self-assemble in a square phase [60] described by the epitaxial matrix $\begin{pmatrix} 7 & 0 \\ 4 & 8 \end{pmatrix}$ (see Chapter 5, [159]). Figure 6.2A-C shows the assembly on such a surface cooled down to $5\,\mathrm{K}$. For negative bias voltages ($\sim -1\,\mathrm{V}$), the single molecule appearance of the pristine Ru-TPP (outlined in orange) is characterized by three bright protrusions along the macrocycle and four less bright in the periphery marking the phenyl substituents. The central bright protrusion corresponds to a filled electronic state of the Ru center (cf. UPS below), [121, 124] whereas the side ones can be assigned to the protruding $\acute{\alpha}\nu\omega$-pyrroles (α-pyr) of the macrocycle. [153] The downward bending $\kappa\acute{\alpha}\tau\omega$-pyrroles ($\kappa$-pyr) are not discernible. In the STM images of the layer we can also identify molecules with additional protrusions, located on the sides of the Ru center and perpendicular to the axis of the α-pyr (examples

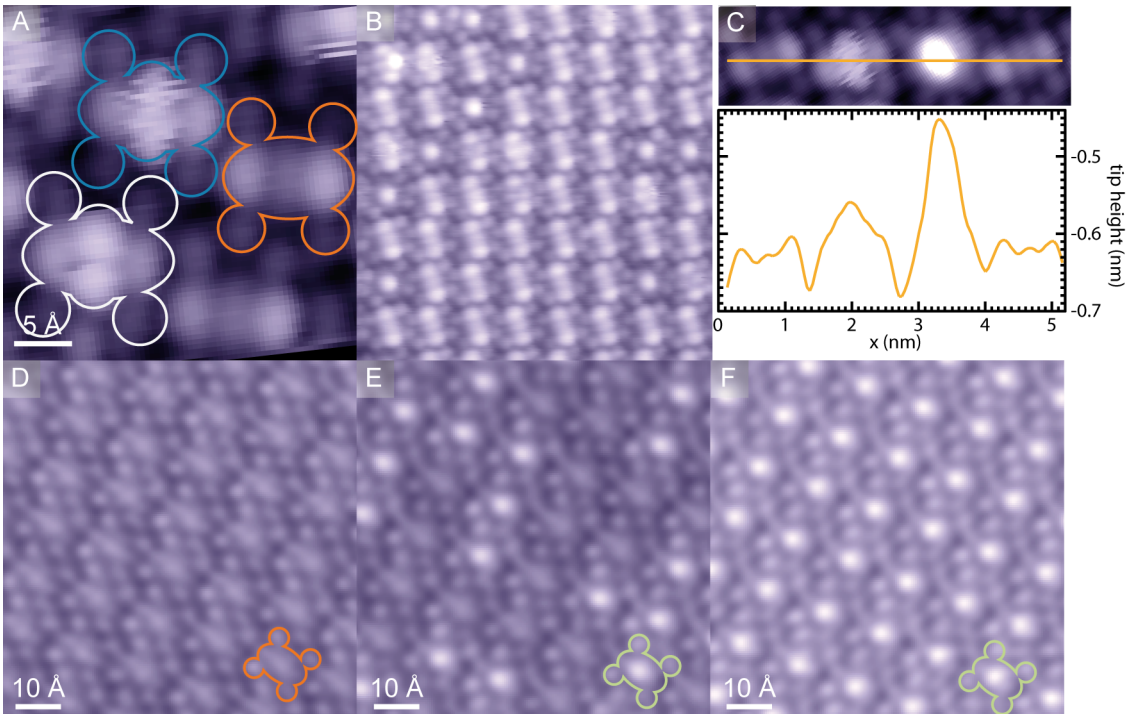

Figure 6.2 STM images of CO-ligation on Ru-TPP on Ag(111). (A) Ligation modes at 5 K: cis-geometry (white and blue) and uncapped (orange). (-1 V, 50 pA) (B) Overview image of the same surface, also showing axial CO ligation. (-0.9 V, 75 pA, 5 K). (C) Line profile across (left to right) a Ru-TPP, a Ru$(CO)_{Rider}$-TPP, a Ru(CO)-TPP and a Ru-TPP molecule on Ag(111), showing clearly the differences in the apparent height. (-1 V, 50 pA) (D-F) Evolution of Ru(CO)-TPP (green) formation in situ at 150 K under CO exposure (1.25 V, 80 pA)

outlined in white and blue). Their STM appearance is virtually identical to the μ-carbonyl rider ligation on Co-TPP and Fe-TPP, [153] and given a small residual pressure of CO (cf. Chapter 3), we can confidently assign those to the analogous Ru-TPP ligation. The molecule outlined in white can be identified as featuring a *cis*-μ-dicarbonyl binding geometry and the example outlined in blue is characteristic of a single CO adsorbed in the rider mode and switching between the two adsorption sides during the STM imaging.

Performing STM investigations at higher temperatures (150 K), we found solely a single mode of CO ligation, recognizable by uniform protrusions directly on top of the Ru centers (example outlined in green in Figure 6.2E,F). We attribute these to axial monodentate carbonyl. [151] Monitoring the same area of a Ru-TPP layer by STM (Figure 6.2D-F), while dosing CO in situ, we note that increasing the CO exposure led to an increase in the number of protrusions until all Ru-TPP molecules became brighter, which was achieved after a nominal exposure to ~ 2 Langmuir of CO. It should be noted that an estimate of the sticking coefficient cannot be extrapolated from the nominal value, as the real exposure will differ due to effects such as tip shadowing.

The CO ligands can be removed selectively by STM tip manipulations at 150 K as illustrated in the sequence of STM images in Figure 6.3A-C. At the position marked by the orange cross (Figure 6.3A), the voltage was ramped from 1.25 V to 2.20 V in a constant current mode (50 pA) while monitoring the tip height (Figure 6.3B). A sudden change in the vertical tip position at ~ 2.1 V indicates desorption of the CO ligand, which is confirmed by a follow-up image revealing a pristine Ru-TPP at the location of the voltage pulse (Figure 6.3C). This procedure

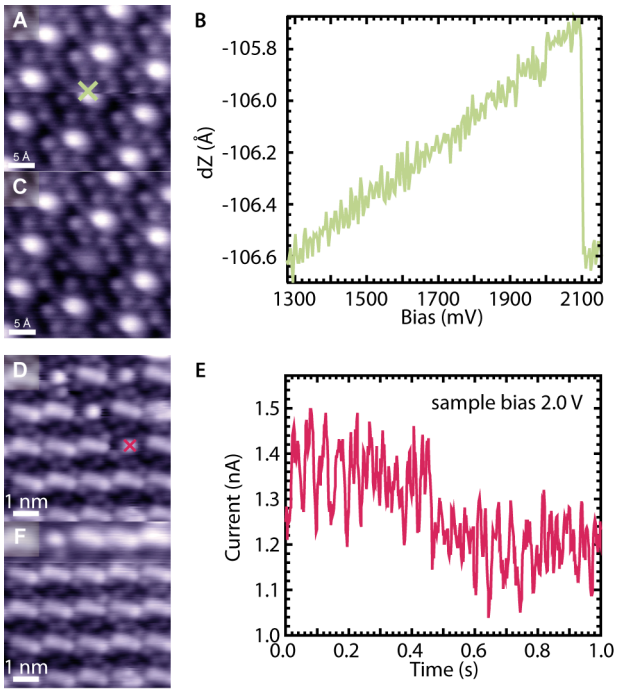

Figure 6.3 (A-C) Removal of a single CO ligand by a voltage pulse with the STM tip. (A) While recording the STM image (1.25 V, 50 pA, 150 K), a voltage pulse was applied at the position marked by the yellow cross. (B) Tip height profile of the voltage pulse from 1.25 V to 2.20 V, with a current of 50 pA. At $\sim$ 2.1 V the tip approaches the surface abruptly, indicating desorption of CO. (C) Follow-up STM image (1.25 V, 50 pA, 150 K) confirming the removal of the ligand. (D-F) Non-local STM tip manipulation. The STM images (-0.9 V, 80 pA, 5 K) were acquired before (D) and after (F) the tip manipulation. Axially ligated CO molecules can be recognized by the bright round protrusion in the center. At the position marked with a cross, the voltage was set to 2.0 V for 1 s with the feedback look turned off. The current trace during this operation is shown in the graph (E). The STM image after the manipulation shows the pristine Ru-TPP following the CO desorption from four molecules, three of which were axially ligated.

allows reliable removal of single CO ligands. On similar systems both tunnelling current induced desorption [151, 160] and electric field induced desorption [161] have been observed, though smaller bias voltages ($<$1 V) were required. For voltages $>$1.5 V, a non-local desorption is often reported. [150, 160, 162] Such a desorption behavior is also observed in this system with a bias voltage of 2.0 V, when higher tunneling currents are applied (Figure 6.3D-F).

To investigate the effect of the macrocyclic conformation on the CO ligation to the Ru center, we have investigated the adsorption behavior of Ru-TPP on Ag(111) after annealing to 620 K. This process causes cyclodehydrogenation reactions between the macrocycle periphery and the phenyl substituents, leading to a family of four Ru-TPP$_{pl}$. [60, 159] These can be identified by matching the characteristic outline of the structural formula (Figure 5.6A-D,6.4A) to the STM image (Figure 6.4B), whereas nc-AFM imaging can visualize more directly the chemical identity, as illustrated for one of the most frequently occurring ones in Figure 6.4C. The resulting porphyrin macrocycle appears to exhibit a subtle bowl shape with pyrrole tilt angles of 6° and 8° (see nc-AFM and respective simulation in Figure 6.4C,D) and also offers a coordinatively unsaturated metal center. We note that the surface depicted in Figure 6.4E has been exposed to the small amounts of CO at 5 K needed for the tip functionalization, however no evidence of the lateral adsorbate stabilization was found on the Ru-TPP$_{pl}$ molecules by STM/nc-AFM. As the rider ligation is associated with the saddle shape deformation,

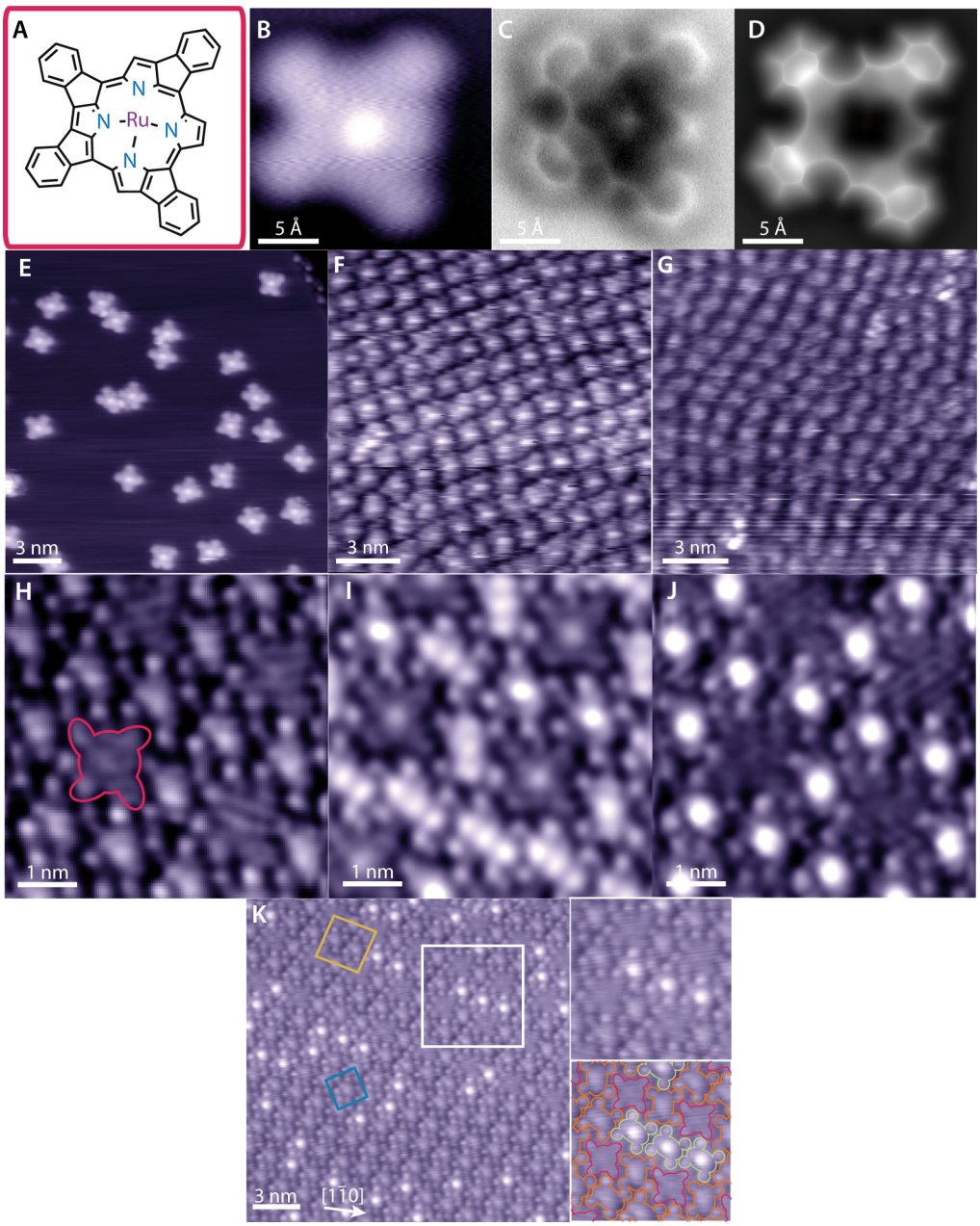

Figure 6.4 (A) Structural formula of one of the four planarized Ru tetraphenyl porphyrin derivatives (Ru-TPP$_{pl}$), as previously shown in Fig. 5.6. (B-D) Images of the Ru-TPP$_{pl}$ shown in A on Ag(111). (B) STM (-50 mV, 50 pA, 5 K). (C) non-contact AFM (nc-AFM) frequency shift image (tip height Z = -20 pm with respect to the STM set point above Ag(111), oscillation amplitude 80 pm, 5 K). (D) nc-AFM simulation. (E-J) STM images of Ru-TPP$_{pl}$. (E) STM overview image (-0.5 V, 50 pA) of the mixture of Ru-TPP$_{pl}$ after CO exposure at 5 K. The bright central protrusion arises from the Ru center. (F-G) Densely packed Ru-TPP$_{pl}$ layers imaged at 150 K before (F) and after (G) CO exposure (F: -0.5 V, 100 pA, G: -0.6 V, 70 pA). (H-J) Mixed layer of the Ru-TPP$_{pl}$ product shown in Figure 5.6D and Ru-TPP before (H), during (I) and after (J) CO exposure at 150 K (H,J: 1.25 V, 50 pA, (I) -1.25 V, 50 pA). (K) STM image (1.25 V, 80 pA, 150 K) of a layer of Ru-TPP and Ru-TPP$_{pl}$. The unit cell for the Ru-TPP lattice is marked in blue, for the mixed Ru-TPP/Ru-TPP$_{pl}$ lattice in orange. The area shown in the white box is magnified on the right, in the bottom image the different molecules are outlined: Ru-TPP$_{pl}$ (red), Ru-TPP (orange) and Ru(CO)-TPP (green).

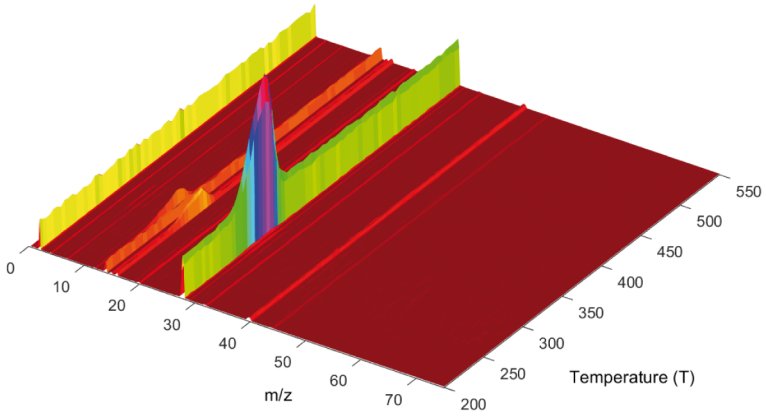

Figure 6.5 2D-TPD spectra of CO desorption from Ru-TPP. CO was deposited at 200 K, the heating rate was set to 2 K/s. Only peaks related to CO (m/z = 12,16,28) can be observed.

[153] we would not expect this bowl configuration to permit such ligation. However, it is with some surprise that we do not observe an axial ligation at all. The protrusion in the center of Ru-TPP$_{pl}$ observed in STM at negative bias (Figure 6.4B,E-G,I) arises, similarly to Ru-TPP, from the Ru center (cf. UPS below, [124]) and is not related to potential CO adsorption, as confirmed by the corresponding nc-AFM image (Figure 6.4C). At experiments of methodical exposure of Ru-TPP$_{pl}$/Ag(111) to CO at 150 K (Figure 6.4F-J) no CO uptake by Ru-TPP$_{pl}$ was observed in STM data.

To corroborate the difference in adsorption behavior clearly with the same STM tip conditions, we prepared a sample containing both Ru-TPP and Ru-TPP$_{pl}$ molecules on Ag(111) (Figure 6.4H). In this mixed lattice exclusively the planarized derivative shown in Figure 5.6D appears. This effect is associated with the different molecular shapes of other product species that do not fit into the expressed overlayer lattice (Figure 6.4K). [132] The (stepwise) exposure of this layer to doses of CO at 150 K resulted in saturating exclusively all Ru-TPP centers with CO (Figure 6.4J), whereas no changes were encountered for the Ru-TPP$_{pl}$ species. An intermediate CO coverage acquired at negative bias (Figure 6.4I) highlights the difference in STM appearance between Ru-TPP, Ru(CO)-TPP and Ru-TPP$_{pl}$.

Binding energy and desorption kinetics

To deduce information about the bond strength of the axially ligated CO on the Ru-TPP layer and to confirm that CO does not ligate to the Ru-TPP$_{pl}$ under the same conditions, we carried out systematic TPD measurements. After exposure of the square phase of Ru-TPP on Ag(111) to CO, our results show exclusively CO desorption (Figure 6.5) in the temperature range of 200-550 K. Dosing different amounts of CO onto a layer of Ru-TPP has no effect on the shape of the desorption curve, but only on the intensity (Figure 6.6A, purple), indicative of first order desorption kinetics. The acquired spectra can be modelled by assuming a pre-exponential factor of $\nu = 10^{13}\,s^{-1}$ and including two first-order desorption processes of equal intensities with energies of $E_{des,1} = 0.80$ eV and $E_{des,2} = 0.84$ eV (more information about the fitting can be found in Chapter 3). Applying the same fitting to desorption spectra taken at different heating rates β (Figure 6.6B) results as well in a good agreement. The dif-

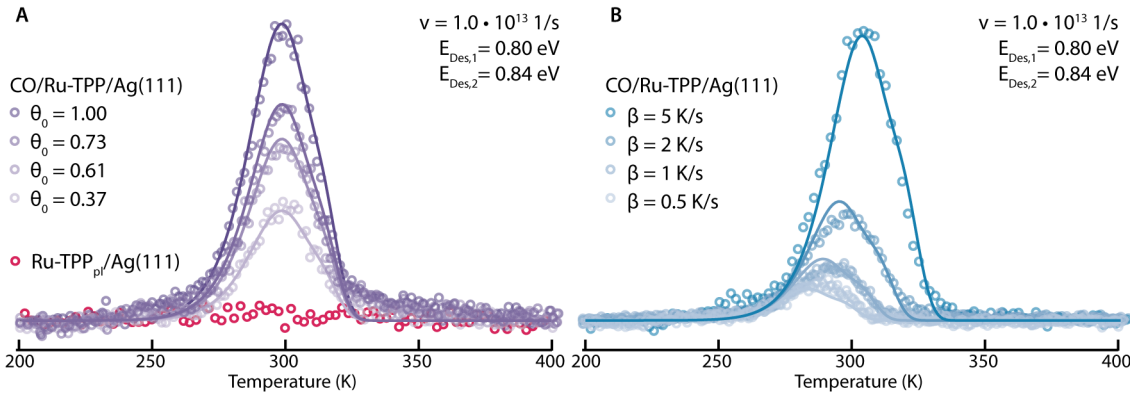

Figure 6.6 (A) Coverage dependent TPD spectra and fitting of CO desorption for m/z = 28. Different shades of purple indicate different initial CO coverages, θ_0, dosed at 200 K, on the same Ru-TPP layer. A heating rate of 2 K/s was used. The red spectrum shows the same trace for Ru-TPP$_{pl}$ after CO exposure, confirming that CO is not ligating. (B) Heating rate dependent TPD spectra and fitting, the different shades of blue indicate different heating rates applied. All spectra were taken on the same Ru-TPP layer with an initial coverage $\theta_0 = 1$.

ference in binding energy of 0.04 eV could be related to the Ru(CO)-TPP adsorption on both *fcc* and *hcp* hollow sites of the Ag(111) (see Chapter 5, [159]). We note that consistently with our experiments, in such a case we would not expect a preferential occupation for the lower binding adsorption site, as no exchange of CO between the molecules is possible at 200 K and the desorption temperature from the Ag(111) is much lower. [163] However, we cannot exclude a more complex desorption behaviour as a cause for the shape of the desorption spectra. While the desorption energy is very comparable to values found for Ru(CO)-TPP on the more reactive Cu(110) surface, [151] it is significantly weaker compared to gas-phase molecules. [32] After exposing a layer of Ru-TPP$_{pl}$ to CO, there is no desorption trace of CO detected (Figure 6.6A, red), confirming the results from STM/AFM measurements that CO is not ligating to Ru-TPP$_{pl}$.

At this stage, the following two questions arise: (1) How is the Ru-TPP affected by the CO ligation? (2) Why are these very similar porphyrins so different in their chemical reactivity? The following analysis will discuss the impact of the CO ligation on electronic and geometric properties of the Ru-TPP.

Electronic structure

We initially investigated the XPS signature of the Ru 3d$_{5/2}$ core level as a measure of the electronic interaction with the metal substrate (Figure 6.7A). Upon ligation of CO, the binding energy of the Ru 3d$_{5/2}$ core level shifts by 2.4 eV towards higher binding energies, indicating a decoupling of the Ru center from the Ag substrate. The shift towards higher binding energies is in good accord with the DFT prediction (+1.8 eV). Note that the Ru 3d$_{3/2}$ component is coincident with the C 1s peak ($\sim$ 285 eV), and can be observed as a small shoulder on the lower binding energy side for Ru-TPP and at the higher binding energy side for Ru(CO)-TPP layers. [121]

From the XPS of a multilayer of Ru(CO)-TPP on Ag(111) one can deduce that the CO ligand remains attached to the Ru-TPP on the layers without direct contact to the Ag(111)

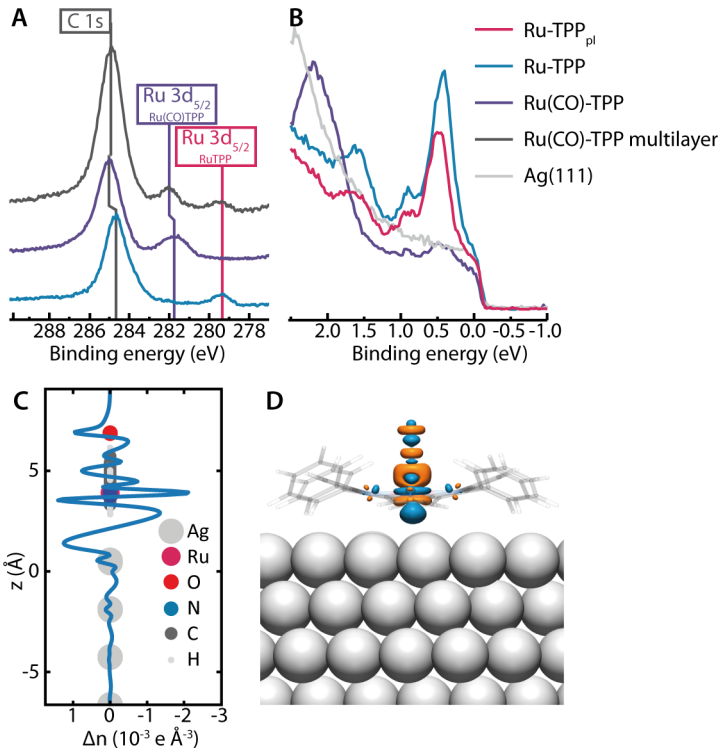

Figure 6.7 (A) XP spectra of the C 1s / Ru 3d region corresponding (from bottom to top) to submonolayer coverages of pristine Ru-TPP on Ag(111) (300 K), CO ligated Ru-TPP (80 K) and a multilayer of Ru(CO)-TPP on Ag(111) (300 K). (B) UP spectra for clean Ag(111) (gray), pristine Ru-TPP (blue), Ru(CO)-TPP (purple) and Ru-TPP$_{pl}$ (red). (C,D) Charge density redistribution upon CO adsorption on Ru-TPP on Ag(111) deduced from DFT. The one dimensional plot (C) shows differences in the electron density normal to the Ag(111) surface, the three dimensional plot (D) shows isosurfaces (0.04 e Å^{-3}) indicating gain of electron density (orange) and loss of electron density (blue).

substrate at 300 K. [164] The binding energy for the Ru 3d$_{5/2}$ core level of Ru(CO)-TPP directly on Ag(111) is 0.2 eV lower than that observed in the multilayer films. Such a shift is consistent with the expected polarization screening by the metal substrate.

UP spectra further show states for both Ru-TPP (Figure 6.7B, blue) and Ru-TPP$_{pl}$ (Figure 6.7B, red) at binding energies of 0.4 eV and 0.9 eV, which can be correlated to the bright protrusion at negative bias voltages in the STM images (Figure 6.2A, 6.4B,E,I), similar to Co-TPP on Ag(111). [25] These Ru states are extinguished for Ru(CO)-TPP (Figure 6.7B, purple), indicating that the interaction of Ru centers and the Ag substrate, responsible for these states, is no longer present upon ligation. [152]

Further insight into the electronic changes upon the adsorption of CO is gained from DFT. Figure 6.7C shows that changes in the electron density upon CO adsorption are not restricted to the porphyrin, but also evident in the Ru-TPP/Ag(111) interface. The charge at the interface per molecule is significantly reduced upon CO ligation ($\Delta q_{Int} = -0.47\,e$, $q_{Int} = 0.18\,e$), confirming the electronic decoupling of the Ru-TPP molecules from the Ag(111) surface correlated to the CO ligation and surface *trans*-effect. While the CO is negatively charged ($q_{CO} = -0.18\,e$), the Ru center gets more positively charged ($\Delta q_{Ru} = 0.27\,e$). A closer inspection of the orbital structure (Figure 6.7D) reveals a decreased electron density in the 5σ orbitals of the CO and a commensurate increase in electron density in the 2π orbitals, in agreement with the Blyholder model for chemisorbed carbon monoxide. [165] On the ruthenium center, a de-

Table 6.1 XPS binding energies of Ru 3d, C 1s, and N 1s core levels of Ru-TPP and Ru(CO)-TPP.

XPS	Ru-TPP	Ru(CO)-TPP	Ru(CO)-TPP multilayer
Ru $3d_{5/2}$	279.4 ± 0.1 eV		279.4 ± 0.1 eV
Ru $3d_{5/2}$ (CO ligated)		281.8 ± 0.1 eV	282.0 ± 0.1 eV
C 1s	284.7 ± 0.1 eV	285.0 ± 0.1 eV	284.9 ± 0.1 eV
N 1s	398.6 ± 0.1 eV	398.9 ± 0.1 eV	398.8 ± 0.1 eV

crease of electron density in the d_{z^2} orbital, as well as an increase in the d_{zx} and d_{yz} orbitals is observed. It is notable that this change in the Ru 3d electron density is similar between, both, the Ru-CO , and Ru-Ag, whereas for Ru-TPP_{pl} (Figure 5.6B) the corresponding DFT calculations find the electron accumulation to be in d_{z^2} and depletion in the d_{zx}, d_{yz} orbitals. [159] The depletion and gain of electrons in orbitals of both Ru and CO show a back-donation of electrons from the Ru center to the CO ligand, which in addition to the decoupling can contribute to the increase in binding energy of the Ru $3d_{5/2}$ core level upon CO ligation (Figure 6.7A).

Structural determination

Our earlier structural investigation of Ru-TPP and Ru-TPP_{pl} has shown that the adsorption height of the Ru center differs only by 0.14 Å (Chapter 5, [159]). Nevertheless, the adsorption height of the Ru center of Ru-TPP increases upon CO ligation at 200 K by 0.59 Å from 2.59 ± 0.05 Å (see Chapter 5, [159]) to 3.18 ± 0.12 Å, as shown by NIXSW data of the Ru(CO)-TPP (Figure 6.8A, Table 6.2). The high coherent fraction indicates a very well-defined adsorption height for the molecules, confirming a rather uniform geometry. The C 1s NIXSW data (Figure 6.2B, Table 6.2) show an increased average adsorption height also for the carbon atoms. Thus, we conclude that the non-planarity of the Ru-TPP facilitates a conformational change of the entire Ru-TPP upon CO ligation and enables the decoupling of the Ru center from the Ag surface. One should note that the NIXSW measurements could only be performed on mixed layers of Ru(CO)-TPP and pristine Ru-TPP. While the Ru $3d_{5/2}$ peaks of the two species can be clearly distinguished due to the large shift in binding energy (Figure 6.7A, Table 6.1), allowing the adsorption height for each species to be analyzed individually, this is not possible for the C 1s. The carbon spectra, as described above, have to be understood as an average over all carbon atoms from both species, which includes additionally a negligible contribution of the Ru $3d_{3/2}$ core level. Therefore, only a qualitative comparison is meaningful. With this in mind, the X-ray standing wave (XSW) results are in excellent agreement with complementary DFT calculations (Figure 6.8C, Table 6.2), which predict an increase of the Ru adsorption height of 0.69 Å and an increase of the average C adsorption height of 0.11 Å. We propose that the porphyrin macrocycle can be lifted, while the phenyl substituents remain in contact with the Ag(111) substrate. These conformational adaptations can be interpreted as a rather strong surface *trans*-effect. [136, 154, 166]

To understand the anticipated structural *trans*-effect for planarized Ru(CO)-TPP derivatives, we investigated a DFT geometry optimization (Figure 6.8D). Here, the *trans*-effect would increase the Ru adsorption height by 0.49 Å whereas it would leave the macrocycle

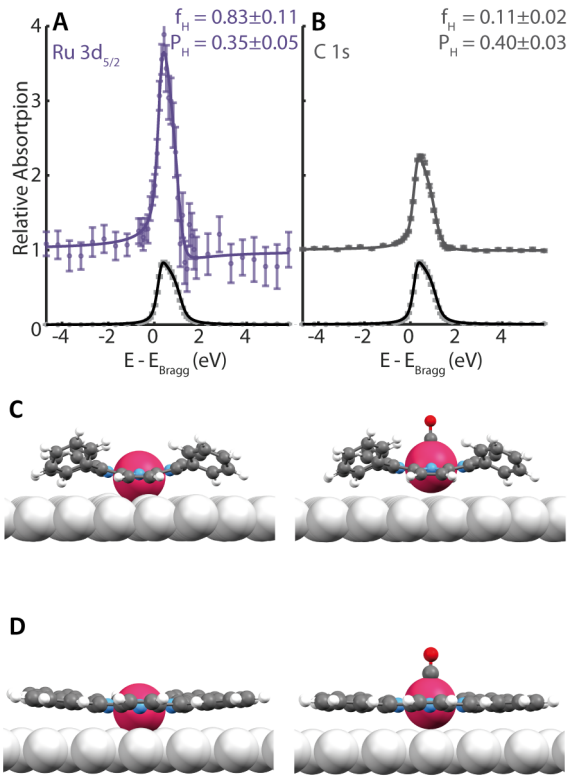

Figure 6.8 (A,B) NIXSW photoelectron profiles and fits of the Ru $3d_{5/2}$ and C 1s regions in (111) reflection for Ru(CO)-TPP. Purple (dark gray) dots indicate the Ru (C) data points, light gray dots the reflection of the Ag(111) substrate. (C) DFT model of Ru-TPP (left) and Ru(CO)-TPP (right) on Ag(111). (D) DFT model of Ru-TPP_{pl} (left) and Ru(CO)-TPP_{pl} (right) on Ag(111). Ru, Ag, C, N, O and H atoms are depicted in red, silver, black, blue and white, respectively.

Table 6.2 DFT and NIXSW results for Ru $3d_{5/2}$ and C 1s core levels for the different investigated systems. The adsorption heights are deduced from the coherent position, for the C atoms it is an average value. In parentheses, we report the DFT simulated adsorption height that would be the result of the respective NIXSW measurement for comparison.

	DFT α-/κ-pyr tilt angle	Adsorption height (Å) Ru	C	**NIXSW** Adsorption height (Å) Ru $3d_{5/2}$	C 1s
Ru-TPP	28° / −9°	2.68	3.53 (3.20)	2.59 ± 0.05	3.02 ± 0.07
Ru(CO)-TPP	23° / −4°	3.37	3.64 (3.44)	3.18 ± 0.12	3.30 ± 0.07
Ru-TPP_{pl}	8°, 6°	2.48	3.01 (3.01)	2.45 ± 0.02	2.99 ± 0.05
Ru(CO)-TPP_{pl}	5°, 0°	2.97	2.99 (2.99)		

mostly unaffected (Table 6.2). In comparison with the saddle-shaped pristine TPP, these deformations are smaller and show less adaptation of the macrocycle with CO ligation, which is more restricted by its adsorption to the silver surface.

It is notable that the planarized Ru(CO)-TPP derivative investigated is also a stable geometry in simulation with a binding energy of the CO predicted to be smaller by $0.5\,\mathrm{eV}$ with respect to the pristine Ru-TPP. We can thus attribute the lack of experimental evidence of this species to either a higher activation barrier associated with the decoupling of the Ru from the silver surface or to CO sticking coefficient differences of more than an order of magnitude.

Conclusion

We have have studied the CO ligation on distinct Ru-porphyrins on a silver surface by a combined theoretical and experimental analysis of the electronic and geometric effects of such a ligation.

Rider CO-ligation at low temperatures (at 5 K) and axial CO-ligation (up to $\sim$ 250 K), in agreement with the Blyholder model for chemisorption, were observed only for the pristine saddle-shape Ru-TPP. STM allowed tip induced desorption of single ligands without damaging the Ru-TPP underneath, which can be used to create patterns on a nanometer scale. The large shift in binding energy of the Ru $3d_{5/2}$ core level upon axial ligation indicated an electronic decoupling of the Ru center from the surface and both NIXSW and DFT have confirmed significant conformational changes. While the Ru center is affected the most, increasing in adsorption height by ~ 0.6 Å, an increase of the adsorption height is observed for the entire molecule (Figure 6.8C). From TPD we determined the desorption energy of the axial CO ligand to $(0.8 \pm 0.1)\,\mathrm{eV}$, reduced by $1.1\,\mathrm{eV}$ in comparison to the CO binding strength of the free Ru-TPP.

For the planarized Ru-TPP derivatives, there was no sign of CO ligation in STM, AFM and TPD measurements. With the bonding of the center Ru to the Ag surface being similar for both investigated porphyrins, our results emphasize the crucial role of the flexibility of the Ru-TPP in the ligation process and the related ease of decoupling of the Ru center from the Ag(111) surface.

Our findings with this model Ru-porphyrin/Ag(111) system are expected to be relevant to the elucidation to processes related to gas sensing,[167–169] and to supported single atom catalysts (e.g. Ru-N_4).

7 Assembly and manipulation of a prototypical N-heterocyclic carbene with a metalloporphyrin pedestal on a solid surface

This Chapter includes content that has been published in

P. Knecht, B. Zhang, J. Reichert, D. A. Duncan, M. Schwarz, F. Haag, P. T. P. Ryan, T.-L. Lee, P. S. Deimel, P. Feulner, F. Allegretti, W. Auwärter, G. Médard, A. P. Seitsonen, J. V. Barth, A. C. Papageorgiou, **Assembly and Manipulation of a Prototypical N-Heterocyclic Carbene with a Metalloporphyrin Pedestal on a Solid Surface**, *J. Am. Chem. Soc.*, 2021, **143**, 4433-4439.

The modular assembly of robust, metal-organic structures at interfaces offers composite systems suitable for device fabrication and with functions controlled by the choice of building blocks and their arrangement. Since it was discovered that N-heterocyclic carbenes (NHCs) are stable carbenes that can be crystallized, their unique properties have been eagerly explored in novel organometallic materials, metallopharmaceuticals, catalysts and surface functionalization. [33] As NHCs are able to coordinate to transition metals as well as p-block elements, they have been excellent ligands to diverse surfaces ranging from metals to semiconductors and, more recently, oxides. [170–172] Examples illustrating functional materials with NHC stabilized interfaces include Ru nanoparticles for hydrogenation catalysis [173] and soluble Au nanorods for phototherapy. [174, 175] One of the key properties of these ligands is that their substituents are amenable by synthesis. Therefore on extended metal surfaces they can offer anchors for tethering further functional groups, such as catalytically active complexes, [176] or provide chiral centers exploited in unidirectional molecular rotation [177] and chiral sensing. [178]

Recent studies on the interface of NHCs with metal surfaces have found that NHC adsorbates often bond to the surface via an adatom, [61] and may form both upstanding and planar bis-carbene metal adatom complexes. [61, 62, 171, 179, 180] The abstraction of this bonding adatom from the surface may lead to surface structure modifications and surface instabilities, [174, 175, 181] which could result in less physicochemically defined systems. To circumvent such modifications, alternative carbenes, [182] which do not bond via adatoms, as well as tethering NHCs carrying their own adatoms [174, 175] have been employed. Within this work we propose a novel strategy to harness NHC chemistry for surface functionalization while

gaining control over both the orientation and the surface spacing of NHCs. This approach features a macrocycle which hosts the adatom guest in its center, making a surface pedestal for the NHC. Accordingly, we show that a porphyrin metal complex acts as a suitable surface pedestal, onto which an NHC molecule is forced to adsorb and "stand".

Porphyrins are well-established building blocks for functional surfaces. [108, 111] As such, their surface chemistry has been extensively investigated, and bottom-up assembly scenarios in low-dimensional nanoarchitectures have been developed. However hitherto, the functionalization of such metalloporphyrin pedestals with commonly employed ligands of supramolecular chemistry on metal surfaces has proven challenging. For example binding would occur only at low temperatures (below room temperature), [183, 184] limiting its applicability, whereas another ligand was found to intercalate between the metal porphyrin and the surface. [185]

To assess whether metalloporphyrins can provide a suitable pedestal for the atomically precise positioning and arrangement of NHCs, we investigate the NHC interaction with a single layer of metalloporphyrins on a metal surface. This might seem contradictory to the fabrication scheme of traditional metal-organic frameworks (MOFs) on thiolate or carbene self-assembled monolayers (SAMs), [178, 186] where the template sequence is opposite, but it is rooted in recent observations that tetrapyrrole compounds intercalate the SAM/metal interface. [164]

Inspired by the synthesis of the catalytically active porphyrin Ru-NHC compounds, [187] we employ the same tectons (metalloporphyrin: Ru tetraphenyl porphyrin (Ru-TPP); NHC: 1,3-dimethyl-2*H*-imidazol-1-ium-2-ide (IMe), Figure 3.6) on the Ag(111) single crystal surface, a substrate on which we have previously characterized both the self-assembly and molecular coupling of our individual building blocks. [61, 159] To elucidate unambiguously the key molecular events and surface properties, we work under ultra-high vacuum (UHV) conditions and utilize a methodology combining high-resolution scanning tunneling microscopy (STM) and manipulation, X-ray photoelectron spectroscopy (XPS), normal incidence X-ray standing wave (NIXSW), and temperature programmed desorption (TPD), coupled with ab initio calculations by density functional theory (DFT).

Results and discussion

On the Ag(111) surface, Ru-TPP molecules (Figure 3.6) adopt a saddle-shape conformation, i.e., two opposite pyrroles of the macrocycle bend upward ($\acute{\alpha}\nu\omega$, α-pyr) and the other two bend downward ($\kappa\acute{\alpha}\tau\omega$, κ-pyr), and self-assemble into a square phase. [159] In STM images, a single molecule (Figure 7.1A) can be identified by three brighter protrusions which signify the Ru atom in the center and the two α-pyr's of the macrocycle; four smaller protrusions correspond to the phenyl substituents.

Depositing IMe (Figure 3.6) at room temperature (RT) onto a submonolayer coverage of Ru-TPP on Ag(111) results in a major change of the appearance of the single molecules in STM (Figure 7.1B,E), without a significant change in the Ru-TPP self-assembly. This finding is similar to STM investigations carried out at both low temperature (5 K) and room temper-

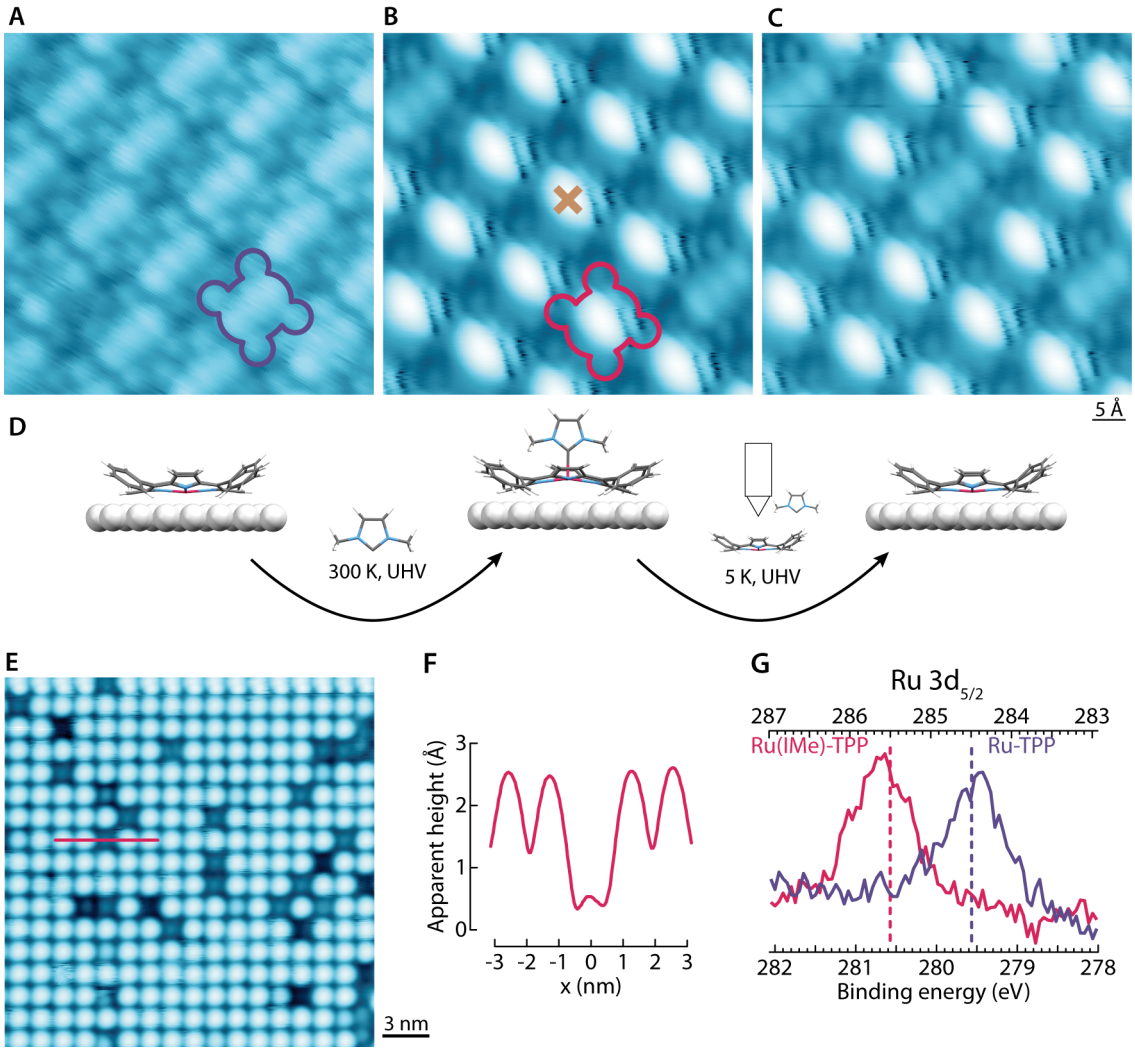

Figure 7.1 Addressable NHC pillars on a two dimensional (2D) array of Ru-TPP on the Ag(111) surface. (A) STM image of the self-assembled square phase Ru-TPP on Ag(111) (-0.5 V, 50 pA, 5 K). A single molecule is outlined in purple. (B) STM image of IMe on Ru-TPP/Ag(111) (-1.3 V, 50 pA, 5 K). The red shape outlines an Ru-TPP capped by IMe. The brown cross indicates the position where a manipulation operation was performed. (C) STM image (-1.3 V, 50 pA, 5 K) of the same area as in (B), following the removal of a single IMe and revealing the pristine, unperturbed Ru-TPP molecule underneath. (D) Schematic of the IMe functionalization and manipulation procedure: Starting with square-phase Ru-TPP on Ag(111) (left panel, model of DFT optimized geometry), exposure to IMe vapor at 300 K leads to the formation of Ru(IMe)-TPP on Ag(111)(middle panel, model of DFT optimized geometry). Using STM tip manipulation on Ru(IMe)-TPP on Ag(111) at 5 K, the IMe ligand can be selectively removed (right panel). (E) Overview image of a porphyrin island of $\sim$90 % Ru(IMe)-TPP and $\sim$10 % Ru-TPP (1.0 V, 75 pA, 5 K). (F) Line scan marked in (E). (G) XP spectra of the Ru $3d_{5/2}$ region corresponding to pristine Ru-TPP (purple) and Ru(IMe)-TPP (red) on Ag(111). The dashed lines correspond to the calculated binding energies by DFT, with the respective binding energy scale on the top.

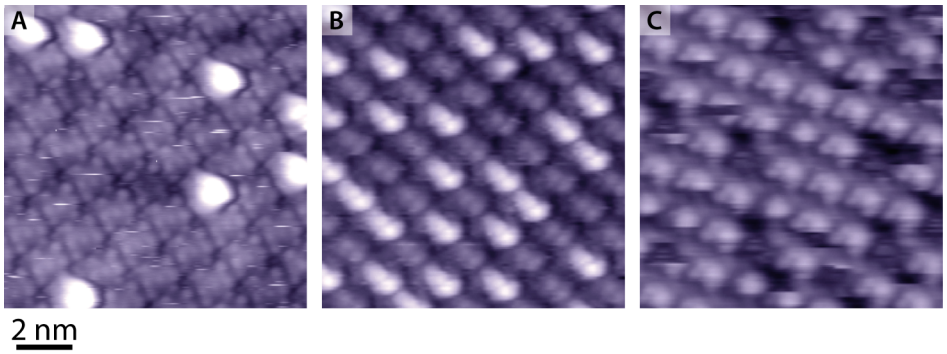

Figure 7.2 STM images of IMe ligation images at RT with different coverages of IMe. (A) $-1.3\,\mathrm{V}$, 80 pA. (B) 1.0 V, 100 pA. (C) 1.4 V, 60 pA.

ature (300 K, Figure 7.2). While the square-phase arrangement of the Ru-TPP can still be recognized, a single brighter protrusion located at the center of the porphyrin is now observed for the majority of the Ru-TPP molecules, indicating the capping of Ru-TPP by IMe. The apparent height difference between the pristine Ru-TPP and the capped Ru-TPP amounts to $\sim$2 Å (Figure 7.1F). We assign the new brighter protrusions to single IMe ligands, consistent with STM investigations of CO/Ru-TPP on Cu(110) [151] or on Ag(111) (Chapter 6, [159]).

The arrangement of the NHCs on the surface via the Ru-TPP pedestal offers unique possibilities for the controlled manipulation of individual ligands in self-assembled layers, which are not present for densely packed layers of upstanding NHCs directly attached to metal surfaces. The NHC ligands adsorbed on Ru-TPP/Ag(111) can be selectively removed by STM tip manipulation. Figure 7.1B shows an area of Ru-TPP molecules capped by IMe: the brown marker indicates the position of subsequent manipulation with the STM tip. After the manipulation operation, we detect a pristine Ru-TPP without the IMe ligand in the same position (Figure 7.1C). No other change is observed in the monitored area, indicating that a single IMe has been removed by the STM tip. The following manipulation protocol has been reproducibly applied in addressing single IMe: positioning the tip on top of an IMe ligand; turning off the feedback loop; setting the bias voltage to $-3\,\mathrm{V}$; and allowing the tip to approach the sample by 2 Å (Figure 7.3A-C). We can therefore use this as a nanoscale tool (Figure 7.1D) with a printing resolution of 1 dot per 1.4 nm (Figure 7.1E). To demonstrate this, the TUM logo was created by removing individual IMe ligands and imaging at intermediate stages to monitor the writing process (Figure 7.3D-H).

The bonding strength of IMe ligands to Ru-TPP was examined by TPD (Figure 7.4A). The TPD spectra, monitoring the desorption of the IMe parent ion, evidence the desorption of the intact NHC (Figure 7.4C). Thus, we prove that its reversible bonding to the Ru-TPP is mediated via the carbene and not via a potential reaction at a different IMe site, which would result in fragmentation of the adsorbed IMe. [179] The shape of the spectra does not change with different initial coverages θ_0 of IMe on the same Ru-TPP layer (see Figure 7.4A), indicating unimolecular desorption. A shoulder is visible in all TPD spectra towards higher temperatures, $\sim$370 K, indicating the existence of a second component. Because IMe desorption from the Ag(111) substrate occurs at slightly higher temperatures (Figure 7.4B), we ascribe this shoulder to the desorption of IMe from Ru-TPP molecules that are not part of

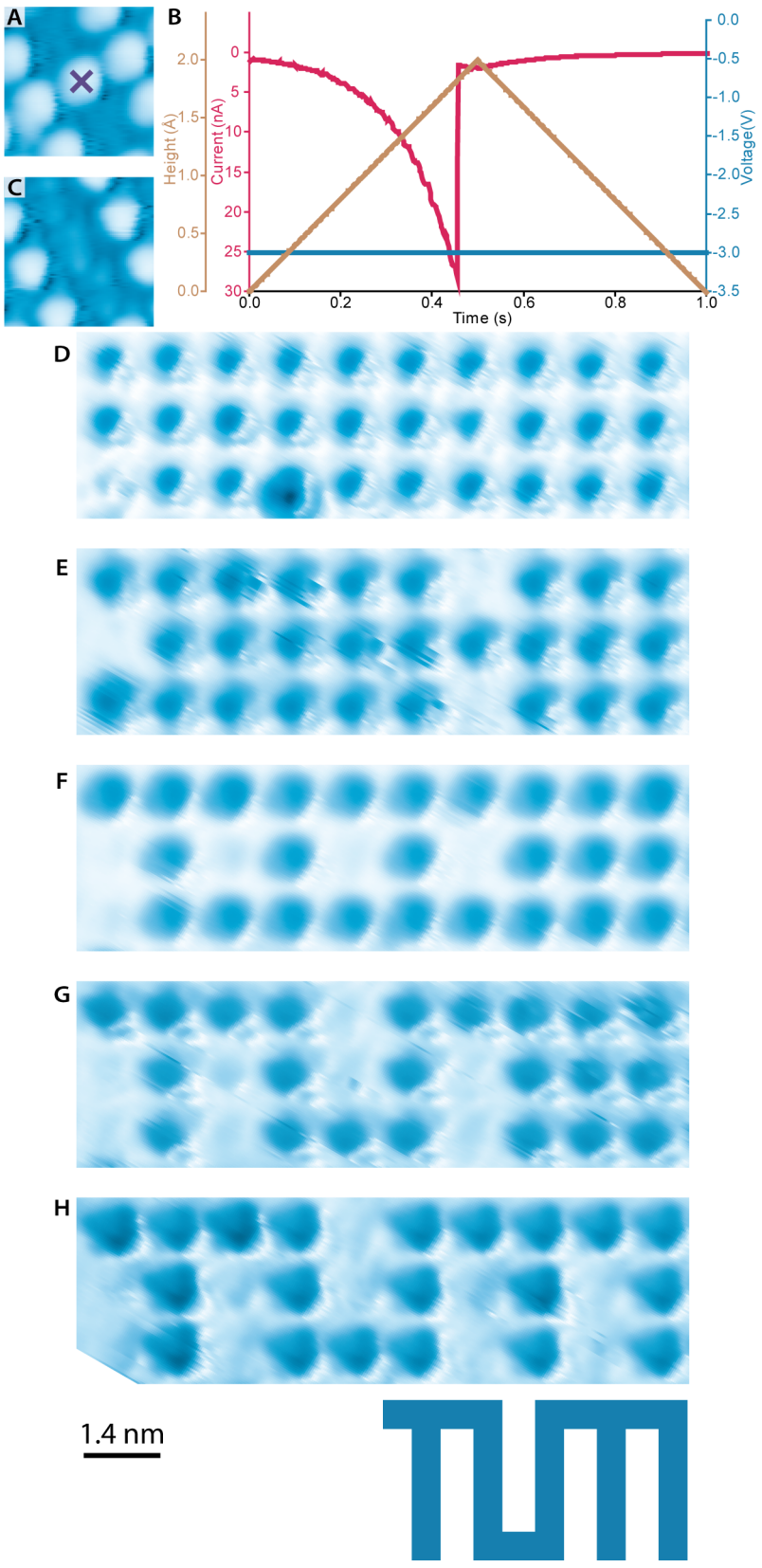

Figure 7.3 Removal of single IMe molecules from Ru-TPP on Ag(111) by STM tip manipulation. (A) STM image before the manipulation, marked by the cross. (B) Typical profiles of the tip height (brown), current (raspberry), and bias voltage (blue) during the manipulation. (C) STM image of the same area as in (a) after the manipulation. (D-H) STM images of the subsequent removal of single IMe molecules in order to recreate the Technical University of Munich (TUM) logo, shown on the bottom as reference. The color scale is inverted for these images: the blue protrusions correspond to the Ru(IMe)-TPP complexes. All STM images were taken at -0.7 V, 50 pA, 5 K.

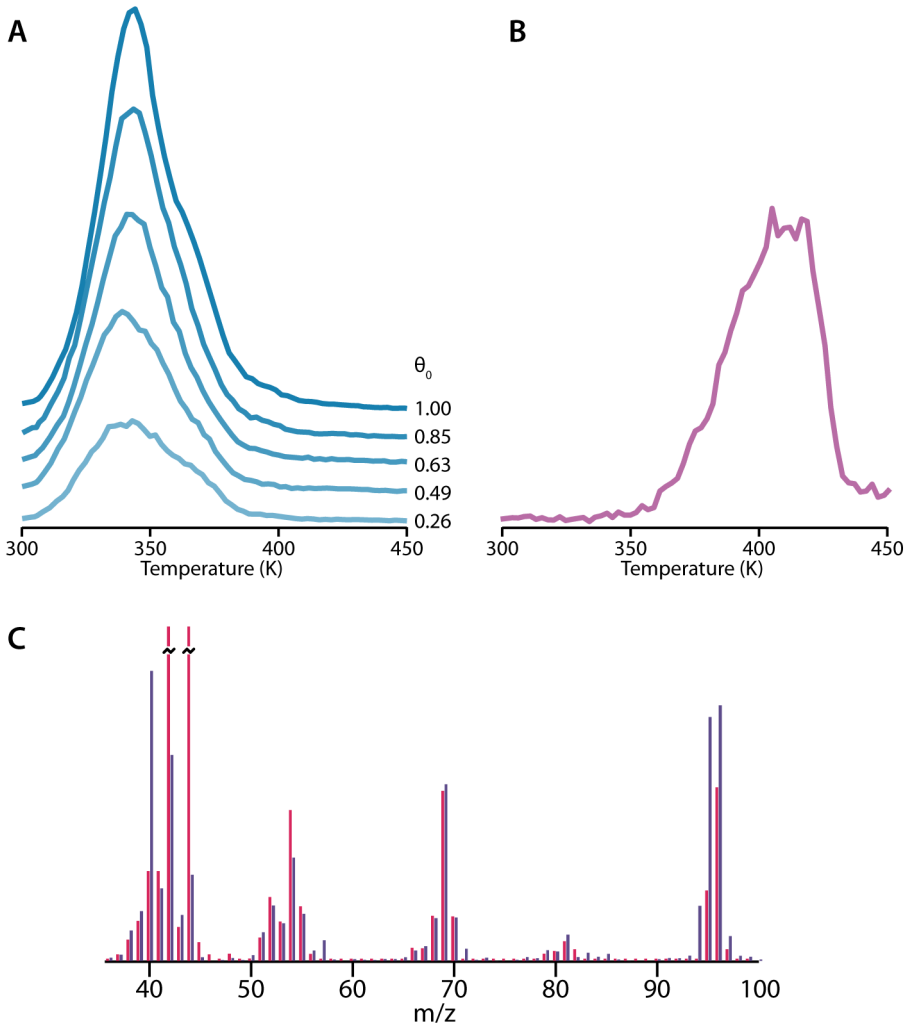

Figure 7.4 TPD spectra for IMe desorption. (A) Desorption curves for IMe on Ru-TPP/Ag(111) (m/z = 96, corresponding to the parent ion of IMe, heating rate β = 2 Ks^{-1}). The spectra correspond to different initial coverages of IMe, θ_0, up to a saturation of all Ru-TPP molecules (θ_0 = 1) and are offset vertically for clarity. (B) Desorption curve of a submonolayer coverage of IMe on Ag(111) (m/z = 96, β = 1 Ks^{-1}). (C) Mass spectra from TPD measurements of IMe on Ru-TPP (blue) and during deposition of IMe (red), in good agreement with reported spectra. [63] During deposition the component at m/z = 44, related to CO_2, which detaches during the evaporation, is significantly larger. Other smaller differences in the relative intensities of the single peaks arise due to different acquisition settings and different mass spectrometers used.

self-assembled islands, but are diffusing on free areas of the Ag(111) substrate. The lower desorption energy of the IMe from the self-assembled islands can be rationalized by the IMe related charge transfer (c.f. DFT analysis) which would result in repulsive interactions. From transition-state theory, a frequency factor of $\nu \approx 10^{13}\,\mathrm{s}^{-1}$ is assumed, allowing us to estimate the desorption energies of IMe via the Redhead equation as E_D = 0.93 eV for the main component and E_D = 1.00 eV for the shoulder. The TPD results shown in Fig. 7.4A are reproducible after several cycles of adsorption and desorption on the same Ru-TPP layer.

To confirm that the IMe is binding to the Ru atom, XP spectra probed the Ru 3d$_{5/2}$ region (Figure 7.1G). This Ru core level shows a shift of 1.2 eV toward higher binding energy upon capping Ru-TPP with IMe: from 279.4 eV (purple) to 280.6 eV (red). The low Ru 3d$_{5/2}$ binding energy of Ru-TPP/Ag(111) has been attributed to a covalent-like coupling of the Ru atom to the Ag(111) (chemisorbed Ru-TPP). [159] Once IMe caps the Ru-TPP molecule, the coupling

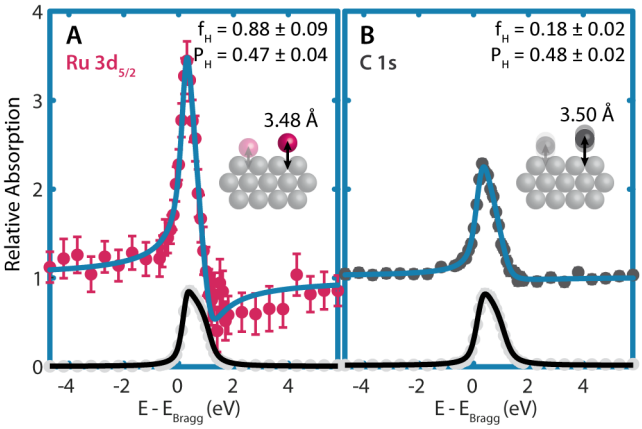

Figure 7.5 NIXSW results showing the NHC ligation-induced lift-off of Ru-TPP from Ag(111). (A) Ru 3d$_{5/2}$ and (B) C 1s X-ray standing wave (XSW) profiles corresponding to IMe dosed on a layer of Ru-TPP ($\sim$0.35 molecules nm^{-2}) on Ag(111). Coherent fraction, f$_H$, and coherent position, P$_H$, values are given for each spectrum. The models in the insets elucidate the deduced atomic adsorption height upon NHC ligation. Faint spheres on the left mark the adsorption height before ligation. The vertical 'blurriness' of the C atoms corresponds to the range of displacement of the different C atoms estimated from the coherent fraction.

of Ru to Ag(111) is significantly weakened and the binding energy is closer to that of Ru-TPP not in direct contact with the metallic surface (physisorbed Ru-TPP: 281.0 eV). [159] Hence we can conclude that IMe ligates to the metal center of Ru-TPP, forming Ru(IMe)-TPP. This interpretation is supported by ab initio calculations, which, in agreement with the experimental value, predict a shift of 1 eV between Ru(IMe)-TPP/Ag(111) and Ru-TPP/Ag(111) for the Ru 3d$_{5/2}$ core level (see dotted lines in Figure 7.1G).

To also determine the out-of-plane structural implications of the ligation, which are not easily accessible by STM, NIXSW [43] measurements were performed. Figure 7.5A shows the absorption profile of the Ru 3d$_{5/2}$ core level for a Ru(IMe)-TPP/Ag(111) layer like the one depicted in Figure 7.1E. From fitting this spectrum, a coherent fraction, f_H, of 0.88 ± 0.09 and a coherent position, P_H, of 0.47 ± 0.04 were extracted. Compared to pristine Ru-TPP/Ag(111), the coherent fraction (Ru-TPP: 0.88 ± 0.05) does not change within the uncertainty, while the coherent position (Ru-TPP: 0.10 ± 0.02) increases significantly. [159] This indicates a very uniform alteration of the adsorption height, lifting the Ru atom by $\sim$0.9 Å from 2.59 ± 0.05 Å [159] to a height of 3.48 ± 0.10 Å above the Ag(111) surface. This electronic and geometric effect on the metal center has been described as 'surface *trans*-effect' and is reported upon ligation of gaseous, inorganic molecules onto silver supported porphyrins [154] and phthalocyanines, [136] albeit with less dramatic height differences.

The C 1s NIXSW data (Figure 7.5B) show a low coherent fraction of 0.18 ± 0.02 due to the nonplanarity of the porphyrin. [188] Nevertheless, the average adsorption height can be determined from the coherent position to be 3.50 ± 0.05 Å, $\sim$0.5 Å higher than for the pristine Ru-TPP/Ag(111). We note that the organic layer contained $\sim$15 % pristine Ru-TPP in the data, which can affect both the coherent fraction and position of the analyzed C 1s signal. However, the significant change in the coherent position shows clearly that not only the Ru center but also the entire macrocycle changes its geometry on the surface upon ligation. While the largest increase of the adsorption height is observed for the metal center,

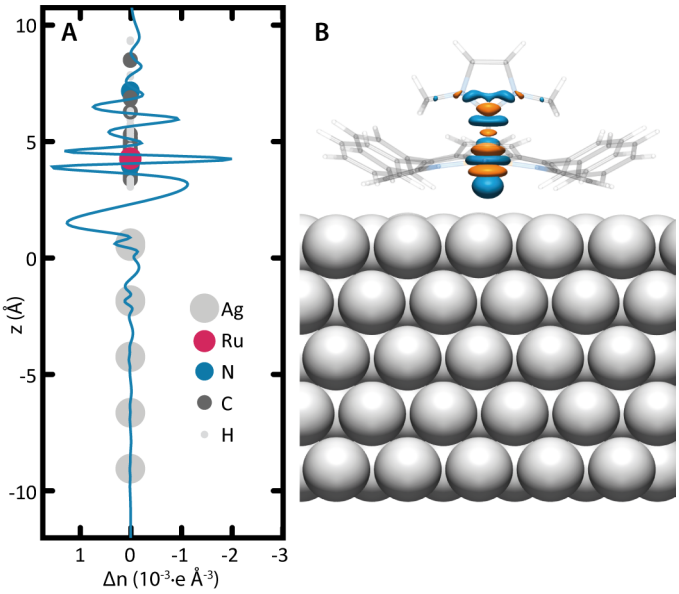

Figure 7.6 DFT results showing the electron transfer and molecular conformation upon NHC ligation on Ru-TPP/Ag(111). (A) One-dimensional charge redistribution plot shows the difference in electron density upon IMe adsorption normal to the Ag(111) surface. (B) Three-dimensional charge redistribution plot shows isosurfaces (0.04 e Å^{-3}) indicating gain (orange) and loss (blue) of electron density.

a displacement is observed for the entire molecule consistent with the findings of the surface *trans*-effect of Fe-phthalocyanine on the same surface. [136]

Finally, we used DFT simulations in order to gain insight into the complete structural conformation and electronic structure of the NHC binding on these pedestals. The DFT optimized structure of the IMe-ligated molecule reproduces the observed differences in the conformation of the molecule (Figure 7.1D, 7.6): the adsorption height of the Ru increases by 0.98 Å upon ligation of IMe (the detailed structural parameters from NIXSW and DFT are compared in Table 7.1). Having established the validity of our DFT calculations, we can confidently quantify further the bond length between Ru and the NHC as 1.99 Å, which is comparable to reported crystal structures of Ru(IMe)$_2$-porphyrins (2.08 Å). [187] The macrocycle preserves its saddle-shape at an average adsorption height of 3.56 Å, but the bending of α-pyr and κ-pyr is more symmetric (α: 20° & κ: 15°, respectively) compared to the pristine Ru-TPP (α: 28° & κ: 9°). By considering the adsorption height of the N atoms (3.51 Å) defining the plane for the macrocycle, the NHC-ligated Ru atom is displaced above it by 0.15 Å, in contrast to being located 0.19 Å below it in the absence of the axial ligand. [159]

Furthermore, an extensive redistribution of electron density normal to the surface is observed on the central part of the molecular complex, shown in Figure 7.6 by plotting the electron density differences upon IMe ligation. Electron depletion in the region just below the NHC indicates the expected σ-bonding involving the lone pair of the carbene. [189] Additionally, the depletion of electron density around the N in the NHC ligand and concomitant accumulation of density in the d_{xz} and d_{yz} orbitals of the Ru can be related to π-bonding [190] between the NHC and Ru center. From Bader analysis, a positive charge on the NHC of 0.26 e was extracted, elucidating the electron-donating properties of the NHC as well as a more positively charged Ru center (Δq = 0.25 e, Table 7.2). While the charge density on the

Table 7.1 NIXSW and DFT results for Ru(NHC)TPP/Ag(111) and Ru-TPP/Ag(111): Coherent fractions f_{111} and coherent positions P_{111} satisfying Bragg conditions from the (111) plane of the Ru and C signals, and adsorption heights extracted from DFT.

			Adsorption height (Å)	
	$\mathbf{f_{111}}$	$\mathbf{P_{111}}$	NIXSW	DFT
Ru-TPP on Ag(111)				
Ru $3d_{5/2}$	0.88 ± 0.05	0.10 ± 0.02	2.59 ± 0.05	2.68
C 1s	0.22 ± 0.03	0.28 ± 0.03	3.02 ± 0.07	3.20
Ru(NHC)-TPP on Ag(111)				
Ru $3d_{5/2}$	0.88 ± 0.09	0.47 ± 0.04	3.48 ± 0.10	3.66
C 1s	0.18 ± 0.02	0.48 ± 0.02	3.50 ± 0.05	3.56

Table 7.2 Bader charge analysis extracted from DFT, given in units of the elementary charge e. For the additional values mentioning 'without', the excluded part was not taken into consideration, but the geometry of the remaining part was fixed.

	Ru ion	TPP macrocycle	IMe
Ru-TPP gas-phase			
	1.04	-1.04	
Ru-TPP on Ag(111)			
	0.84	-1.49	
Ru(NHC)-TPP on Ag(111)			
	1.09	-1.49	0.26
without Ag(111)	1.09	-1.35	0.26
without IMe	0.96	-1.39	

TPP macrocycle remains the same, the negative charge donated by the NHC and the Ru ion is redistributed to the Ag(111)–Ru-TPP interface (Δq = 0.51 e).

Conclusion

In summary, we have functionalized selectively the Ru atoms in Ru-porphyrin layers on the (111) termination of silver with an NHC ligand and characterized them comprehensively by a variety of techniques. Structural analysis by experiment and theory showed a pronounced effect on the Ru-TPP upon NHC ligation, with a displacement of the Ru center of $\sim$0.9 Å away from the surface, an exemplary manifestation of the surface *trans*-effect. The bonding strength of the NHC to the silver-supported metalloporphyrin is estimated to be $\sim$1 eV by thermal desorption experiments. Within this layer, we demonstrated the controlled removal of individual NHCs within ordered arrays by STM manipulation and the ability to 'write' on the nanoscale. The NHC functionalization is a reversible process, and several cycles of adsorption and desorption can be performed on the same Ru-TPP layer.

Therefore, the metalloporphyrin is a suitable pedestal for guaranteeing both the in-plane as well as further out-of-plane assembly for practical applications. This well-defined model system is suitable for creating bottom-up nanoscale patterns and can be further addressed via STM tip manipulations on single molecules. Given that porphyrins self-assemble on a variety of surfaces including metal oxides, [191–193] graphite, [194] and BN, [129, 195] the proposed strategy is not limited to metal surfaces. Moreover, we anticipate that tailoring the

Ru porphyrin peripheral substituents will provide a route to templating axial NHCs in a wide range of preprogrammed arrangements. As NHCs are important catalytic species and can be further functionalized (e.g., photoswitches) [196] such layers pave the way for a versatile, modular, bottom-up assembly of functional pillars on surfaces.

8 N-heterocyclic carbenes: molecular porters of surface mounted Ru porphyrins

---

This Chapter includes content submitted for publication:

P. Knecht, J. Reichert, D. A. Duncan, M. Schwarz, J. T. Küchle, T.-L. Lee, P. S. Deimel, P. Feulner, F. Allegretti, W. Auwärter, G. Médard, A. P. Seitsonen, J. V. Barth, A. C. Papageorgiou, **N-Heterocyclic Carbenes: Molecular Porters of Surface Mounted Ru-Porphyrins**, *J. Am. Chem. Soc.*, unpublished work copyright 2021 American Chemical Society.

Single metal atoms on surfaces have attracted attention owing to the multitude of functional properties they comprehend spanning from catalysis [147] to magnetism. [197, 198] Ligating such metal atoms can both stabilize and tune their physicochemical properties. Cyclic tetrapyrrole compounds, for example, can stabilize undercoordinated metal atoms on surfaces, [106–108, 111] whereas coordination of axial ligands has produced surface rotors [185] and modified the atomic spin characteristics. [155, 199] N-heterocyclic carbenes (NHCs) are an interesting class of ligands that offer robust bonding and promising properties in surface functionalization. [33, 170, 171] Inspired by catalytically active porphyrin Ru-NHC compounds, [187] we used recently an NHC ligand to functionalize the Ru hosted in porphyrins on a silver surface (see Chapter 7, [166]). A modular construction of such interfaces worked remarkably well: the NHC was found to selectively ligate to the Ru centre of the pre-assembled porphyrins on Ag(111) without disrupting their self-assembly. Each Ru-porphyrin molecule served as pedestal for the precise surface orientation and packing of an NHC ligand. Diffraction measurements showed that the NHC functionalized Ru atoms uniformly moved by $0.9\,$Å away from the silver interface (illustrated in Figure 8.1A). Further investigations of this system illuminated an apparent paradox, which we report here: the assembly of the same NHC on the same Ru porphyrins, albeit in a different pre-assembled form, on the same surface following the same procedure resulted in a non-uniform adsorption height of the NHC ligated Ru (illustrated in Figure 8.1B). To elucidate this phenomenon observed by normal incidence X-ray standing waves (NIXSW), [159] we employed a methodology including structural determination with real and reciprocal space imaging as well as thermal desorption experiments. Thereby we reveal an NHC induced dynamic rearrangement of the molecular film in two layers. We functionalized a saturated monolayer of Ru tetraphenyl porphyrin (Ru-TPP) molecules on Ag(111), assembling in a compressed phase, [159] with the NHC 1,3-dimethyl-2*H*-imidazol-1-ium-2-ide (IMe) at room temperature (RT). The Ru 3d core level of Ru-TPP/Ag(111) has a characteristic energy shift by $1.2\,$eV after the IMe ligation (Figure

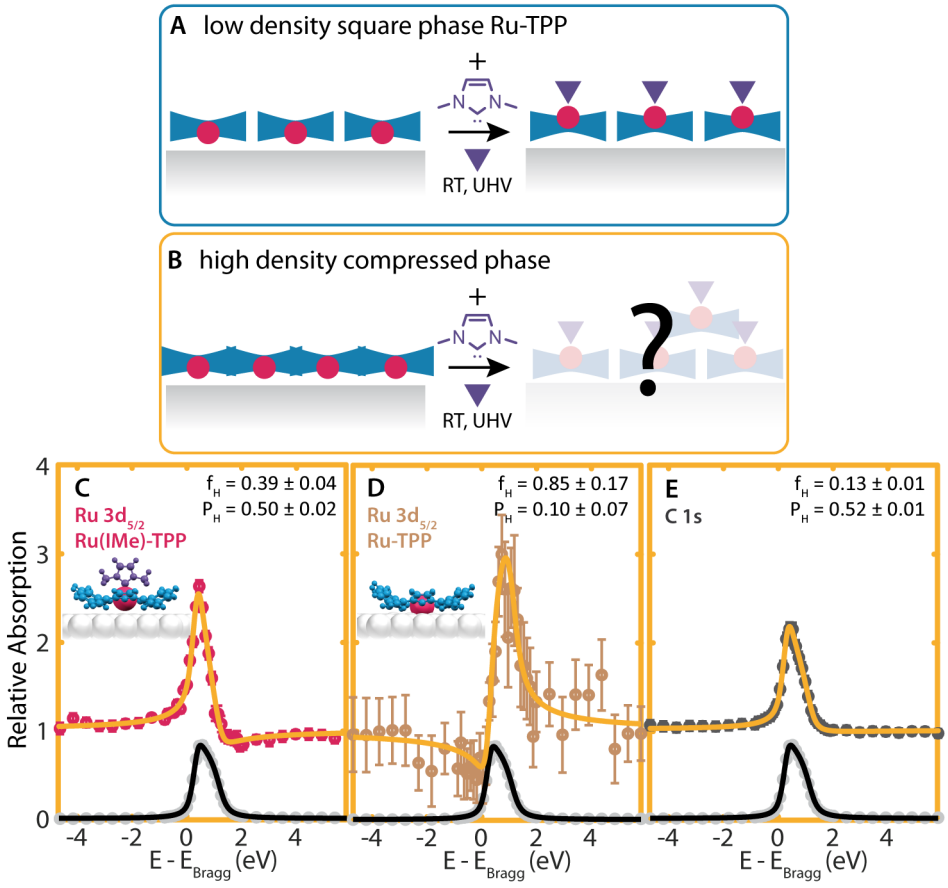

Figure 8.1 (A,B) Schematic of the effects of IMe ligation on different layers of Ru-TPP/Ag(111). In the square phase (A), the TPP self-assembly is retained, the Ru centers are displaced further from the Ag interface. In the compressed phase (B), a uniform displacement of the Ru centers is not compatible with the NIXSW data. (C-E): NIXSW absorption profiles following IMe ligated functionalization of the compressed phase on Ag(111), of the Ru $3d_{5/2}$ core level from Ru(IMe)-TPP (C) and Ru-TPP (D), and of the C 1s core level (E) . The yellow curves show the fits to the data, light grey dots and black curves indicate the reflection of the silver substrate data points and fit, respectively. Density functional theory (DFT) models of Ru(IMe)-TPP and Ru-TPP on the Ag(111) surface are shown as insets.

8.2B). This allows us to perform NIXSW of the Ru in the different environments to deduce the respective adsorption height from the surface. Analysis of the Ru $3d_{5/2}$ of the IMe ligated Ru (Figure 8.1C) in this saturated layer of Ru-TPP on Ag(111) gives a coherent position P_H = 0.50 $\pm$ 0.02 and a coherent fraction f_H = 0.39 $\pm$ 0.04. The coherent position, which can be used to deduce the adsorption height of the IMe ligated Ru, increased significantly upon ligation, similarly to our recently reported results on the less densely packed square phase of Ru(IMe)-TPP on Ag(111). [166] However the significant drop in the coherent fraction (from f_H = 0.88 $\pm$ 0.09) is not compatible with a single adsorption height for the Ru centre and consequently not compatible with a uniform conformational change of each molecule as observed for the square phase ligation (see Chapters 5 and 7, [159, 166]).

To attribute the drop of the coherent fraction solely to IMe ligation and not to a potential variation in the adsorption height of the Ru-TPP molecules on Ag(111) in the compressed phase, we simultaneously monitored the small fraction of uncapped Ru-TPP molecules in the same layer. The respective Ru $3d_{5/2}$ was found to have P_H = 0.10 $\pm$ 0.07 and f_H = 0.85 $\pm$ 0.17 (Figure 8.1D), in agreement with the values obtained for the compressed phase Ru-TPP/Ag(111) (Chapter 5, [159]). Therefore all the uncapped Ru atoms in this layer have an adsorption

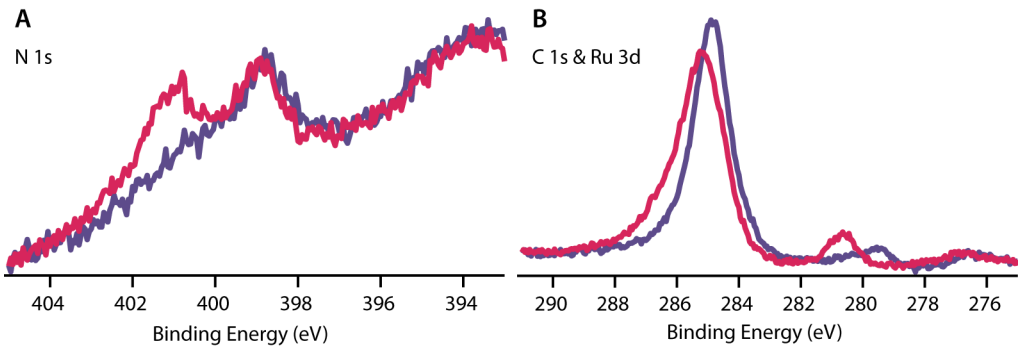

Figure 8.2 XP spectra of pristine Ru-TPP in the compressed phase (purple) and the same surface following IMe ligation at RT (red). (A) N 1s spectra. Upon IMe ligation, a second peak related to IMe (E_B = 401.1 eV) can be observed, while the first component related to Ru-TPP (E_B = 399.0 eV) does not change. (B) C 1s & Ru 3d spectra, showing the shift of the Ru $3d_{5/2}$ peak from 279.4 eV (Ru-TPP) to 280.6 eV (Ru(IMe)-TPP) upon ligation, as well as a change in the shape of the carbon peak.

height of 2.59 ± 0.17 Å, identical to both the compressed phase of Ru-TPP/Ag(111) and the less dense square phase. [159] This puzzling effect cannot stem from either the nature of the NHC–Ru-TPP ligation (we identified a well-defined adsorption height for the square phase Ru(IMe)-TPP) or from the change of the initial position of Ru (in both self-assembled structures Ru was found to have the same well-defined adsorption height). To understand it, we investigated the self-assembly with scanning tunneling microscopy (STM) and low-energy electron diffration (LEED). While STM offers a unique way of visualizing the self-assembly in real space, thus being sensitive to deviations from regularity, LEED facilitates the easier recognition of even minute changes in the periodic arrangement.

The LEED pattern of the compressed phase before IMe ligation is shown in Figure 8.3A, with one of the six equivalent unit cells highlighted. The inset shows the characteristic simulated pattern based on an overlayer matrix of $\begin{pmatrix} 4 & 5 \\ 3 & -13/6 \end{pmatrix}$ [159] for comparison with the experimental observation. The corresponding overview STM image (Figure 8.3D) shows the Ag(111) surface covered with Ru-TPP, where each protrusion signifies a single Ru-TPP molecule. A grid matching the expected periodicity from LEED is overlaid on the top left corner. After depositing IMe at RT on this monolayer, we observe marked differences (Figure 8.3B). The LEED pattern undergoes a transformation, which can be identified as the pattern of the sparser square phase, described by the overlayer matrix $\begin{pmatrix} 11/2 & 3/2 \\ 3/2 & 11/2 \end{pmatrix}$. The transformation of the contact layer to the square phase can be confirmed in the real space imaging (Figure 8.3E), which is highlighted on the top left corner by the overlaid grid marking the molecular density. Here the vast majority of Ru-TPP molecules are ligated to IMe and can be identified as the brighter protrusions of the same plane (see Chapter 7, [166]).

This increased sparsity indicates that a fraction of $\sim 20\,\%$ of the initially adsorbed Ru-TPP molecules are missing from the Ag(111) interface. Strikingly, the phase transformation is reversible: after annealing the IMe ligated Ru-TPP to a temperature, which entails desorption of IMe (cf. temperature programmed desorption (TPD) investigation below), the LEED and STM data show that the initial compressed phase is restored (Figure 8.3C,F). Desorption of the missing Ru(IMe)-TPP molecules can therefore be ruled out, as also shown by X-ray photo-

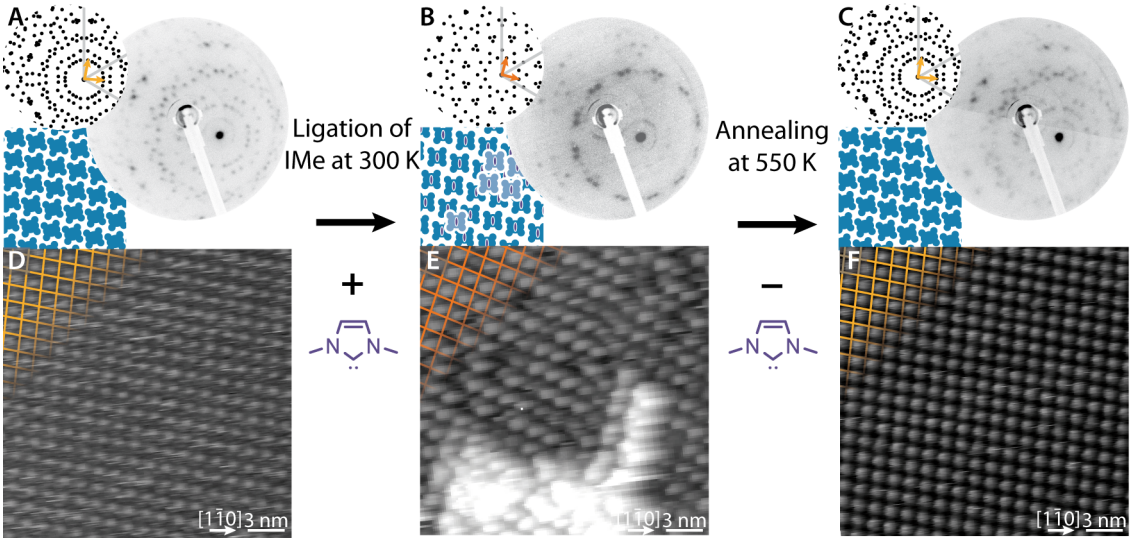

Figure 8.3 Porter effect of IMe monitored by LEED and STM. (A,D) Ru-TPP on Ag(111) self-assembled in the compressed phase. (B,E) The same sample following deposition of IMe shows a diffraction pattern matching the square phase Ru(IMe)-TPP, the STM image confirms the phase change and indicates an accumulation of molecules in a second layer. (C,F) After annealing the surface imaged in B/E to 550 K, the compressed phase LEED pattern observed in A is restored. All LEED images were taken at 300 K, the simulated diffraction patterns of each phase are plotted next to the LEED image by black dots, the high symmetry axes of the substrate are indicated in gray, the unit cell vectors of a single domain are shown in yellow (A,C) and orange (B). Below the diffraction patterns, a schematic, top view representation of the corresponding real-space arrangements of the Ru-TPP (blue shapes) and IMe ligands (purple ellipses) are shown. STM images were taken at 0.6 V, 90 pA, 300 K (A), -2.1 V, 50 pA, 110 K (B), 1.25 V, 60 pA, 280 K (C), the overlaid grids highlight the self-assembly.

electron spectroscopy (XPS) measurements (Figure 8.2). For this transformation, manifestly, the NHCs (depicted schematically as purple ellipses in Figure 8.3B) act as molecular porters that carry $\sim$20 % of the Ru-TPP molecules (depicted in blue) from the silver contact layer to a second layer on top. Such relocation is also evident in the STM images (Figure 8.3E). Small molecular adlayers on top of the first layer can be identified, where protrusions similar to the regular underlying structure can be discriminated. Such adlayers cannot be visualized by STM investigations at RT, presumably due to increased mobility.

The second layer created by the porter effect contributes to the NIXSW with a different adsorption height for both the C 1s and the Ru $3d_{5/2}$. This has a more pronounced effect on the Ru $3d_{5/2}$ spectra (Figure 8.1C). Indeed, a small contribution of the second layer Ru centers is sufficient to lower the coherent fraction significantly, owing to the interference of the emitted electrons from the two different adsorption heights. The coherent position of 0.50 ± 0.02 (Figure 8.1C) would correspond to an adsorption height of 3.53 ± 0.05 Å in the case of a single adsorption site. However, with two different adsorption heights, it is not possible to determine the two different adsorption heights precisely. The measured coherent position and the transformation to the square phase self-assembly suggest that the adsorption height of the Ru atoms of the molecules at the Ag(111) interface is comparable to the 3.48 ± 0.10 Å measured for square phase Ru(NHC)-TPP on Ag(111) (see Chapter 7, [166]), with a respective structural *trans*-effect resulting in a displacement of approximately 0.9 Å away from the surface.

While the portering also influences the absorption profiles of the C 1s core levels (Figure 8.1E), the effect is less dramatic due to the non-planarity of the porphyrin macrocycle. The co-

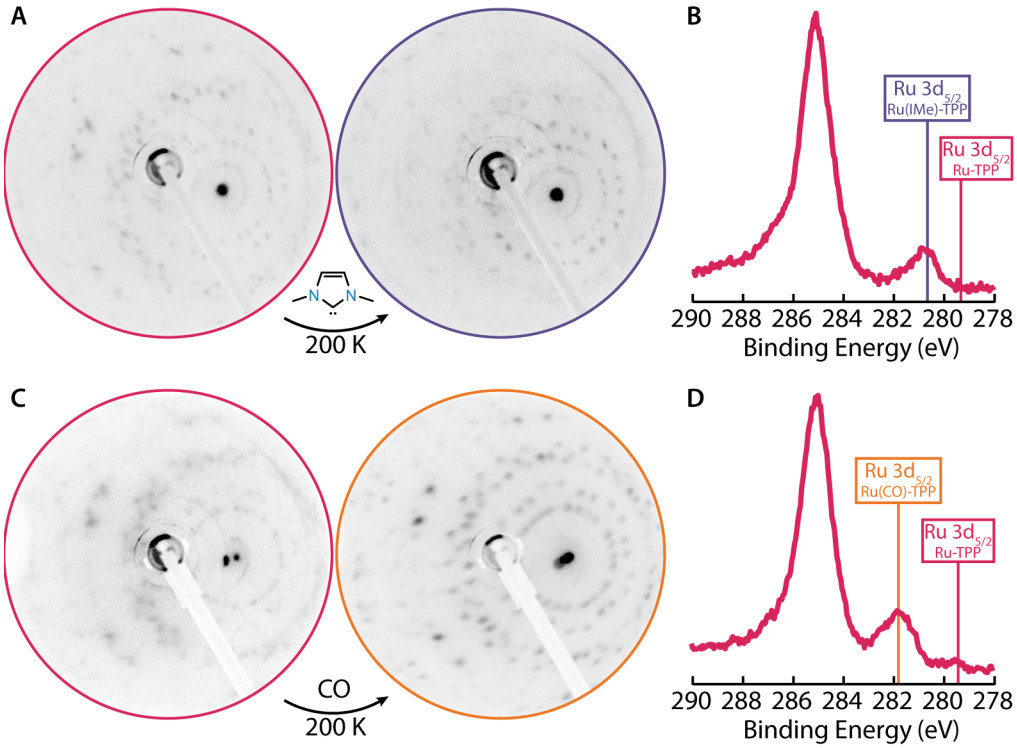

Figure 8.4 (A) LEED of compressed phase Ru-TPP (left) and of Ru(IMe)-TPP after IMe ligation at 200 K (right). (B) XP spectrum of the Ru 3d region for Ru(IMe)-TPP after IMe ligation at 200 K. The shift in binding energy of the Ru $3d_{5/2}$ peak (purple marker) compared to pristine Ru-TPP (pink marker) shows that IMe ligated to the Ru-TPP molecules. (C) LEED of compressed phase Ru-TPP (left) and of Ru(CO)-TPP after CO ligation at 200 K (right). (D) XP spectrum of the Ru 3d region for Ru(CO)-TPP after CO ligation at 200 K. The shift in binding energy of the Ru $3d_{5/2}$ peak for the Ru(CO)-TPP (orange marker, E_B = 281.8 eV) compared to pristine Ru-TPP (pink marker) shows that CO ligated to the Ru-TPP molecules.

herent position increases significantly from 0.29 ± 0.02 (see Chapter 5, [159]) to 0.52 ± 0.01 upon ligation, indicating that not only the Ru center is experiencing the *trans*-effect, but that the whole porphyrin macrocycle changes its shape, akin to the submonolayer coverages of Ru(NHC)-TPP on Ag(111) (see Chapter 7, [166]). The coherent fraction is already very low for the pristine Ru-TPP layer (0.16 ± 0.02), [159] showing that the carbon atoms occupy multiple different adsorption heights and reduces further (0.13 ± 0.01) after IMe ligation, supporting the transfer of the complete molecule on the second layer.

The mass transport induced by the portering of entire molecules is reminiscent of the removal of single metal atoms from the close-packed coinage metal surfaces by the same NHC. [61, 63, 180] However, to the best of our knowledge, this is the first report of molecules being carried from the metal surface to the next layer. We attribute the physical origin of this phenomenon to the relative adsorption strength of Ru-TPP and Ru(IMe)-TPP on Ag(111). Indeed, IMe weakens the bond of Ru-TPP to the Ag surface resulting in a so-called *trans*-effect, while the driving force for the formation of the compressed phase also ceases. [159]

The *trans*-effect is documented upon ligation of several inorganic molecules on metalloporphyrins and phthalocyanines. In particular, a substantial structural *trans*-effect is observed on the Ru-TPP/Ag(111) upon CO ligation: the Ru atoms are displaced 0.6 Å further away from the Ag interface (see Chapter 6). It is, in contrast, notable that such a porter effect cannot be observed on the corresponding LEED experiment when CO replaces IMe (Figure 8.4C,D), in

an experiment albeit performed at a 100 K lower temperature required by the lower desorption energy of CO. To investigate thermal effects on the observed phase transformation, IMe was also deposited on the compressed Ru-TPP phase at 200 K. By monitoring the binding energy of the Ru $3d_{5/2}$ region in XPS, we could confirm the formation of a Ru(IMe)-TPP layer, but no difference was identified in the respective LEED pattern (Figure 8.4A,B). Thereby, we can conclude that the porter effect is hitherto particular to IMe and thermally assisted. We therefore investigated the dynamics of IMe to the Ru-TPP compressed phase on Ag(111) with TPD experiments.

Figure 8.5A shows the TPD spectra after the deposition of IMe at 200 K on Ru-TPP in the compressed phase. While at low initial IMe coverages (θ_0) the apex of the desorption peak is located at ∼350 K, it is shifted towards lower temperature with increasing coverages of IMe. Gratifyingly, with the assumption of repulsive interactions between adsorbates, this effect could be modeled with an equation featuring decreasing desorption energy for increasing coverage, based on the Polanyi-Wigner equation in the following form:

$$\frac{d\theta}{dT} = \frac{\nu}{\beta} \cdot \theta \cdot \exp\left(-\frac{E_{des} - E_\theta \cdot \theta}{k_B T}\right) \tag{8.1}$$

The best fitting results (Figure 8.5A) were obtained with a frequency factor $\nu = 1.04 \times 10^{15}\,\mathrm{s}^{-1}$, which falls into the range of common frequency factors reported for desorption of organic molecules, [200–203] and a desorption energy of $E_{des} = (1.08 - 0.12 \cdot \theta)$ eV. We propose that the repulsion is caused by dipole-dipole interactions [204–206] between adjacent IMe ligands. Importantly, the reduction of 0.12 eV could be reproduced by a dipole moment of ∼6 D, using a simple model on the basis of Coulomb-interactions between dipoles (see Chapter 3, with q = 0.3 e from DFT, estimating l = 4 Å as separation of IMe and the TPP macrocycle, s = 6 Å as two times the Ag(111)/Ru-TPP separation), in very good agreement with DFT, from which we estimate this dipole at 5.3 D. Since substantial molecular dipoles are also evident using DFT for a range of NHCs adsorbed directly on a metal surface and further evidenced in work function measurements, [207, 208] it would be expected for such interactions to influence the thermal stability of NHC self-assembled monolayers. From our analysis, the determined desorption energy of IMe from Ru-TPP/Ag(111) ranges between 0.96 eV (all Ru centres covered) and 1.08 eV (zero coverage limit). These energies are consistent with the earliest reported data (Chapter 7, [166]) by computation with the same frequency factor $\nu = 1.04 \times 10^{15}\,\mathrm{s}^{-1}$.

With the onset of desorption already at ∼270 K for high coverages, the ligation on the compressed phase should not be stable at 300 K. Surprisingly, complete NHC functionalization of the Ru centers was however achieved at 300 K. TPD spectra of IMe deposited at 300 K are shown in Figure 8.5B. While at low IMe coverages, the main peaks are comparable to the desorption spectra shown in Figure 8.5A, there is an additional component at ∼400 K. This component is not observed in either the TPD of the compressed phase after exposure to IMe at 200 K, nor the square phase after exposure to IMe at 300 K. [166] It is therefore reasonable to assign this component to IMe desorption from the transported Ru-TPP molecules and to the reintegration of those Ru-TPP molecules back into the compressed phase.

In conclusion, we have discovered a fascinating, dynamic interface rearrangement based

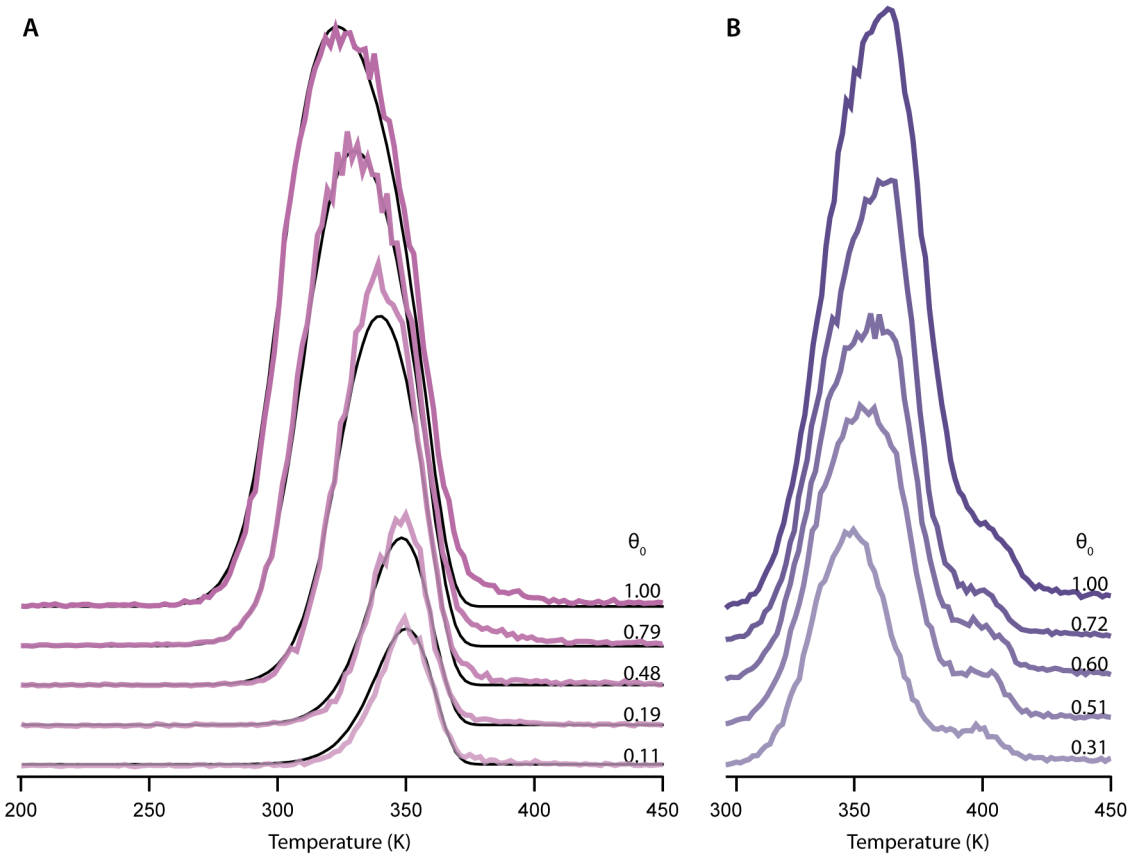

Figure 8.5 TPD spectra of IMe on Ru-TPP (m/z = 96, corresponding to the parent ion of IMe). Each graph shows spectra for different initial coverages of IMe, θ_0, up to a saturation of all Ru-TPP molecules ($\theta_0 = 1$). The spectra are offset along the vertical axes for clarity. A: IMe (T_{sample} = 200 K during sublimation) on a compressed layer Ru-TPP, the black lines show the fit. B: IMe (T_{sample} = 300 K during sublimation) on a compressed layer Ru-TPP.

on the NHC ligand acting as a molecular porter for Ru-TPP molecules on Ag(111). Ru(NHC)-TPP complexes were lifted into a second layer to allow a phase transformation of the first layer from a compressed phase into the less densely packed square phase. This mass transport is thermally activated and specific for the NHC ligand, which leads to weakened bonding of the ruthenium atom to the silver surface. Remarkably, this reorganization is thermally reversible by annealing-promoted removal of the NHC ligands. Detailed analysis of the thermal desorption reveals the effect of repulsive dipole interactions in the binding energy of NHCs on surfaces, and similar modeling is expected to be applicable in the characterization of densely packed NHCs. We anticipate that harnessing these dynamic events is at hand and will serve the engineering of atomically precise NHC-containing complex interfaces.

9 Conclusions and outlook

In this thesis an investigation of the properties of different (metal-)organic molecules on a metal substrate is conducted. Specifically, we characterized the self-assembly of the molecules on the substrate, observed in-plane coordination with transition metals, and induced out-of-plane complexation with organic and inorganic ligands. A combined approach of different analysis techniques including scanning probe microscopy, photoelectron spectroscopy, electron diffraction, and desorption spectroscopy, supported by complementary DFT calculations, forms the basis for a comprehensive analysis of the geometric, electronic and chemical properties of the investigated systems.

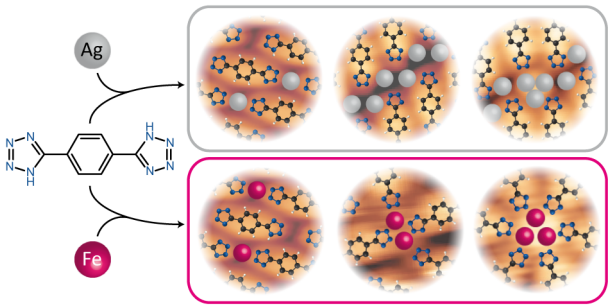

In Chapter 4, the self-assembly and metal adatom coordination of the organic ligand BTB on a Ag(111) surface was investigated via STM and XPS. Already at RT simultaneous deprotonation and coordination with native silver adatoms of the tetrazole moieties occur slowly, evidenced via XPS. This process can be sped up by thermal annealing, which for temperatures higher than $\sim$390 K leads also to the formation of different metal-atom coordinated structures, both with the native silver adatoms and with additionally deposited iron adatoms. The multitude of coordination sites offered by the tetrazole moieties is reflected in a polymorphism of the metal adatom coordination motifs found on the surface. Four different motifs were found after annealing, two incorporating silver adatoms and two incorporating iron adatoms (see Figure). We have seen nodes of silver/iron trimers, dimers and single adatoms. Furthermore, the XPS signature of the iron atoms points towards a Fe^{2+} species, implying that the ligation prevents interfacial charge transfer, which often lowers the observed oxidation state and quenches magnetic properties.

Further experiments could verify if the iron atoms have magnetic properties, determine its spin state and investigate possible SCO phenomena. Additionally, the ligation behavior with different metal adatoms could shed light to the driving force for the polymorphism of the coordination motifs and the role of each of the four coordination sites of the tetrazole moiety further.

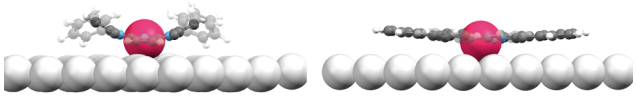

Chapter 5 is based on a detailed analysis of the self-assembly of Ru-TPP on Ag(111). This porphyrin can

self-assemble in two different ways on the chosen substrate, which can be controlled by the amount of molecules deposited on the surface. In the submonolayer regime, the self-assembly is very similar to other porphyrins, however by combining STM, LEED, NIXSW, and ab initio calculations by DFT we were able to determine an asymmetry. This asymmetry offsets half of the molecules in such a way, that all Ru centers can be accommodated into hollow sites of the Ag(111) substrate, indicating a strong bonding between the Ru and the Ag(111) surface. For saturated monolayers, the pattern of the self-assembly changes surprisingly into a more densely packed phase, allowing to accommodate $\sim$20 % more molecules to the Ag contact layer. Here, we do not observe any asymmetries in the self-assembly, and the moiré observed in STM images points towards a higher-order coincidence lattice, in agreement with the LEED measurements. Moreover, the saddle-shape conformation of the Ru-TPP was confirmed, evident in STM by protrusions caused by the opposite upwards bended pyrroles, and from NIXSW data, showing that the four nitrogen atoms in the macrocycle do not have the same adsorption height. In addition, the adsorption height of the Ru center was the same for both self-assemblies, placing it below the porphyrin macrocycle and close to the Ag(111) surface. The third structure under investigation was a more disordered phase, which formed after a thermal annealing, inducing cyclodehydrogenation reactions in the porphyrins and leading to the formation of four different derivatives of Ru-TPP. AFM, NIXSW and DFT data showed a significant planarization of the molecule, resulting in a bowl-shaped macrocycle, with the central Ru atom even closer to the surface than for the pristine Ru-TPP. A strong preference for the Ag(111) hollow sites for the adsorption for the Ru center points once more towards a strong interaction between the Ru center and the Ag(111) substrate.

While this chapter offers a profound insight into the adsorption behavior of Ru-TPP onto the Ag(111) surface, further studies could enlighten the influence of the Ru-TPP moieties on these fascinating properties. Different substituents on the porphyrin macrocycle could influence the compression effect on the porphyrin, and similar effects might be found with other metalloporphyrins.

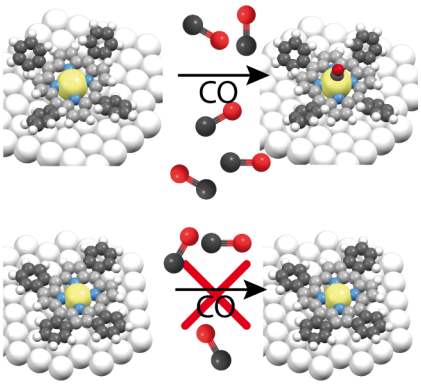

In Chapter 6, we use a submonolayer of Ru-TPP on Ag(111) as pedestals for the ligation of CO to the ruthenium center. We found that the CO can bind to the Ru-TPP in different ways, namely the μ-mono- or *cis*-μ-dicarbonyl ligation, where the CO bridges between a pyrrole group and the metal center, and axial ligation, with the CO bonding directly to the metal center. The μ-carbonyl bonds are stable only at low temperatures, while the axial ligation exhibits a significantly stronger binding, leading to a much higher temperature stability, which is characterized by XPS, TPD, NIXSW and STM with additional support from DFT calculations. We find a significant surface-*trans* effect upon ligation, albeit a bit less pronounced compared to the NHC ligation.

A very interesting finding is the significant difference in the ligation behavior depending of

the conformation of the macrocycle, whether it is in the saddle-shape configuration (pristine Ru-TPP) or in the bowl-shape configuration (planarised Ru-TPP derivatives). While we have observed both axial and cis-dicarbonyl ligation on Ru-TPP, none of these were found for the bowl-shaped macrocycle of the Ru-TPP_{pl}, despite the similarity in the chemical environment of the ruthenium center. We ascribe this behavior to a weaker bond between the ruthenium and the CO, which is confirmed by DFT, and to potential differences to the CO sticking coefficient.

This system could be used as a gas sensing system for CO and potentially other small organic molecules, given that we found the adsorption and desorption to be a fully reversible process. However, the bond is only stable below RT. This issue should be addressed in further studies, where a less interacting substrate might increase the thermal stability.

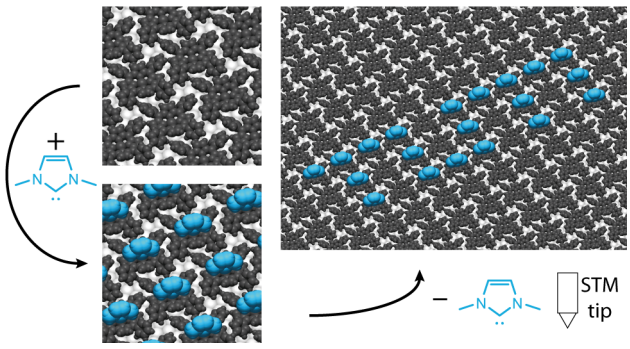

Chapter 7 is based on the same pedestal consisting of Ru-TPP on the Ag(111) surface, but covers the controlled tethering of IMe. We were able to apply the ligand at RT, inducing a ligation to the Ru center, evidenced by XPS measurements. Furthermore NIXSW data showed that this ligation alters the conformation of the Ru-TPP, with the Ru center being lifted away from the surface by almost 1 Å, which can be interpreted as a strong surface *trans*-effect, in line with TPD data showing a rather large desorption energy for the ligand, also reflected in its temperature stability. Utilizing a LT-STM we could address single ligands with the STM tip, enabling the precise removal of single IMe molecules, which opens up the path to nanoprinting, with a resolution of $\sim 2 \times 10^7$ dpi determined by the underlying Ru-TPP lattice. We also show a way for the precise placement of NHCs on a surface, with a well-defined orientation and spacing. This strategy will enable to further harness NHC chemistry for surface functionalization.

The various possibilities for the tailoring of NHCs to fit specific purposes offer a multitude of options for subsequent studies. Bulkier NHC ligands might improve the temperature stability of this ligand even further, which would be beneficial for the purpose of nanoprinting, as well as a smaller pedestal than Ru-TPP to further enhance the resolution. Further investigations should also inspect potential ligation induced switching of magnetic properties of the Ru center, as observed for Co-TPP on Au(111). [155, 209, 210] Bis-NHCs ligands could pave the way towards surface mounted 3D coordination networks.

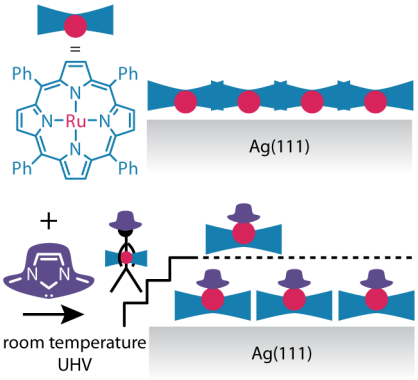

Chapter 8 covers a fascinating dynamic effect, observed on the more densely packed compressed phase of Ru-TPP on Ag(111). While we demonstrated in the previous chapter that the ligation of IMe on the less densely packed Ru-TPP phase is of a very controllable and uniform character, we could show that the ligation on the compressed phase induces a reorganization of the Ru-TPP layer. Upon IMe ligation on the compressed phase Ru-TPP we found $\sim$20 % of the molecules portered into a second layer on top and a restoration of the less densely packed phase of Ru-TPP in the contact layer by using LEED, STM, and NIXSW. This process is reversible by thermal desorption of the IMe ligands. We noticed however that this dynamic effect is specific to the IMe ligand and thermally assisted, as it is only observed upon IMe ligation at RT, and could not be observed for either CO or IMe ligation at 200 K.

Another interesting finding was that after IMe deposition at 200 K, the desorption energy increased with decreasing IMe coverage. This could be explained by repulsive interactions, caused by IMe induced dipole moments.

Further experiments with different NHC ligands might improve our understanding of the driving force for this dynamic effect, as well as the influence of molecular dipoles on the ligation characteristics. To this end, it could also be beneficial to compare the repulsive interactions on the two different self-assemblies of Ru-TPP, as the different packing density should result in different interaction strength between the dipoles.

To conclude, this thesis provides fundamental insights in using functional organic ligands to stabilize transition metal atoms and clusters on surfaces. We explored on an atomistic scale how single atoms and clusters of Ag and Fe on a surface are stabilized by a tetrazole linker. While in this case a single ligand lead to a variety of possible metal nodes, we subsequently focused on a different case, where a single node, Ru-TPP, could be stabilized in different ways on the surface. We have shown that the understanding of such metalloporphyrin/metal interfaces is crucial e.g. for assessing the chemical properties towards ligation or for the creation of patterns on the nanoscale. For both employed ligands, CO and IMe, we observed different reactivities towards the metal center upon slightly changing the environment. This elucidates the importance of the assembly in such molecular layers and the necessity to explore the chemistry beyond the single-molecule level. Such detailed studies, elaborating on the impact of both the metal atoms and the molecular modules are expected to improve the understanding of the chemistry of surface-confined metal-organic systems and pave the way for the further application of such surfaces, e.g. for single-site catalysis, gas storage and release systems, information storage devices or in the field of nanoprinting. The results from the model systems analyzed in this thesis, by an extensive experimental and theoretical approach, are expected to offer valuable insights for the further development of the field of sophisticated functional metal-organic interfaces.

List of publications

- The self-assembly and metal adatom coordination of a linear bis-tetrazole ligand on Ag(111)
  P. Knecht, N. Suryadevara, B. Zhang, J. Reichert, M. Ruben, J. V. Barth, S. Klyatskaya, and A. C. Papageorgiou
  Chemical Communications, vol. 54, no. 72, pp. 10072-10075, 2018

- On-surface Synthesis of a Semiconducting 2D Metal-Organic Framework $Cu_3(C_6O_6)$ Exhibiting Dispersive Electronic Bands
  R. Zhang, J. Liu, Y. Gao, M. Hua, B. Xia, **P. Knecht**, A. C. Papageorgiou, J. Reichert, J. V. Barth, H. Xu, L. Huang, N. Lin
  Angewandte Chemie, International Edition, vol. 59, no. 7, pp. 2669-2673, 2020.

- Tunable Interface of Ruthenium Porphyrins and Silver
  P. Knecht, P. T. P. Ryan, D. A. Duncan, L. Jiang, J. Reichert, P. S. Deimel, F. Haag, J. T. Küchle, F. Allegretti, M. Schwarz, M. Garnica, W. Auwärter, A. P. Seitsonen, J. V. Barth, and A. C. Papageorgiou
  Journal of Physical Chemistry C, vol. 125, no. 5, pp. 3215-3224, 2021.

- Assembly and Manipulation of a Prototypical N-Heterocyclic Carbene with a Metalloporphyrin Pedestal on a Solid Surface
  P. Knecht, B. Zhang, J. Reichert, D. A. Duncan, M. Schwarz, F. Haag, P. T. P. Ryan, T.-L. Lee, P. S. Deimel, P. Feulner, F. Allegretti, W. Auwärter, G. Médard, A. P. Seitsonen, J. V. Barth, and A. C. Papageorgiou
  Journal of the American Chemical Society, vol. 143, no. 11, pp. 4433-4439, 2021.

- Conformational control of chemical reactivity for surface-confined Ru-porphyrins
  P. Knecht, J. Reichert, P. S. Deimel, P. Feulner, F. Haag, F. Allegretti, M. Garnica, M. Schwarz, W. Auwärter, P. T. P. Ryan, T.-L. Lee, D. A. Duncan, A. P. Seitsonen, J. V. Barth, and A. C. Papageorgiou
  Angewandte Chemie, International Edition, doi.org/10.1002/anie.202104075, 2021.

- N-Heterocyclic Carbenes: Molecular Porters of Surface Mounted Ru-Porphyrins
  P. Knecht, J. Reichert, D. A. Duncan, M. Schwarz, J. T. Küchle, T.-L. Lee, P. S. Deimel, P. Feulner, F. Allegretti, W. Auwärter, G. Médard, A. P. Seitsonen, J. V. Barth, and A. C. Papageorgiou
  submitted.

- An enantiospecific self-assembled array of molecular raffle wheels: The rotation of organic modules confined in the pores of a surface-supported kagome network
  D. Meier,* A. K. Adak,* **P. Knecht**,* J. Reichert, S. Mondal, N. Suryadevara, K. S. Kumar, K. Eguchi, F. Allegretti, M. Ruben, J. V. Barth, S. Narasimhan, and A. C. Papageorgiou
  (* equal contribution)
  submitted.

- Monodispersed graphene nanoribbons on Ag(111) by electrospray controlled ion beam deposition: their self-assembly and on-surface extension
  W. Ran, A. Walz, K. Stoiber, **P. Knecht**, H. Xu, A. C. Papageorgiou, A. Hüttig, D. Cortizo-Lacalle, J. P. Mora-Fuentes, A. Mateo-Alonso, H. Schlichting, J. Reichert, and J. V. Barth
  in preparation.

- Flexible on-surface self-assembly: Phase transformation in the long-range ordering of a bio-inspired macrocyclic compound on Ag(111)
  F. Haag, P. S. Deimel, **P. Knecht**, R. Lauenstein, M. Kaspar, K. Seufert, M. González Cuxart, Y. Bao, A. C. Papageorgiou, P. Feulner, W. Auwärter, C. R. Hess, J. V. Barth, and F. Allegretti
  in preparation.

Bibliography

[1] H. Iwai, “End of the Downsizing and World after that”, in 2017 Fourth International Conference on Mathematics and Computers in Sciences and in Industry (MCSI), edited by IEEE Computer Society (2018), pp. 138–143.

[2] B. Marchon, T. Pitchford, Y.-T. Hsia, and S. Gangopadhyay, “The Head-Disk Interface Roadmap to an Areal Density of Tbit/in^2”, Adv. Tribol. **2013**, 1–8 (2013).

[3] M. L. Perrin, E. Burzurí, and H. S. J. van der Zant, “Single-molecule transistors”, Chem. Soc. Rev. **44**, 902–919 (2015).

[4] W. Auwärter, K. Seufert, F. Bischoff, D. Écija, S. Vijayaraghavan, S. Joshi, F. Klappenberger, N. Samudrala, and J. V. Barth, “A surface-anchored molecular four-level conductance switch based on single proton transfer”, Nat. Nanotechnol. **7**, 41–46 (2011).

[5] P. Liljeroth, J. Repp, and G. Meyer, “Current-Induced Hydrogen Tautomerization and Conductance Switching of Naphthalocyanine Molecules”, Science **317**, 1203–1206 (2007).

[6] G. J. Simpson, V. García-López, P. Petermeier, L. Grill, and J. M. Tour, “How to build and race a fast nanocar”, Nat. Nanotechnol. **12**, 604–606 (2017).

[7] C. Joachim and J. K. Gimzewski, “A nanoscale single-molecule amplifier and its consequences”, Proc. IEEE **86**, 184–190 (1998).

[8] S. Erbas-Cakmak, S. Kolemen, A. C. Sedgwick, T. Gunnlaugsson, T. D. James, J. Yoon, and E. U. Akkaya, “Molecular logic gates: the past, present and future”, Chem. Soc. Rev. **47**, 2228–2248 (2018).

[9] M. Mannini, F. Pineider, P. Sainctavit, C. Danieli, E. Otero, C. Sciancalepore, A. M. Talarico, M.-A. Arrio, A. Cornia, D. Gatteschi, and R. Sessoli, “Magnetic memory of a single-molecule quantum magnet wired to a gold surface”, Nat. Mater. **8**, 194–197 (2009).

[10] G. E. Poirier, “Coverage-Dependent Phases and Phase Stability of Decanethiol on Au(111)”, Langmuir **15**, 1167–1175 (1999).

[11] M. Ruben, D. Payer, A. Landa, A. Comisso, C. Gattinoni, N. Lin, J.-P. Collin, J.-P. Sauvage, A. de Vita, and K. Kern, “2D supramolecular assemblies of benzene-1,3,5-triyl-tribenzoic acid: temperature-induced phase transformations and hierarchical organization with macrocyclic molecules”, J. Am. Chem. Soc. **128**, 15644–15651 (2006).

[12] M. S. Baviloliaei and L. Diekhöner, “Molecular self-assembly at nanometer scale modulated surfaces: trimesic acid on Ag(111), Cu(111) and Ag/Cu(111)”, Phys. Chem. Chem. Phys. **16**, 11265–11269 (2014).

[13] H. Aitchison, H. Lu, R. Ortiz de la Morena, I. Cebula, M. Zharnikov, and M. Buck, “Self-assembly of 1,3,5-benzenetribenzoic acid on Ag and Cu at the liquid/solid interface”, Phys. Chem. Chem. Phys. **20**, 2731–2740 (2018).

[14] H. Huang, S. L. Wong, W. Chen, and A. T. S. Wee, “LT-STM studies on substrate-dependent self-assembly of small organic molecules”, J. Phys. D: Appl. Phys. **44**, 464005 (2011).

[15] C. Wäckerlin, F. Donati, A. Singha, R. Baltic, S. Rusponi, K. Diller, F. Patthey, M. Pivetta, Y. Lan, S. Klyatskaya, M. Ruben, H. Brune, and J. Dreiser, “Giant Hysteresis of Single-Molecule Magnets Adsorbed on a Nonmagnetic Insulator”, Adv. Mater. **28**, 5195–5199 (2016).

[16] M. Mannini, F. Pineider, C. Danieli, F. Totti, L. Sorace, P. Sainctavit, M.-A. Arrio, E. Otero, L. Joly, J. C. Cezar, A. Cornia, and R. Sessoli, “Quantum tunnelling of the magnetization in a monolayer of oriented single-molecule magnets”, Nature **468**, 417–421 (2010).

[17] B. E. Murphy, S. A. Krasnikov, N. N. Sergeeva, A. A. Cafolla, A. B. Preobrajenski, A. N. Chaika, O. Lübben, and I. V. Shvets, “Homolytic cleavage of molecular oxygen by manganese porphyrins supported on Ag(111)”, ACS Nano **8**, 5190–5198 (2014).

[18] B. Hulsken, R. van Hameren, J. W. Gerritsen, T. Khoury, P. Thordarson, M. J. Crossley, A. E. Rowan, R. J. M. Nolte, J. A. A. W. Elemans, and S. Speller, “Real-time single-molecule imaging of oxidation catalysis at a liquid-solid interface”, Nat. Nanotechnol. **2**, 285–289 (2007).

[19] H. Zhao, Z.-R. Qu, H.-Y. Ye, and R.-G. Xiong, “In situ hydrothermal synthesis of tetrazole coordination polymers with interesting physical properties”, Chem. Soc. Rev. **37**, 84–100 (2008).

[20] Z. Yan, M. Li, H.-L. Gao, X.-C. Huang, and D. Li, “High-spin versus spin-crossover versus low-spin: geometry intervention in cooperativity in a 3D polymorphic iron(II)-tetrazole MOFs system”, Chem. Commun. **48**, 3960–3962 (2012).

[21] S. Westhues, J. Idel, and J. Klankermayer, “Molecular catalyst systems as key enablers for tailored polyesters and polycarbonate recycling concepts”, Sci. Adv. **4**, eaat9669 (2018).

[22] K. Song, K. Kim, D. Hong, J. Kim, C. E. Heo, H. I. Kim, and S. H. Hong, “Highly active ruthenium metathesis catalysts enabling ring-opening metathesis polymerization of cyclopentadiene at low temperatures”, Nat. Commun. **10**, 3860 (2019).

[23] P. Quarterman, C. Sun, J. Garcia-Barriocanal, M. DC, Y. Lv, S. Manipatruni, D. E. Nikonov, I. A. Young, P. M. Voyles, and J.-P. Wang, “Demonstration of Ru as the 4th ferromagnetic element at room temperature”, Nat. Commun. **9**, 2058 (2018).

[24] D. Kaiming, Y. Jinlong, X. Chuanyun, and W. Kelin, “Electronic properties and magnetism of ruthenium clusters”, Phys. Rev. B **54**, 2191–2197 (1996).

[25] W. Auwärter, K. Seufert, F. Klappenberger, J. Reichert, A. Weber-Bargioni, A. Verdini, D. Cvetko, M. Dell'Angela, L. Floreano, A. Cossaro, G. Bavdek, A. Morgante, A. P. Seitsonen, and J. V. Barth, "Site-specific electronic and geometric interface structure of Co-tetraphenyl-porphyrin layers on Ag(111)", Phys. Rev. B **81**, 245403 (2010).

[26] C. Ruggieri, S. Rangan, R. A. Bartynski, and E. Galoppini, "Zinc(II) Tetraphenylporphyrin on Ag(100) and Ag(111): Multilayer Desorption and Dehydrogenation", J. Phys. Chem. C **120**, 7575–7585 (2016).

[27] H. Zaglmayr, T. Lackner, L. Sun, and P. Zeppenfeld, "Growth of tetraphenyl-porphyrin thin films on Ag(111)", Synth. Met. **228**, 64–69 (2017).

[28] E. C. Zampronio, M. C. A. F. Gotardo, M. D. Assis, and H. P. Oliveira, "Catalytic Oxidation of Cyclohexane and Cyclooctene over a New Metalloporphyrin Supported on $VOPO_4$ Catalyst", Catal. Lett. **104**, 53–56 (2005).

[29] E. Brulé and Y. R. de Miguel, "Supported metalloporphyrin catalysts for alkene epoxidation", Org. Biomol. Chem. **4**, 599–609 (2006).

[30] N. A. Rakow and K. S. Suslick, "A colorimetric sensor array for odour visualization", Nature **406**, 710–713 (2000).

[31] G. Guillaud, J. Simon, and J. P. Germain, "Metallophthalocyanines", Coord. Chem. Rev. **178-180**, 1433–1484 (1998).

[32] N. Shafizadeh, S. Boyé-Péronne, S. Soorkia, B. K. Cunha de Miranda, G. A. Garcia, L. Nahon, S. Chen, A. de la Lande, L. Poisson, and B. Soep, "The surprisingly high ligation energy of CO to ruthenium porphyrins", Phys. Chem. Chem. Phys. **20**, 11730–11739 (2018).

[33] M. N. Hopkinson, C. Richter, M. Schedler, and F. Glorius, "An overview of N-heterocyclic carbenes", Nature **510**, 485–496 (2014).

[34] G. Binnig and H. Rohrer, "Scanning tunneling microscopy—from birth to adolescence", Rev. Mod. Phys. **59**, 615–625 (1987).

[35] F. Hund, "Zur Deutung der Molekelspektren. III", Z. Physik **43**, 805–826 (1927).

[36] J. Tersoff and D. R. Hamann, "Theory of the scanning tunneling microscope", Phys. Rev. B **31**, 805 (1985).

[37] J. Bardeen, "Tunnelling from a Many-Particle Point of View", Phys. Rev. Lett. **6**, 57 (1961).

[38] H. Hertz, "Ueber einen Einfluss des ultravioletten Lichtes auf die electrische Entladung", Ann. Phys. Chem. **267**, 983–1000 (1887).

[39] A. Einstein, "Über einen die Erzeugung und Verwandlung des Lichtes betreffenden heuristischen Gesichtspunkt", Ann. Phys. Chem. **322**, 132–148 (1905).

[40] T. L. Alford, L. C. Feldman, and J. W. Mayer, *Fundamentals of nanoscale film analysis* (Springer, New York, N.Y. and London, 2007), XIV, 336.

[41] T. A. Carlson, "Basic assumptions and recent developments in quantitative XPS", Surf. Interface Anal. **4**, 125–134 (1982).

[42] B. W. Batterman and H. Cole, “Dynamical Diffraction of X Rays by Perfect Crystals”, Rev. Mod. Phys. **36**, 681–717 (1964).

[43] D. P. Woodruff, “Surface structure determination using x-ray standing waves”, Rep. Prog. Phys. **68**, 743 (2005).

[44] D. P. Woodruff, “Normal incidence X-ray standing wave determination of adsorbate structures”, Prog. Surf. Sci. **57**, 1–60 (1998).

[45] M. Schwarz, A. Riss, M. Garnica, J. Ducke, P. S. Deimel, D. A. Duncan, P. K. Thakur, T.-L. Lee, A. P. Seitsonen, J. V. Barth, F. Allegretti, and W. Auwärter, “Corrugation in the Weakly Interacting Hexagonal-BN/Cu(111) System: Structure Determination by Combining Noncontact Atomic Force Microscopy and X-Ray Standing Waves”, ACS Nano **11**, 9151–9161 (2017).

[46] C. Kittel, *Introduction to solid state physics*, in collab. with P. McEuen, Global edition, [9th edition] (Wiley, Hoboken, NJ, 2018), 692 pp.

[47] D. A. King, “Thermal desorption from metal surfaces: A review”, Surf. Sci. **47**, 384–402 (1975).

[48] J. L. Taylor and W. H. Weinberg, “The effect of time delays in thermal desorption mass spectrometry”, Surf. Sci. **78**, L508–L511 (1978).

[49] M. Ungarish and L. D. Schmidt, “Temperature programmed desorption at high pressures”, Appl. Surf. Sci. (1977-1985) **17**, 23–38 (1983).

[50] D. A. King, T. E. Madey, and J. T. Yates, “Interaction of Oxygen with Polycrystalline Tungsten. II. Corrosive Oxidation”, J. Chem. Phys **55**, 3247–3253 (1971).

[51] P. A. Redhead, “Thermal desorption of gases”, Vacuum **12**, 203–211 (1962).

[52] E. Habenschaden and J. Küppers, “Evaluation of flash desorption spectra”, Surf. Sci. **138**, L147–L150 (1984).

[53] B. Meng and W. H. Weinberg, “Monte Carlo simulations of temperature programmed desorption spectra”, J. Chem. Phys **100**, 5280–5289 (1994).

[54] C. Pisani, G. Rabino, and F. Ricca, “Statistical analysis and model determination for thermal desorption spectra: Nitrogen on tungsten”, Surf. Sci. **41**, 277–292 (1974).

[55] K. Seufert, “Surface anchored porphyrins - investigation of assembly, reactivity, manipulation and in-situ synthesis”, E20, PhD Thesis (Technische Universität München, Garching, 2011).

[56] F. Bischoff, “Scanning probe microscopy studies of surface confined molecules and (metal-organic) nanostructures”, E20, PhD Thesis (Technische Universität München, Garching, 2018).

[57] T.-L. Lee and D. A. Duncan, “A Two-Color Beamline for Electron Spectroscopies at Diamond Light Source”, Synchrotron Radiat. News **31**, 16–22 (2018).

[58] A. Hofmann, T. Ericson, and P. Y. Landshoff, *The Physics of Synchrotron Radiation*, Vol. 20, Cambridge Monographs on Particle Physics, Nuclear Physics and Cosmology (Cambridge University Press, Cambridge, 2004), 347 pp.

[59] P. Knecht, N. Suryadevara, B. Zhang, J. Reichert, M. Ruben, J. V. Barth, S. Klyatskaya, and A. C. Papageorgiou, “The self-assembly and metal adatom coordination of a linear bis-tetrazole ligand on Ag(111)”, Chem. Commun. **54**, 10072–10075 (2018).

[60] A. Wiengarten, J. A. Lloyd, K. Seufert, J. Reichert, W. Auwärter, R. Han, D. A. Duncan, F. Allegretti, S. Fischer, S. C. Oh, Ö. Sağlam, L. Jiang, S. Vijayaraghavan, D. Écija, A. C. Papageorgiou, and J. V. Barth, “Surface-Assisted Cyclodehydrogenation; Break the Symmetry, Enhance the Selectivity”, Chem. - Eur. J. **21**, 12285–12290 (2015).

[61] L. Jiang, B. Zhang, G. Médard, A. P. Seitsonen, F. Haag, F. Allegretti, J. Reichert, B. Kuster, J. V. Barth, and A. C. Papageorgiou, “N-Heterocyclic carbenes on close-packed coinage metal surfaces: bis-carbene metal adatom bonding scheme of monolayer films on Au, Ag and Cu”, Chem. Sci. **8**, 8301–8308 (2017).

[62] G. Lovat, E. A. Doud, D. Lu, G. Kladnik, M. S. Inkpen, M. L. Steigerwald, D. Cvetko, M. S. Hybertsen, A. Morgante, X. Roy, and L. Venkataraman, “Determination of the structure and geometry of N-heterocyclic carbenes on Au(111) using high-resolution spectroscopy”, Chem. Sci. **10**, 930–935 (2019).

[63] X. Wang, C. Chi, K. Zhang, Y. Qian, K. M. Gupta, Z. Kang, J. Jiang, and D. Zhao, “Reversed thermo-switchable molecular sieving membranes composed of two-dimensional metal-organic nanosheets for gas separation”, Nat. Commun. **8**, 14460 (2017).

[64] P. S. Deimel, “Bonding, Reactivity and Chemical Transformations of Adsorbed Organic and Metal-Organic Species”, E20, PhD Thesis (Technische Universität München, Garching, 2019).

[65] D. Nečas and P. Klapetek, “Gwyddion: an open-source software for SPM data analysis”, Open Phys. **10**, 181–188 (2012).

[66] P. Feulner and D. Menzel, “Simple ways to improve ”flash desorption” measurements from single crystal surfaces”, J. Vac. Sci. Technol. **17**, 662–663 (1980).

[67] S. P. Frigo, P. Feulner, B. Kassühlke, C. Keller, and D. Menzel, “Observation of Neutral Atomic Fragments for Specific 1s Core Excitations of an Adsorbed Molecule”, Phys. Rev. Lett. **80**, 2813 (1998).

[68] P. Giannozzi, S. Baroni, N. Bonini, M. Calandra, R. Car, C. Cavazzoni, D. Ceresoli, G. L. Chiarotti, M. Cococcioni, I. Dabo, A. Dal Corso, S. de Gironcoli, S. Fabris, G. Fratesi, R. Gebauer, U. Gerstmann, C. Gougoussis, A. Kokalj, M. Lazzeri, L. Martin-Samos, N. Marzari, F. Mauri, R. Mazzarello, S. Paolini, A. Pasquarello, L. Paulatto, C. Sbraccia, S. Scandolo, G. Sclauzero, A. P. Seitsonen, A. Smogunov, P. Umari, and R. M. Wentzcovitch, “QUANTUM ESPRESSO: a Modular and Open-Source Software Project for Quantum Simulations of Materials”, J. Phys.: Condens. Matter **21**, 395502 (2009).

[69] I. Hamada, “Van der Waals density functional made accurate”, Phys. Rev. B **89**, 121103 (2014).

[70] K. Lee, É. D. Murray, L. Kong, B. I. Lundqvist, and D. C. Langreth, “Higher-accuracy van der Waals density functional”, Phys. Rev. B **82**, 081101 (2010).

[71] P. E. Blöchl, O. Jepsen, and O. K. Andersen, “Improved tetrahedron method for Brillouin-zone integrations”, Phys. Rev. B **49**, 16223–16233 (1994).

[72] P. Hapala, G. Kichin, C. Wagner, F. S. Tautz, R. Temirov, and P. Jelínek, “Mechanism of High-Resolution STM/AFM Imaging with Functionalized Tips”, Phys. Rev. B **90**, 085421 (2014).

[73] M. M. Antonijevic and M. B. Petrovic, “Copper Corrosion Inhibitors, A review”, Int. J. Electrochem. Sci. **2008**, 1–28 (2007).

[74] Y. I. Kuznetsov and L. P. Kazansky, “Physicochemical aspects of metal protection by azoles as corrosion inhibitors”, Russ. Chem. Rev. **77**, 219–232 (2008).

[75] G. Aromí, L. A. Barrios, O. Roubeau, and P. Gamez, “Triazoles and tetrazoles, Prime ligands to generate remarkable coordination materials”, Coord. Chem. Rev. **255**, 485–546 (2011).

[76] A. Maspero, S. Galli, V. Colombo, G. Peli, N. Masciocchi, S. Stagni, E. Barea, and J. A. Navarro, “Metalorganic frameworks based on the 1,4-bis(5-tetrazolyl) benzene ligand, The Ag and Cu derivatives”, Inorg. Chim. Acta **362**, 4340–4346 (2009).

[77] F. Grillo, J. A. Garrido Torres, M.-J. Treanor, C. R. Larrea, J. P. Götze, P. Lacovig, H. A. Früchtl, R. Schaub, and N. V. Richardson, “Two-dimensional self-assembly of benzotriazole on an inert substrate”, Nanoscale **8**, 9167–9177 (2016).

[78] F. Grillo, D. W. Tee, S. M. Francis, H. A. Früchtl, and N. V. Richardson, “Passivation of Copper, Benzotriazole Films on Cu(111)”, J. Phys. Chem. C **118**, 8667–8675 (2014).

[79] F. Grillo, D. W. Tee, S. M. Francis, H. A. Früchtl, and N. V. Richardson, “Initial stages of benzotriazole adsorption on the Cu(111) surface”, Nanoscale **5**, 5269–5273 (2013).

[80] S. J. Jethwa, E. L. Kolsbjerg, S. R. Vadapoo, J. L. Cramer, L. Lammich, K. V. Gothelf, B. Hammer, and T. R. Linderoth, “Supramolecular Corrals on Surfaces Resulting from Aromatic Interactions of Nonplanar Triazoles”, ACS Nano **11**, 8302–8310 (2017).

[81] L. Cui, Y.-F. Geng, C. F. Leong, Q. Ma, D. M. D’Alessandro, K. Deng, Q.-D. Zeng, and J.-L. Zuo, “Synthesis, properties and surface self-assembly of a pentanuclear cluster based on the new π-conjugated TTF-triazole ligand”, Sci. Rep. **6**, 25544 (2016).

[82] I. Stassen, D. de Vos, and R. Ameloot, “Vapor-Phase Deposition and Modification of Metal-Organic Frameworks, State-of-the-Art and Future Directions”, Chem. - Eur. J. **22**, 14452–14460 (2016).

[83] L. Dong, Z. Gao, and N. Lin, “Self-assembly of metal–organic coordination structures on surfaces”, Prog. Surf. Sci. **91**, 101–135 (2016).

[84] N. Lin, S. Stepanow, M. Ruben, and J. V. Barth, “Surface-confined supramolecular coordination chemistry”, Top. Curr. Chem. **287**, 1–44 (2009).

[85] J. V. Barth, “Fresh perspectives for surface coordination chemistry”, Surf. Sci. **603**, 1533–1541 (2009).

[86] R. Gutzler, S. Stepanow, D. Grumelli, M. Lingenfelder, and K. Kern, “Mimicking enzymatic active sites on surfaces for energy conversion chemistry”, Acc. Chem. Res. **48**, 2132–2139 (2015).

[87] D. Écija, J. I. Urgel, A. P. Seitsonen, W. Auwärter, and J. V. Barth, “Lanthanide-Directed Assembly of Interfacial Coordination Architectures-From Complex Networks to Functional Nanosystems”, Acc. Chem. Res. **51**, 365–375 (2018).

[88] T. Groizard, N. Papior, B. Le Guennic, V. Robert, and M. Kepenekian, “Enhanced Cooperativity in Supported Spin-Crossover Metal-Organic Frameworks”, J. Phys. Chem. Lett. **8**, 3415–3420 (2017).

[89] K. Morgenstern, G. Rosenfeld, and G. Comsa, “Decay of two-dimensional Ag islands on Ag(111)”, Phys. Rev. Lett. **76**, 2113–2116 (1996).

[90] M. Poensgen, J. F. Wolf, J. Frohn, M. Giesen, and H. Ibach, “Step dynamics on Ag(111) and Cu(100) surfaces”, Surf. Sci. **274**, 430–440 (1992).

[91] J.-H. Deng, X.-L. Yuan, and G.-Q. Mei, “A three-dimensional highly stable Zn(II) coordination polymer based on 1,4-benzeneditetrazolate (H_2BDT), Synthesis, crystal structure, and luminescent properties”, Inorg. Chem. Commun. **13**, 1585–1589 (2010).

[92] A. C. Papageorgiou, J. Li, S. C. Oh, B. Zhang, Ö. Sağlam, Y. Guo, J. Reichert, D. Cortizo, A. Belén Marco, A. Mateo-Alonso, and J. V. Barth, “Tuning the ease of formation of on-surface metal-adatom coordination polymers featuring diketones”, Nanoscale, 9561–9568 (2018).

[93] C. G. Williams, M. Wang, D. Skomski, C. D. Tempas, L. L. Kesmodel, and S. L. Tait, “Metal–Ligand Complexation through Redox Assembly at Surfaces Characterized by Vibrational Spectroscopy”, J. Phys. Chem. C **121**, 13183–13190 (2017).

[94] A. Wiengarten, K. Seufert, W. Auwärter, D. Écija, K. Diller, F. Allegretti, F. Bischoff, S. Fischer, D. A. Duncan, A. C. Papageorgiou, F. Klappenberger, R. G. Acres, T. H. Ngo, and J. V. Barth, “Surface-assisted dehydrogenative homocoupling of porphine molecules”, J. Am. Chem. Soc. **136**, 9346–9354 (2014).

[95] J. S. Stevens, L. K. Newton, C. Jaye, C. A. Muryn, D. A. Fischer, and S. L. M. Schroeder, “Proton Transfer, Hydrogen Bonding, and Disorder, Nitrogen Near-Edge X-ray Absorption Fine Structure and X-ray Photoelectron Spectroscopy of Bipyridine–Acid Salts and Co-crystals”, Cryst. Growth Des. **15**, 1776–1783 (2015).

[96] A. C. Papageorgiou, S. Fischer, J. Reichert, K. Diller, F. Blobner, F. Klappenberger, F. Allegretti, A. P. Seitsonen, and J. V. Barth, “Chemical transformations drive complex self-assembly of uracil on close-packed coinage metal surfaces”, ACS Nano **6**, 2477–2486 (2012).

[97] E. Szőcs, I. Bakó, T. Kosztolányi, I. Bertóti, and E. Kálmán, “EC-STM study of 5-mercapto-1-phenyl-tetrazole adsorption on Cu(111)”, Electrochim. Acta **49**, 1371–1378 (2004).

[98] A. Katrib, N. R. El-Rayyes, and F. M. Al-Kharafi, “N 1s orbital binding energies of some pyrazole pyrazoline compounds by XPS”, J. Electron. Spectrosc. Relat. Phenom. **31**, 317–321 (1983).

[99] G. Xue, Q. Dai, and S. Jiang, “Chemical reactions of imidazole with metallic silver studied by the use of SERS and XPS techniques”, J. Am. Chem. Soc., 2393–2395 (1988).

[100] J. J. Yeh and I. Lindau, “Atomic subshell photoionization cross sections and asymmetry parameters. $1 \leq Z \leq 103$”, At. Data Nucl. Data Tables **32**, 1–155 (1985).

[101] T. Wu, R. Zhou, and D. Li, “Effect of substituted groups of ligand on construction of topological networks, In situ generated silver(I) tetrazolate coordination polymers”, Inorg. Chem. Commun. **9**, 341–345 (2006).

[102] F. Bebensee, K. Svane, C. Bombis, F. Masini, S. Klyatskaya, F. Besenbacher, M. Ruben, B. Hammer, and T. R. Linderoth, “A surface coordination network based on copper adatom trimers”, Angew. Chem. Int. Ed. **53**, 12955–12959 (2014).

[103] A. P. Grosvenor, B. A. Kobe, M. C. Biesinger, and N. S. McIntyre, “Investigation of multiplet splitting of Fe 2p XPS spectra and bonding in iron compounds”, Surf. Interface Anal. **36**, 1564–1574 (2004).

[104] A. Shchyrba, C. Wäckerlin, J. Nowakowski, S. Nowakowska, J. Björk, S. Fatayer, J. Girovsky, T. Nijs, S. C. Martens, A. Kleibert, M. Stöhr, N. Ballav, T. A. Jung, and L. H. Gade, “Controlling the dimensionality of on-surface coordination polymers via endo- or exoligation”, J. Am. Chem. Soc. **136**, 9355–9363 (2014).

[105] S. Vijayaraghavan, W. Auwärter, D. Écija, K. Seufert, S. Rusponi, T. Houwaart, P. Sautet, M.-L. Bocquet, P. K. Thakur, S. Stepanow, U. Schlickum, M. Etzkorn, H. Brune, and J. V. Barth, “Restoring the Co magnetic moments at interfacial Co-porphyrin arrays by site-selective uptake of iron”, ACS Nano **9**, 3605–3616 (2015).

[106] H. Marbach, “Surface-Mediated in Situ Metalation of Porphyrins at the Solid-Vacuum Interface”, Acc. Chem. Res. **48**, 2649–2658 (2015).

[107] K. Diller, A. C. Papageorgiou, F. Klappenberger, F. Allegretti, J. V. Barth, and W. Auwärter, “In vacuo interfacial tetrapyrrole metallation”, Chem. Soc. Rev. **45**, 1629–1656 (2016).

[108] J. M. Gottfried, “Surface chemistry of porphyrins and phthalocyanines”, Surf. Sci. Rep. **70**, 259–379 (2015).

[109] A. Baklanov, M. Garnica, A. Robert, M.-L. Bocquet, K. Seufert, J. T. Küchle, P. T. P. Ryan, F. Haag, R. Kakavandi, F. Allegretti, and W. Auwärter, “On-Surface Synthesis of Nonmetal Porphyrins”, J. Am. Chem. Soc. **142**, 1871–1881 (2020).

[110] M. Schöniger, S. R. Kachel, J. Herritsch, P. Schröder, M. Hutter, and J. M. Gottfried, “Direct synthesis of dilithium tetraphenylporphyrin: facile reaction of a free-base porphyrin with vapor-deposited lithium”, Chem. Commun. **55**, 13665–13668 (2019).

[111] W. Auwärter, D. Écija, F. Klappenberger, and J. V. Barth, “Porphyrins at interfaces”, Nat. Chem. **7**, 105 (2015).

[112] M. Turner, O. P. H. Vaughan, G. Kyriakou, D. J. Watson, L. J. Scherer, A. C. Papageorgiou, J. K. M. Sanders, and R. M. Lambert, “Deprotection, tethering, and activation of a one-legged metalloporphyrin on a chemically active metal surface: NEXAFS, synchrotron XPS, and STM study of [SAc]P-Mn(III)Cl on Ag(100)”, J. Am. Chem. Soc. **131**, 14913–14919 (2009).

[113] F. Sedona, M. Lo Cicero, S. Carlotto, A. Basagni, M. M. S. Fakhrabadi, M. Casarin, and M. Sambi, “Substrate involvement in dioxygen bond dissociation catalysed by iron phthalocyanine supported on Ag(100)”, Chem. Commun. **54**, 9418–9421 (2018).

[114] M. Pagliaro, S. Campestrini, and R. Ciriminna, “Ru-based oxidation catalysis”, Chem. Soc. Rev. **34**, 837–845 (2005).

[115] P. Fackler, S. M. Huber, and T. Bach, “Enantio- and regioselective epoxidation of olefinic double bonds in quinolones, pyridones, and amides catalyzed by a ruthenium porphyrin catalyst with a hydrogen bonding site”, J. Am. Chem. Soc. **134**, 12869–12878 (2012).

[116] D. A. Duncan, P. S. Deimel, A. Wiengarten, R. Han, R. G. Acres, W. Auwärter, P. Feulner, A. C. Papageorgiou, F. Allegretti, and J. V. Barth, “Immobilised molecular catalysts and the role of the supporting metal substrate”, Chem. Commun. **51**, 9483–9486 (2015).

[117] M. Xiao, L. Gao, Y. Wang, X. Wang, J. Zhu, Z. Jin, C. Liu, H. Chen, G. Li, J. Ge, Q. He, Z. Wu, Z. Chen, and W. Xing, “Engineering Energy Level of Metal Center: Ru Single-Atom Site for Efficient and Durable Oxygen Reduction Catalysis”, J. Am. Chem. Soc. **141**, 19800–19806 (2019).

[118] T. Lukasczyk, K. Flechtner, L. R. Merte, N. Jux, F. Maier, J. M. Gottfried, and H.-P. Steinrück, “Interaction of Cobalt(II) Tetraarylporphyrins with a Ag(111) Surface Studied with Photoelectron Spectroscopy”, J. Phys. Chem. C **111**, 3090–3098 (2007).

[119] K. Diller, F. Klappenberger, F. Allegretti, A. C. Papageorgiou, S. Fischer, A. Wiengarten, S. Joshi, K. Seufert, D. Écija, W. Auwärter, and J. V. Barth, “Investigating the molecule-substrate interaction of prototypic tetrapyrrole compounds: adsorption and self-metalation of porphine on Cu(111)”, J. Chem. Phys **138**, 154710 (2013).

[120] A. C. Papageorgiou, K. Diller, S. Fischer, F. Allegretti, F. Klappenberger, S. C. Oh, Ö. Sağlam, J. Reichert, A. Wiengarten, K. Seufert, W. Auwärter, and J. V. Barth, “Correction to “In Vacuo Porphyrin Metalation on Ag(111) via Chemical Vapor Deposition of $Ru_3(CO)_{12}$, Mechanistic Insights””, J. Phys. Chem. C **121**, 12503 (2017).

[121] A. C. Papageorgiou, K. Diller, S. Fischer, F. Allegretti, F. Klappenberger, S. C. Oh, Ö. Sağlam, J. Reichert, A. Wiengarten, K. Seufert, W. Auwärter, and J. V. Barth, “In Vacuo Porphyrin Metalation on Ag(111) via Chemical Vapor Deposition of $Ru_3(CO)_{12}$, Mechanistic Insights”, J. Phys. Chem. C **120**, 8751–8758 (2016).

[122] K. Jarzembska, S. Seal, K. Woźniak, A. Szadkowska, M. Bieniek, and K. Grela, “X–Ray Photoelectron Spectroscopy and Reactivity Studies of a Series of Ruthenium Catalysts”, ChemCatChem **1**, 144–151 (2009).

[123] S. Lizzit, A. Baraldi, A. Groso, K. Reuter, M. V. Ganduglia-Pirovano, C. Stampfl, M. Scheffler, M. Stichler, C. Keller, W. Wurth, and D. Menzel, “Surface Core-Level Shifts of Clean and Oxygen-Covered Ru(0001)”, Phys. Rev. B **63**, 205419 (2001).

[124] A. C. Papageorgiou, S. Fischer, S. C. Oh, Ö. Sağlam, J. Reichert, A. Wiengarten, K. Seufert, S. Vijayaraghavan, D. Écija, W. Auwärter, F. Allegretti, R. G. Acres, K. C. Prince, K. Diller, F. Klappenberger, and J. V. Barth, “Self-Terminating Protocol for an Interfacial Complexation Reaction in Vacuo by Metal–Organic Chemical Vapor Deposition”, ACS Nano **7**, 4520–4526 (2013).

[125] T. Houwaart, T. Le Bahers, P. Sautet, W. Auwärter, K. Seufert, J. V. Barth, and M.-L. Bocquet, “Scrutinizing Individual CoTPP Molecule Sdsorbed on Coinage Metal Surfaces from the Interplay of STM Experiment and Theory”, Surf. Sci. **635**, 108–114 (2015).

[126] D. A. Duncan, P. Casado Aguilar, M. Paszkiewicz, K. Diller, F. Bondino, E. Magnano, F. Klappenberger, I. Píš, A. Rubio, J. V. Barth, A. Pérez Paz, and F. Allegretti, “Local Adsorption Structure and Bonding of Porphine on Cu(111) Before and After Self-Metalation”, J. Chem. Phys **150**, 094702 (2019).

[127] P. T. P. Ryan, P. L. Lalaguna, F. Haag, M. M. Braim, P. Ding, D. J. Payne, J. V. Barth, T.-L. Lee, D. P. Woodruff, F. Allegretti, and D. A. Duncan, “Validation of the Inverted Adsorption Structure for Free-Base Tetraphenyl Porphyrin on Cu(111)”, Chem. Commun. **56**, 3681–3684 (2020).

[128] F. Buchner, I. Kellner, W. Hieringer, A. Görling, H.-P. Steinrück, and H. Marbach, “Ordering Aspects and Intramolecular Conformation of Tetraphenylporphyrins on Ag(111)”, Phys. Chem. Chem. Phys. **12**, 13082–13090 (2010).

[129] M. Schwarz, D. A. Duncan, M. Garnica, J. Ducke, P. S. Deimel, P. K. Thakur, T.-L. Lee, F. Allegretti, and W. Auwärter, “Quantitative determination of a model organic/insulator/metal interface structure”, Nanoscale **10**, 21971–21977 (2018).

[130] G. Di Santo, S. Blankenburg, C. Castellarin–Cudia, M. Fanetti, P. Borghetti, L. Sangaletti, L. Floreano, A. Verdini, E. Magnano, F. Bondino, C. A. Pignedoli, M.-T. Nguyen, R. Gaspari, D. Passerone, and A. Goldoni, “Supramolecular Engineering through Temperature–Induced Chemical Modification of 2H–Tetraphenylporphyrin on Ag(111), Flat Phenyl Conformation and Possible Dehydrogenation Reactions”, Chem. - Eur. J. **17**, 14354–14359 (2011).

[131] B. Cirera, B. de La Torre, D. Moreno, M. Ondráček, R. Zbořil, R. Miranda, P. Jelínek, and D. Écija, “On-Surface Synthesis of Gold Porphyrin Derivatives via a Cascade of Chemical Interactions: Planarization, Self-Metalation, and Intermolecular Coupling”, Chem. Mater. **31**, 3248–3256 (2019).

[132] H. M. Sturmeit, I. Cojocariu, M. Jugovac, A. Cossaro, A. Verdini, L. Floreano, A. Sala, G. Comelli, S. Moro, M. Stredansky, M. Corva, E. Vesselli, P. Puschnig, C. M. Schneider, V. Feyer, G. Zamborlini, and M. Cinchetti, “Molecular anchoring stabilizes low

valence Ni(I)TPP on copper against thermally induced chemical changes", J. Mater. Chem. C **8**, 8876–8886 (2020).

[133] H. Chen, L. Tao, D. Wang, Z.-Y. Wu, J.-L. Zhang, S. Gao, W. Xiao, S. Du, K.-H. Ernst, and H.-J. Gao, "Stereoselective On-Surface Cyclodehydrofluorization of a Tetraphenylporphyrin and Homochiral Self-Assembly", Angew. Chem. Int. Ed., 10.1002/anie.202005425 (2020).

[134] I. Kröger, B. Stadtmüller, C. Stadler, J. Ziroff, M. Kochler, A. Stahl, F. Pollinger, T.-L. Lee, J. Zegenhagen, F. Reinert, and C. Kumpf, "Submonolayer Growth of Copper-Phthalocyanine on Ag(111)", New J. Phys. **12**, 083038 (2010).

[135] J. D. Baran, J. A. Larsson, R. A. J. Woolley, Y. Cong, P. J. Moriarty, A. A. Cafolla, K. Schulte, and V. R. Dhanak, "Theoretical and Experimental Comparison of SnPc, PbPc, and CoPc Adsorption on Ag(111)", Phys. Rev. B **81**, 075413 (2010).

[136] P. S. Deimel, R. M. Bababrik, B. Wang, P. J. Blowey, L. A. Rochford, P. K. Thakur, T.-L. Lee, M.-L. Bocquet, J. V. Barth, D. P. Woodruff, D. A. Duncan, and F. Allegretti, "Direct quantitative identification of the "surface trans-effect"", Chem. Sci. **7**, 5647–5656 (2016).

[137] Y. Bai, "Photoelectron Spectroscopic Investigations of Porphyrins and Phthalocyanines on Ag(111) and Au(111), Adsorption and Reactivity", PhD thesis (Friedrich-Alexander-Universität Erlangen-Nürnberg, 2010).

[138] B. Cordero, V. Gómez, A. E. Platero-Prats, M. Revés, J. Echeverría, E. Cremades, F. Barragán, and S. Alvarez, "Covalent Radii Revisited", Dalton Trans. **0**, 2832–2838 (2008).

[139] N. D. Lang and A. R. Williams, "Theory of Atomic Chemisorption on Simple Metals", Phys. Rev. B **18**, 616–636 (1978).

[140] A. Gerlach, F. Schreiber, S. Sellner, H. Dosch, I. A. Vartanyants, B. C. C. Cowie, T.-L. Lee, and J. Zegenhagen, "Adsorption-Induced Distortion of F_{16}CuPc on Cu(111) and Ag(111), An X-ray Standing Wave Study", Phys. Rev. B **71**, 205425 (2005).

[141] M. O. Senge, S. A. MacGowan, and J. M. O'Brien, "Conformational Control of Cofactors in Nature - the Influence of Protein-Induced Macrocycle Distortion on the Biological Function of Tetrapyrroles", Chem. Commun. **51**, 17031–17063 (2015).

[142] M. Roucan, M. Kielmann, S. J. Connon, S. S. R. Bernhard, and M. O. Senge, "Conformational Control of Nonplanar Free Base Porphyrins: Towards Bifunctional Catalysts of Tunable Basicity", Chem. Commun. **54**, 26–29 (2017).

[143] C. Bürker, A. Franco-Cañellas, K. Broch, T.-L. Lee, A. Gerlach, and F. Schreiber, "Self-Metalation of 2*H*-Tetraphenylporphyrin on Cu(111) Studied with XSW: Influence of the Central Metal Atom on the Adsorption Distance", J. Phys. Chem. C **118**, 13659–13666 (2014).

[144] M. Lepper, J. Köbl, L. Zhang, M. Meusel, H. Hölzel, D. Lungerich, N. Jux, A. de Siervo, B. Meyer, H.-P. Steinrück, and H. Marbach, “Controlling the Self-Metalation Rate of Tetraphenylporphyrins on Cu(111) via Cyano Functionalization”, Angew. Chem. Int. Ed. **57**, 10074–10079 (2018).

[145] R. Hellwig, M. Uphoff, T. Paintner, J. Björk, M. Ruben, F. Klappenberger, and J. V. Barth, “Ho-Mediated Alkyne Reactions at Low Temperatures on Ag(111)”, Chem. - Eur. J. **24**, 16126–16135 (2018).

[146] A. J. Therrien, A. J. R. Hensley, M. D. Marcinkowski, R. Zhang, F. R. Lucci, B. Coughlin, A. C. Schilling, J.-S. McEwen, and E. C. H. Sykes, “An atomic-scale view of single-site Pt catalysis for low-temperature CO oxidation”, Nat. Catal. **1**, 192–198 (2018).

[147] A. Wang, J. Li, and T. Zhang, “Heterogeneous single-atom catalysis”, Nat. Rev. Chem. **2**, 65–81 (2018).

[148] J. Wang, R. You, C. Zhao, W. Zhang, W. Liu, X.-P. Fu, Y. Li, F. Zhou, X. Zheng, Q. Xu, T. Yao, C.-J. Jia, Y.-G. Wang, W. Huang, and Y. Wu, “N-Coordinated Dual-Metal Single-Site Catalyst for Low-Temperature CO Oxidation”, ACS Catal. **10**, 2754–2761 (2020).

[149] K. Seufert, W. Auwärter, and J. V. Barth, “Discriminative Response of Surface-Confined Metalloporphyrin Molecules to Carbon and Nitrogen Monoxide”, J. Am. Chem. Soc. **132**, 18141–18146 (2010).

[150] T. Omiya, Y. Kim, R. Raval, and H. Arnolds, “Ultrafast Vibrational Dynamics of CO Ligands on RuTPP/Cu(110) under Photodesorption Conditions”, Surfaces **2**, 117–130 (2019).

[151] T. Omiya, P. Poli, H. Arnolds, R. Raval, M. Persson, and Y. Kim, “Desorption of CO from individual ruthenium porphyrin molecules on a copper surface via an inelastic tunnelling process”, Chem. Commun. **53**, 6148–6151 (2017).

[152] K. Flechtner, A. Kretschmann, L. R. Bradshaw, M.-M. Walz, H.-P. Steinrück, and J. M. Gottfried, “Surface-Confined Two-Step Synthesis of the Complex (Ammine)(Meso-Tetraphenylporphyrinato)-Zinc(II) on Ag(111)”, J. Phys. Chem. C **111**, 5821–5824 (2007).

[153] K. Seufert, M.-L. Bocquet, W. Auwärter, A. Weber-Bargioni, J. Reichert, N. Lorente, and J. V. Barth, “Cis-Dicarbonyl Binding at Cobalt and Iron Porphyrins with Saddle-Shape Conformation”, Nat. Chem. **3**, 114–119 (2011).

[154] W. Hieringer, K. Flechtner, A. Kretschmann, K. Seufert, W. Auwärter, J. V. Barth, A. Görling, H.-P. Steinrück, and J. M. Gottfried, “The surface trans effect: influence of axial ligands on the surface chemical bonds of adsorbed metalloporphyrins”, J. Am. Chem. Soc. **133**, 6206–6222 (2011).

[155] C. Wäckerlin, D. Chylarecka, A. Kleibert, K. Müller, C. Iacovita, F. Nolting, T. A. Jung, and N. Ballav, “Controlling spins in adsorbed molecules by a chemical switch”, Nat. Commun. **1**, 61 (2010).

[156] R. A. van Delden, M. K. J. ter Wiel, M. M. Pollard, J. Vicario, N. Koumura, and B. L. Feringa, “Unidirectional molecular motor on a gold surface”, Nature **437**, 1337–1340 (2005).

[157] M. Alemani, M. V. Peters, S. Hecht, K.-H. Rieder, F. Moresco, and L. Grill, “Electric field-induced isomerization of azobenzene by STM”, J. Am. Chem. Soc. **128**, 14446–14447 (2006).

[158] B. Baisch, D. Raffa, U. Jung, O. M. Magnussen, C. Nicolas, J. Lacour, J. Kubitschke, and R. Herges, “Mounting freestanding molecular functions onto surfaces: the platform approach”, J. Am. Chem. Soc. **131**, 442–443 (2009).

[159] P. Knecht, P. T. P. Ryan, D. A. Duncan, L. Jiang, J. Reichert, P. S. Deimel, F. Haag, J. T. Küchle, F. Allegretti, M. Schwarz, M. Garnica, W. Auwärter, A. P. Seitsonen, J. V. Barth, and A. C. Papageorgiou, “Tunable Interface of Ruthenium Porphyrins and Silver”, J. Phys. Chem. C **125**, 3215–3224 (2021).

[160] S. R. Burema, K. Seufert, W. Auwärter, J. V. Barth, and M.-L. Bocquet, “Probing Nitrosyl Ligation of Surface-Confined Metalloporphyrins by Inelastic Electron Tunneling Spectroscopy”, ACS Nano **7**, 5273–5281 (2013).

[161] A. Stróżecka, M. Soriano, J. I. Pascual, and J. J. Palacios, “Reversible Change of the Spin State in a Manganese Phthalocyanine by Coordination of CO Molecule”, Phys. Rev. Lett. **109**, 32655–32662 (2012).

[162] H. Kim, Y. H. Chang, W.-J. Jang, E.-S. Lee, Y.-H. Kim, and S.-J. Kahng, “Probing Single-Molecule Dissociations from a Bimolecular Complex NO–Co-Porphyrin”, ACS Nano **9**, 7722–7728 (2015).

[163] W. Hansen, M. Bertolo, and K. Jacobi, “Physisorption of CO on Ag(111): investigation of the monolayer and the multilayer through HREELS, ARUPS, and TDS”, Surf. Sci. **253**, 1–12 (1991).

[164] P. S. Deimel, P. Feulner, J. V. Barth, and F. Allegretti, “Spatial decoupling of macrocyclic metal–organic complexes from a metal support: a 4-fluorothiophenol self-assembled monolayer as a thermally removable spacer”, Phys. Chem. Chem. Phys. **21**, 10992–11003 (2019).

[165] G. Blyholder, “Molecular Orbital View of Chemisorbed Carbon Monoxide”, J. Phys. Chem. **68**, 2772–2777 (1964).

[166] P. Knecht, B. Zhang, J. Reichert, D. A. Duncan, M. Schwarz, F. Haag, P. T. P. Ryan, T.-L. Lee, P. S. Deimel, P. Feulner, F. Allegretti, W. Auwärter, G. Médard, A. P. Seitsonen, J. V. Barth, and A. C. Papageorgiou, “Assembly and Manipulation of a Prototypical N-Heterocyclic Carbene with a Metalloporphyrin Pedestal on a Solid Surface”, J. Am. Chem. Soc. **143**, 4433–4439 (2021).

[167] A.-M. Andringa, M.-J. Spijkman, E. C. Smits, S. G. Mathijssen, P. A. van Hal, S. Setayesh, N. P. Willard, O. V. Borshchev, S. A. Ponomarenko, P. W. Blom, and D. M. de Leeuw, “Gas sensing with self-assembled monolayer field-effect transistors”, Org. Electron. **11**, 895–898 (2010).

[168] H. T. Ngo, K. Minami, G. Imamura, K. Shiba, and G. Yoshikawa, “Effects of Center Metals in Porphines on Nanomechanical Gas Sensing”, Sensors **18**, 1640 (2018).

[169] G. Bengasi, R. Meunier–Prest, K. Baba, A. Kumar, A. L. Pellegrino, N. D. Boscher, and M. Bouvet, “Molecular Engineering of Porphyrin–Tapes/Phthalocyanine Heterojunctions for a Highly Sensitive Ammonia Sensor”, Adv. Electron. Mater. **6**, 2000812 (2020).

[170] A. V. Zhukhovitskiy, M. J. MacLeod, and J. A. Johnson, “Carbene ligands in surface chemistry: from stabilization of discrete elemental allotropes to modification of nanoscale and bulk substrates”, Chem. Rev. **115**, 11503–11532 (2015).

[171] C. A. Smith, M. R. Narouz, P. A. Lummis, I. Singh, A. Nazemi, C.-H. Li, and C. M. Crudden, “N-heterocyclic carbenes in materials chemistry”, Chem. Rev. **119**, 4986–5056 (2019).

[172] A. J. Veinot, A. Al–Rashed, J. D. Padmos, I. Singh, D. S. Lee, M. R. Narouz, P. A. Lummis, C. J. Baddeley, C. M. Crudden, and J. H. Horton, “N–heterocyclic carbenes reduce and functionalize copper oxide surfaces in one pot”, Chem. - Eur. J. **26**, 11431–11434 (2020).

[173] P. Lara, O. Rivada-Wheelaghan, S. Conejero, R. Poteau, K. Philippot, and B. Chaudret, “Ruthenium nanoparticles stabilized by N-heterocyclic carbenes: ligand location and influence on reactivity”, Angew. Chem. Int. Ed. **50**, 12080–12084 (2011).

[174] M. J. MacLeod, A. J. Goodman, H.-Z. Ye, H. V.-T. Nguyen, T. van Voorhis, and J. A. Johnson, “Robust gold nanorods stabilized by bidentate N-heterocyclic-carbene-thiolate ligands”, Nat. Chem. **11**, 57–63 (2019).

[175] G. Médard and A. C. Papageorgiou, “Surface anchors target golden bullets”, Nat. Chem. **11**, 20–22 (2019).

[176] A. V. Zhukhovitskiy, M. G. Mavros, T. van Voorhis, and J. A. Johnson, “Addressable carbene anchors for gold surfaces”, J. Am. Chem. Soc. **135**, 7418–7421 (2013).

[177] J. Ren, M. Freitag, C. Schwermann, A. Bakker, S. Amirjalayer, A. Rühling, H.-Y. Gao, N. L. Doltsinis, F. Glorius, and H. Fuchs, “A Unidirectional Surface-Anchored N-Heterocyclic Carbene Rotor”, Nano Lett. **20**, 5922–5928 (2020).

[178] L.-M. Chang, Y.-Y. An, Q.-H. Li, Z.-G. Gu, Y.-F. Han, and J. Zhang, “N-heterocyclic carbene as a surface platform for assembly of homochiral metal–organic framework thin films in chiral sensing”, ACS Appl. Mater. Interfaces **12**, 38357–38364 (2020).

[179] C. R. Larrea, C. J. Baddeley, M. R. Narouz, N. J. Mosey, J. H. Horton, and C. M. Crudden, “N–heterocyclic carbene self–assembled monolayers on copper and gold: dramatic effect of wingtip groups on binding, orientation and assembly”, ChemPhysChem **18**, 3536–3539 (2017).

[180] A. Inayeh, R. Groome, I. Singh, A. J. Veinot, F. Iima, R. Miwa, C. M. Crudden, and A. McLean, “Self-assembly of N-heterocyclic carbenes on Au(111)”, Preprint, 10.26434/chemrxiv.12551627.v1 (2020).

[181] S. Amirjalayer, A. Bakker, M. Freitag, F. Glorius, and H. Fuchs, “Cooperation of N-Heterocyclic Carbenes on a Gold Surface”, Angew. Chem. Int. Ed. **59**, 21230–21235 (2020).

[182] E. A. Doud, R. L. Starr, G. Kladnik, A. Voevodin, E. Montes, N. P. Arasu, Y. Zang, P. Zahl, A. Morgante, L. Venkataraman, H. Vázquez, D. Cvetko, and X. Roy, “Cyclopropenylidenes as Strong Carbene Anchoring Groups on Au Surfaces”, J. Am. Chem. Soc. **142**, 19902–19906 (2020).

[183] F. J. Williams, O. P. H. Vaughan, K. J. Knox, N. Bampos, and R. M. Lambert, “First observation of capping/uncapping by a ligand of a Zn porphyrin adsorbed on Ag(100)”, Chem. Commun., 1688 (2004).

[184] Z. Wang, K. Qian, M. A. Öner, P. S. Deimel, Y. Wang, S. Zhang, X. Zhang, V. Gupta, J. Li, H.-J. Gao, D. A. Duncan, J. V. Barth, X. Lin, F. Allegretti, S. Du, and C.-A. Palma, “Layer-by-Layer Epitaxy of Porphyrin−Ligand Fe(II)-Fe(III) Nanoarchitectures for Advanced Metal–Organic Framework Growth”, ACS Appl. Nano Mater. **3**, 11752–11759 (2020).

[185] O. P. H. Vaughan, F. J. Williams, N. Bampos, and R. M. Lambert, “A chemically switchable molecular pinwheel”, Angew. Chem. Int. Ed. **45**, 3779–3781 (2006).

[186] R. Haldar, L. Heinke, and C. Wöll, “Advanced photoresponsive materials using the metal–organic framework approach”, Adv. Mater. **32**, 1905227 (2020).

[187] K.-H. Chan, X. Guan, V. K.-Y. Lo, and C.-M. Che, “Elevated catalytic activity of ruthenium(II)–porphyrin-catalyzed carbene/nitrene transfer and insertion reactions with N-heterocyclic carbene ligands”, Angew. Chem. Int. Ed. **53**, 2982–2987 (2014).

[188] D. P. Woodruff and D. A. Duncan, “X-ray standing wave studies of molecular adsorption: why coherent fractions matter”, New J. Phys. **22**, 113012 (2020).

[189] D. Marchione, L. Belpassi, G. Bistoni, A. Macchioni, F. Tarantelli, and D. Zuccaccia, “The chemical bond in gold(I) complexes with N-heterocyclic carbenes”, Organometallics **33**, 4200–4208 (2014).

[190] L. Cavallo, A. Correa, C. Costabile, and H. Jacobsen, “Steric and electronic effects in the bonding of N-heterocyclic ligands to transition metals”, J. Organomet. Chem. **690**, 5407–5413 (2005).

[191] F. Xiang, T. Schmitt, M. Raschmann, and M. A. Schneider, “Adsorption and self-assembly of porphyrins on ultrathin CoO films on Ir(100)”, Beilstein J. Nanotechnol. **11**, 1516–1524 (2020).

[192] T. Wähler, R. Schuster, and J. Libuda, “Surface Structure Controls Self-Metalation: In-Situ IR Studies of Anchored Porphyrins on Atomically-Defined Cobalt Oxide Surfaces”, J. Phys. Chem. C **124**, 21538–21548 (2020).

[193] L. Zajac, P. Olszowski, S. Godlewski, L. Bodek, B. Such, R. Jöhr, R. Pawlak, A. Hinaut, T. Glatzel, E. Meyer, and M. Szymonski, “Self-assembling of Zn porphyrins on a (110) face of rutile TiO2–The anchoring role of carboxyl groups”, Appl. Surf. Sci. **379**, 277–281 (2016).

[194] A. G. Slater, Y. Hu, L. Yang, S. P. Argent, W. Lewis, M. O. Blunt, and N. R. Champness, “Thymine functionalised porphyrins, synthesis and heteromolecular surface-based self-assembly”, Chem. Sci. **6**, 1562–1569 (2015).

[195] V. V. Korolkov, S. A. Svatek, A. Summerfield, J. Kerfoot, L. Yang, T. Taniguchi, K. Watanabe, N. R. Champness, N. A. Besley, and P. H. Beton, “van der Waals-Induced Chromatic Shifts in Hydrogen-Bonded Two-Dimensional Porphyrin Arrays on Boron Nitride”, ACS Nano **9**, 10347–10355 (2015).

[196] D. T. Nguyen, M. Freitag, C. Gutheil, K. Sotthewes, B. J. Tyler, M. Böckmann, M. Das, F. Schlüter, N. L. Doltsinis, H. F. Arlinghaus, B. J. Ravoo, and F. Glorius, “An Arylazopyrazole-Based N-Heterocyclic Carbene as a Photoswitch on Gold Surfaces: Light-Switchable Wettability, Work Function, and Conductance”, Angew. Chem. Int. Ed. **59**, 13651–13656 (2020).

[197] F. Donati, S. Rusponi, S. Stepanow, C. Wäckerlin, A. Singha, L. Persichetti, R. Baltic, K. Diller, F. Patthey, E. Fernandes, J. Dreiser, Ž. Šljivančanin, K. Kummer, C. Nistor, P. Gambardella, and H. Brune, “Magnetic remanence in single atoms”, Science **352**, 318–321 (2016).

[198] K. S. Kumar, M. Studniarek, B. Heinrich, J. Arabski, G. Schmerber, M. Bowen, S. Boukari, E. Beaurepaire, J. Dreiser, and M. Ruben, “Engineering On-Surface Spin Crossover: Spin-State Switching in a Self-Assembled Film of Vacuum-Sublimable Functional Molecule”, Adv. Mater. **30**, 1705416 (2018).

[199] A. Köbke, F. Gutzeit, F. Röhricht, A. Schlimm, J. Grunwald, F. Tuczek, M. Studniarek, D. Longo, F. Choueikani, E. Otero, P. Ohresser, S. Rohlf, S. Johannsen, F. Diekmann, K. Rossnagel, A. Weismann, T. Jasper-Tönnies, C. Näther, R. Herges, R. Berndt, and M. Gruber, “Reversible Coordination-Induced Spin-State Switching in Complexes on Metal Surfaces”, Nat. Nanotechnol. **15**, 18–21 (2020).

[200] C. T. Campbell and J. R. V. Sellers, “The entropies of adsorbed molecules”, J. Am. Chem. Soc. **134**, 18109–18115 (2012).

[201] K. A. Fichthorn and R. A. Miron, “Thermal desorption of large molecules from solid surfaces”, Phys. Rev. Lett. **89**, 196103 (2002).

[202] R. Z. Lei, A. J. Gellman, and B. E. Koel, “Desorption energies of linear and cyclic alkanes on surfaces: anomalous scaling with length”, Surf. Sci. **554**, 125–140 (2004).

[203] T. Wagner, H. Karacuban, and R. Möller, “Analysis of complex thermal desorption spectra: PTCDA on copper”, Surf. Sci. **603**, 482–490 (2009).

[204] T. J. Rockey, M. Yang, and H.-L. Dai, “Adsorption energies, inter-adsorbate interactions, and the two binding sites within monolayer benzene on Ag(111)”, J. Phys. Chem. B **110**, 19973–19978 (2006).

[205] P.-H. Lu, P. J. Lasky, Q.-Y. Yang, Y. Wang, and R. M. Osgood, “Molecular desorption of methyl halides from GaAs(110): The role of lateral dipole–dipole interaction between adsorbates”, J. Chem. Phys **101**, 10145–10154 (1994).

[206] E. V. Albano, “Thermal desorption mass spectrometry of alkali metal atoms from transition metal surfaces. The influence of coadsorbed oxygen”, J. Chem. Phys **85**, 1044–1051 (1986).

[207] H. K. Kim, A. S. Hyla, P. Winget, H. Li, C. M. Wyss, A. J. Jordan, F. A. Larrain, J. P. Sadighi, C. Fuentes-Hernandez, B. Kippelen, J.-L. Brédas, S. Barlow, and S. R. Marder, “Reduction of the Work Function of Gold by N-Heterocyclic Carbenes”, Chem. Mater. **29**, 3403–3411 (2017).

[208] B. Adhikari, S. Meng, and M. Fyta, “Carbene-mediated self-assembly of diamondoids on metal surfaces”, Nanoscale **8**, 8966–8975 (2016).

[209] C. Wäckerlin, K. Tarafder, J. Girovsky, J. Nowakowski, T. Hählen, A. Shchyrba, D. Siewert, A. Kleibert, F. Nolting, P. M. Oppeneer, T. A. Jung, and N. Ballav, “Ammonia Coordination Introducing a Magnetic Moment in an On-Surface Low-Spin Porphyrin”, Angew. Chem. Int. Ed. **52**, 4568–4571 (2013).

[210] H. Kim, Y. H. Chang, S.-H. Lee, Y.-H. Kim, and S.-J. Kahng, “Switching and sensing spin states of co-porphyrin in bimolecular reactions on Au(111) using scanning tunneling microscopy”, ACS Nano **7**, 9312–9317 (2013).

Acknowledgment

Finally, I would like to thank everyone who contributed to this work in one way or another. First of all, I want to thank Prof. Johannes V. Barth for giving me the opportunity to realize this work, and my supervisor Dr. Anthoula C. Papageorgiou, who provided always excellent support and guidance.

A big thank you goes out to my lab colleagues: Dr. Bodong Zhang, who instructed me on my first days; Dennis Meier for continuing the work on projects that I have started; Dr. Andreas Walz for his help with electronspray ion beam deposition and especially his efforts in maintaining and improving the vacuum chamber.

I also want to thank Dr. Joachim Reichert for his advice on technical problems, repairs of the chamber and experimental procedures, and Karl Eberle and Reinhold Schneider for their help with all kind of repairs.

A large part of the data presented here is the result of two beam times at the DLS, which would not have been possible without Dr. Martin Schwarz, Felix Haag, Johannes T. Küchle, and Dr. Paul T. P. Ryan. Last, I want to highlight the contribution of Dr. David A. Duncan, who gave everything to make each beam time a success!

Furthermore, I had also the opportunity to acquire data from an LT-STM, for which I want to thank Prof. Willi Auwärter and Dr. Knud Seufert, and also from the PSD chamber, where Dr. Peter S. Deimel, Dr. Francesco Allegretti and Prof. Peter Feulner have been a great help not only for the use of the chambers, but also for the data analysis.

A special thanks goes to Dr. Ari Paavo Seitsonen, who has not only provided all theoretical calculations, but also greatly helped with the understanding of the results.

This work could not have been realized without the synthesis of the employed molecules, which was done by Dr. Guillaume Médard and Dr. Nithin Suryadevara.

Last but not least, I want to thank my family and my girlfriend Manuela for always being there.